Study of photo-induced effect on the charge-ordered state in Pr0.65Ca0.35Mn03 and La0.67Ca0.33Mn03

Doctoral Thesis

STUDY OF PHOTO-INDUCED EFFECT ON THE CHARGE-ORDERED STATE IN $Pr_{0.65}Ca_{0.35}MnO_3$ AND $La_{0.67}Ca_{0.33}MnO_3$

1999

Division of Transportation System Engineering
Graduate School of Mercantile Marine Science
Tokyo University of Mercantile Marine

OSAMI Yanagisawa

To Mayeve

who provided the opportunity to try
and the support to complete.

Abstract

The distorted perovskite manganese have got a great interest because of their unusual magnetic and electronic properties. For example, some of these manganese exhibit a magnetic field driven insulator-metal (I-M) transitions so called colossal magnetoresistance (CMR). Recently, in $Pr_{0.7}Ca_{0.3}MnO_3$, I-M transitions driven by an electric field, synchrotron orbit radiation x-ray and laser illumination were reported. Our motivation of the present study is to get a answer for the question; what is exactly going on in the spin and orbital system under the photon injection? With respect to the photo-induced effect we investigate the spin system and the charge system by electron-spin resonance (ESR) and x-ray diffraction, respectively.

As the first step, magnetic and structural behavior of $Pr_{0.65}Ca_{0.35}MnO_3$ (Space group: *Pbnm* at 296 K) in powder form was studied. The onset of the charge-ordered (CO) state at $T_{CO} \sim 215$ K was verified from the change of lattice constants and the appearance of superlattice reflections. The antiferromagnetic transition was found out at $T_{AF} \sim 180$ K based on the ESR linewidth $\Delta H_{P\text{-}P}$. The canted antiferromagnetic transition was observed at $T_{CAF} \sim 125$ K from both the appearance of the spontaneous d.c. magnetization and an abrupt increase of the $\Delta H_{P\text{-}P}$. The resonance intensity in ESR profile becomes weakened with decreasing temperature, suggesting the existence of magnetic disorder below 90 K. It is responsible for behavior of d.c. magnetization below T_{CAF}. They provide an evidence of the existence of the spin-glass state.

To investigate a photo-induced effect, the ESR for $Pr_{0.65}Ca_{0.35}MnO_3$ powder was measured under the photon injection by a He-Ne cw laser with photon energy, $h\upsilon = 1.96$ eV and a Nd-YAG cw laser with $h\upsilon = 1.17$ eV. Both significant change of the ESR curve and increase of the effective spin susceptibility was clearly found out under the photon injection with $h\upsilon = 1.17$ eV between 90 K - 80 K, in the canted antiferromagnetic state associated with the CO structure. The temperature dependence of ESR profile excludes the possibility of laser heating. On the contrary, the ESR curve is not affected much under the photon injection with $h\upsilon = 1.96$ eV. Photon energy, $h\upsilon \sim 1.2$ eV is characteristic in the optical spectra in distorted perovskite manganese. It has been assigned as a charge-transfer excitation energy of an electron from the lower Jahn-Teller split e_g of Mn^{3+} to the e_g of adjacent Mn^{4+} ion, which exhibits the promotion of the dipole active photoionization of the small polaron. Our present result suggests that the photon injection with the characteristic photon energy, $h\upsilon \sim 1.2$ eV enhances vibronic state and eventually releases the cooperative Jahn-Teller distortion associated with the CO state.

The behavior of CO state in $Pr_{0.65}Ca_{0.35}MnO_3$ powder under the photon injection with hυ = 1.17 eV was studied with the x-ray diffraction to understand the mechanism of present photo-induced effect. Below T_{CO}, the superlattice reflections appeared associated with the formation of the CO state and the CO sate was maintained down to at least 10 K. The photon injection led to the prominent decrease of the intensity of superlattice reflections. The present result provides a structural evidence of the collapse of CO state by the photon injection. It also suggests that a photo-induced I-M transition occurs due to the propagation of delocalized carriers via the ferromagnetic double-exchange interaction in the collapsed CO state created by the photon injection.

As the second step, $Pr_{0.65}Ca_{0.35}MnO_3$ thin films were prepared to improve the sensitivity of the photo-induced effect against to the sample thickness due to small penetration depth of the laser light and to get advantages for industrial application. The thin films of $Pr_{0.65}Ca_{0.35}MnO_3$ with 5000 Å thickness were prepared by the sol-gel method on $SrTiO_3$ (100) substrates. In the ESR study, the thin films exhibit the ferromagnetic transition at $T_c \sim 120$ K and some kind of weak photo-induced effect at low temperature. However, the ground state of the discussed thin films are not accompanied by the CO state, which plays an essential role on the photo-induced effect. These differences are due to the oxygen stoichiometry and the strain effect induced by the lattice mismatch.

Thin film of distorted perovskite manganese with large size rare earth and alkaline earth ions, $La_{0.67}Ca_{0.33}MnO_3$ is less affected by the oxygen stoichiometry and/or the strain effect. To enhance the photo-induced effect in $Pr_{0.65}Ca_{0.35}MnO_3$ thin film against these process parameters, $La_{0.67}Ca_{0.33}MnO_3$ thin films were comparatively studied. $La_{0.67}Ca_{0.33}MnO_3$ undergoes the transition from the paramagnetic insulating state into the ferromagnetic metallic state at the Curie temperature, $T_c \sim 260$ K. The temperature dependence of the ESR resonance magnetic field in both $Pr_{0.65}Ca_{0.35}MnO_3$ and $La_{0.67}Ca_{0.33}MnO_3$ thin films obeys a critical behavior of a second-order phase transition, corresponding to the appearance of the spontaneous magnetic moment.

Increase of the effective spin susceptibility and collapse of CO state was found in $Pr_{0.65}Ca_{0.35}MnO_3$ powder under the photon injection with hυ = 1.17 eV. This photo-induced effect has the lowest threshold in I-M transitions found in $Pr_{1-x}Ca_xMnO_3$. However, $Pr_{0.65}Ca_{0.35}MnO_3$ thin films prepared by the sol-gel method does not show photo-induced effect and is not accompanied by the CO state.

Contents

Chapter I
General Introduction

I.1 Perovskite Manganese

I.1.1 Perovskite transition-metal oxides

The inorganic material, perovskite transition-metal oxides are represented as ABX_3 where A, B and X are alkaline earth element, transition-metal and oxygen. These oxides can achieve various series of physical properties, e.g., ferroelectricity (Titanates) [1], high-temperature superconductivity (Cuprates) [2, 3], and magnetism (Manganese) [4, 5, 6, 7] as shown in Table I - 1. Furthermore one can control these properties with great precision. It means that the series of these oxides has a great advantage for industrial devices in the next century than classical semiconductor material which has been used for civil industrial devices, represented by so-called large integrated circuit (LSI) until present day.

Three physical parameter, charge, spin and orbital parameterize electron property of transition metal ion in this system. In these oxides, one can control these properties by the substitution of composing atoms with different ionic radius, ionic valence, and number of total effective spin keeping a charge equilibrium per unit cell. [8, 9] For example, electronic transport and magnetic properties respect the control of hopping between local $3d$-electron through the O_{2p}-orbital and the electron-electron interaction between $3d$-electron on the transition-metal ions. The key is an optimization in charge correlation, spin correlation and orbital correlation.

Physical property	Transition-metal	Compound	References
Ferroelectricity	Ti	$BaTiO_3$, $SrTiO_3$	[1]
Superconductivity	Cu	$YBa_2Cu_3O_{7-\delta}$, $Ba_xLa_{2-x}CuO_{4-y}$	[2, 3]
Magnetism	Mn	(La, Sr)Mn O_3	[4, 5, 6, 7]

Table I - 1 Representative physical property of perovskite transition metal oxide series.

I.1.2 Distorted perovskite manganese

I.1.2.1 Distorted perovskite manganese

The distorted perovskite manganese, $R_{1-x}A_xMnO_3$ (R = trivalent rare earth element and A = divalent alkaline earth element, $0 \leq x \leq 1$) has recently attracted much attention by the virtue of their

unusual magnetic and electronic properties. For example, some of these manganese exhibit a magnetic field driven insulator-metal (I-M) transitions where the conductivity and magnetization change dramatically, an effect termed colossal magnetoresistance (CMR) [4, 5, 6, 7]. These I-M transitions can be achieved not only by a magnetic field, but also by other external stimulation, e.g., electric current [10], synchrotron orbit radiation x-ray [11], and laser light [12].

I.1.2.2 Crystal structure of the perovskite manganese

In the whole range of compositions, the solid solutions, $R_{1-x}A_xMnO_3$ was found to belong to orthorhombically ($a \neq b \neq c$, $\alpha = \beta = \gamma = 90°$) distorted perovskites (space group *Pbnm*). [8, 9, 13, 14, 15, 16]

Figure I - 1 shows the unit cell of the perovskites structure of manganese. A center manganese ion of the unit cell is surrounded by oxygen tetrahedral. Metal ions (R, A) are placed at each corner of the unit cube.

There are two characteristic distortions in the system. One consists of a spontaneous cooperative puckering of the MnO_6 octahedral (S.C. buckling) which makes the coordination polyhedral of R or A ions deformed in such a way that the effective coordination number becomes 9 instead of 12. This kind of distortion is a consequence of the ionic radii mismatch and is common in perovskites with small central cations (Goldschmidt's tolerance factor < 1).

The other kind of lattice distortion is connected with the Jahn-Teller effect of $Mn^{3+}O_6^{2-}$ octahedral and their cooperative ordering below a certain critical temperature. The latter cooperative distortion does not change the Pbnm symmetry but modifies the crystal structure in such a way that $c/\sqrt{2} < a < b$ (O' -type structure).

I.1.2.3 Control of physical property in the perovskite manganese

In the $R_{1-x}A_xMnO_3$, one can control the electronic property through the electronic bandwidth and the doping level.

The population of Mn^{3+} / Mn^{4+} ions is approximately a linear function of x, the chemical composition of R^{+3} and A^{+2} ions. Therefore, the substitution of the (A, R) ion and/or the change of nominal composition can controls the doping level of Mn ions. [8, 9]

The electronic bandwidth is as a function of transfer energy determined by distortion of the perovskite structure associated with modification of the distance between Mn ion sites via inter-site oxygen. Different ionic radii of the (A, R) ion lead into different distortion of the perovskite structure. Therefore, the control of the electronic bandwidth is possible with a selection of the (A, R)

ion. [8, 9] The smaller ionic radii of the (A, R) ions make the smaller transfer integral which can promote the localization of the charge carrier and form the charge-ordered (CO) state. On the other hand, the larger ionic radii of the (A, R) ion make the larger transfer integral which can promote the delocalization of the charge carrier through the double-exchange mechanism.

I.1.3 $R_{1-x}A_xMnO_3$ with large size (A, R) site ions

I.1.3.1 Double-exchange mechanism

The $R_{1-x}A_xMnO_3$ with the larger ionic radii of the (A, R) site ion, such as $La_{1-x}Sr_xMnO_3$ [13] and $La_{1-x}Ca_xMnO_3$ [8] is the prototypic double-exchange ferromagnet.[17, 18, 19, 20, 21] Mother compound, $RMnO_3$ is a Mott insulator due to strong correlation of the $3d$-e_g electron of Mn^{3+}. The hole doping compound, $R_{1-x}A_xMnO_3$, transforms from the antiferromagnetic insulator state (AFI) into the ferromagnetic metal state (FM) with increasing doping carriers, x. This phase transformation has been described by a metallic transport phenomenon carried out by the double-exchange interaction mechanism.

The double-exchange interaction scheme was originally proposed by Zener in 1951 [22], further developed by Anderson and Hasegawa [23], and Goodenough [24], and eventually by A. J. Millis [25, 26, 27]. [28, 29] The Mn $3d$ levels are split by the oxygen octahedral crystal field into a lower energy t_{2g} orbital (triplet) and a higher energy e_g orbital (doublet) as shown in Figure I - 2. The Mn^{3+} ion in the hole undoped compound $RMnO_3$ and Mn^{4+} ion in the hole doped compound $AMnO_3$ have the high spin $3d^4$ electron configuration $t_{2g}^3e_g^1$ and the low spin $3d^3$ electron configuration t_{2g}^3, respectively. According to the Hund's rule, all spins are aligned on a given each site by a large intra-atomic exchange J_H. The t_{2g} orbital hybridize with O_{2p} orbital much more weakly than the e_g orbital, and can be regarded as forming the localized spin ($S = 3/2$). In contrast to that, the e_g orbital, which have lobes directed to the neighboring oxygen atoms, hybridizes strongly with the O_{2p} orbital, producing rather broad bands. [16] The electronic conduction arises from the hopping of an electron from Mn^{3+} to Mn^{4+} with the electron transfer energy t as shown in Figure I - 3 (b). This results in the ferromagnetic (F) double-exchange interaction between the localized spins, the core t_{2g} orbital ($\mathbf{S} = 3/2$) mediated by the hopping e_g orbital electron.

Hamiltonian for the double-exchange mechanism in the hole-doped manganese oxide system will be represented as

$$H = -\sum_{\langle ij\rangle\sigma} t_{ij}\left(c^{\dagger}_{i\sigma}c_{j\sigma} + h.c.\right) - J\sum_i \boldsymbol{\sigma}_i \cdot \mathbf{S}_i \qquad \text{(I - 1)}$$

Here t_{ij} is the transfer integral between neighboring sites i and j. J is Hund coupling constant between the $3d$-e_g electron spin on Mn ions and the $3d$-t_{2g} electron spin. The $c^{\dagger}_{i\sigma}$ creates an electron of spin σ in the $3d$-e_g orbital on site i. The first term represents the $3d$-e_g electron transfer between neighboring sites i and j. The second term represents Hund coupling between the conduction $3d$-e_g electron spin and the localized $3d$-t_{2g} electron spin.

I.1.3.2 Colossal magnetoresistance effect

The application of an external magnetic field aligns the localized $3d$-t_{2g} electron spin and reduces the spin scattering by the localized $3d$-t_{2g} electron spin in the conduction $3d$-e_g electron as shown in Figure I - 3. The Curie temperature T_C is located at a higher temperature than the CO transition temperature T_{CO} in the $R_{1-x}A_xMnO_3$. This effect is expected to be most pronounced around T_C, and hence to cause the CMR effect.

I.1.4 $R_{1-x}A_xMnO_3$ with small size (A, R) site ions

I.1.4.1 Charge-ordered state

On the contrary, a more complex feature appears in the phase diagram of $R_{1-x}A_xMnO_3$ with the smaller ionic radii of the (A, R) site.[4, 5, 8, 14, 30, 31, 32, 33] Those systems remain insulating against doping carriers over the whole temperature range, which is more or less semiconductor.

The CO state appears in $La_{1-x}Ca_xMnO_3$ (x=1/2) [8], $Pr_{1-x}Sr_xMnO_3$ (x=1/2) [30], $Nd_{1-x}Sr_xMnO_3$ (x=1/2) [31], and also in $Pr_{1-x}Ca_xMnO_3$ (x=1/2) at low temperature. [4, 5] The charge carriers are localized on the Mn ion site and form real-space alternation of 1:1 Mn^{3+} / Mn^{4+} species, so called "charge crystal" associated with doubling of the unit cell in unique crystallographic direction. The CO state is stabilized over a wide range of concentration in $R_{1-x}A_xMnO_3$ with small size (A, R) site ions in contrast that the CO state appears only at specified composition (x = 0.5) in $R_{1-x}A_xMnO_3$ with large size (A, R) site ions. Especially, in the $Pr_{1-x}Ca_xMnO_3$, the CO state is stabilized around $0.3 < x < 0.7$.[4, 5, 14] The CO state appears at higher temperature than the magnetic transition temperature at which antiferromagnetic (AF) spin order forms.

I.1.4.2 Ground state of the $R_{1-x}A_xMnO_3$

In general, the ground state of the $R_{1-x}A_xMnO_3$ is characterized by a competing interaction between two different ground states: a charge-delocalized (CD) state, which is metallic with ferromagnetic (F) spin arrangement and exhibits relatively small Jahn-Teller distortions and the CO

insulating state. [25, 16]

In the CD state, the origin of the ferromagnetic (F) metal itself has been clarified in the double-exchange interaction scheme in which the doped holes at e_g orbital in Mn^{4+} site exhibit a kind of hopping conduction associated with the aligned spins for both Mn^{4+} and Mn^{3+} sites. [22, 25, 16] On the other hand, the CO state is characterized as an antiferromagnetic (AF) spin arrangement on Mn ions, and the Mn^{3+} sublattice retains a cooperative Jahn-Teller distortion, thereby giving rise to a combination of charge, orbital, and magnetic ordering. [25, 16]

Upon heating, both the CO and the CD states transform into a charge-localized paramagnetic insulator (PI) phase, characterized by semiconductive properties.

The switching in d.c. resistivity between CO and CD states, i.e., I-M transition, can be achieved not only by a magnetic field, but also by external stimulation. [4, 5, 10, 11, 12]

I.1.4.3 Discommensuration effect

The CO state has been mostly observed when the concentration of charge carriers takes a rational value of the periodicity of the crystal lattice. [9, 4] The commensurability of the carrier concentration with a periodicity of the crystal lattice is related to the stability of the CO state. In $R_{1-x}A_xMnO_3$, the CO state is optimized at x = 0.5 (commensurate), a deviation of x from 0.5 (discommensuration) decreases the stability of the CO state. Around x = 0.3, the system is on the phase boundary of the transition from the CO insulator state to the FM state, so that the external stimulation causes the transition from the CO state to the FM state with relative ease. [4, 5]

I.1.5 $Pr_{1-x}Ca_xMnO_3$

I.1.5.1 Phase diagram of $Pr_{1-x}Ca_xMnO_3$

The phase diagram as a function of temperature and composition of $Pr_{1-x}Ca_xMnO_3$ has been determined by the measurements of resistivity, magnetization and neutron diffraction as in Figure I - 4. [5, 14, 9]

The sample with x = 0.3 is studied in detail by Y. Tomioka et al.[4, 5] It is an insulator without an external magnetic field at whole temperature range. And it shows the paramagnetic behavior at room temperature (PI), then turns into the COI with the lattice distortion at $T_{CO} \sim 200$ K, successively into the pseudo CE-type AFI with the antiferromagnetic component where the ferromagnetic double-exchange interaction is quenched by a CO effect at Néel temperature $T_N \sim 130$ K, and finally into the canted antiferromagnetic state (CAFI) $T_{CAF} \sim 115$ K.

I.1.5.2 Magnetic structure in $Pr_{0.7}Ca_{0.3}MnO_3$

Figure I - 5 shows the antiferromagnetic component of the $Pr_{0.7}Ca_{0.3}MnO_3$ magnetic structure. This structure is known as the "pseudo-CE" structure, is closely related to the CE-type structure. [14] In the "pseudo-CE" structure, magnetic coupling in the *a-c* plane being identical in each case, with FM-coupled zig-zag AFM chains running along the *a* or *c* axes.

I.1.5.3 Spin glass state

In $Pr_{1-x}Ca_xMnO_3$, the CMR is most pronounced below 80 K. From the neutron diffraction study, the spin glass state is suggested by Yoshizawa et al. [4] There is any other evidence rather than the diffraction which essentially needs long range order while the spin-glass state is short range order.

I.1.6 Insulator-metal transition induced by external field

For the $Pr_{1-x}Ca_xMnO_3$, the collapse of the CO state by magnetic field, which is the transition from the AF-CO state to ferromagnetic (F)-CD (F-CD), was found together with the structural evidence at the low temperature [1].

In the $Pr_{0.7}Ca_{0.3}MnO_3$ system, electric current (by implication of a static electric field) also triggers this AF-CO to F-CD transition at the low temperature [11].

This AF-CO to F-CD transition as a phase-segregation can be driven by synchrotron orbit radiation x-ray exposure (energy 8 keV, flux 5×10^{10} photons/$mm^2 \cdot s^{-1}$) below 40 K [12, 16]. This transition is accompanied by significant change in the lattice structure and can be reversed by thermal cycle, but neither change nor revival of the superlattice reflection intensity is observed when the x-ray beam is switched off after the suppression of the superlattice with synchrotron orbit radiation x-ray exposure. The synchrotron orbit radiation x-ray-induced conductivity is annealed out on heating above 60 K.

Miyano et al. [10] have stated the trace of the collapse of the CO state by observation of photocurrent under the coexistence of the applied electric field and pulse laser irradiation with 1.2 eV in the photon energy range 0.6 eV to 3.5 eV. Thus, there is no x-ray diffraction study of the collapse of the CO state under the laser irradiation to our knowledge.

I.2 Electron Spin Resonance

I.2.1 Paramagnetic resonance

I.2.1.1 The condition for magnetic resonance absorption

We consider electron that possesses a magnetic moment $\boldsymbol{\mu}$ and an angular moment $\hbar\mathbf{S}$. The two quantities are parallel, and we may write

$$\boldsymbol{\mu} = \gamma\hbar\mathbf{S} \; ; \tag{I - 2}$$

where the magnetogyric ratio γ is constant. By convention $\mathbf{S}$ denotes the angular momentum measured in unit of $\hbar$.

The interaction energy with the applied magnetic field is

$$U = -\boldsymbol{\mu}\cdot\mathbf{B}_a \; ; \tag{I - 3}$$

if $\mathbf{B}_a = B_0\mathbf{z}$, then

$$U = -\mu_z B_0 = -\gamma\hbar B_0 S_z \, . \tag{I - 4}$$

The allowed values of S_z are $m_S = S, S-1, \ldots, -S$, and $U = -m_S\gamma\hbar B_0$.

In a magnetic field, an electron with $S = 1/2$ has two energy levels corresponding to $m_S = \pm 1/2$ as in Figure I - 6. If $\hbar\omega_0$ denotes the energy difference between the two levels, then $\hbar\omega_0 = \gamma\hbar B_0$ or

$$\omega_0 = \gamma B_0 \, . \tag{I - 5}$$

This is the fundamental condition for magnetic resonance absorption. For the electron spin,

$$\upsilon(\mathrm{GHz}) = 2.80\, B_0(\mathrm{kG}) = \; 28.0\, B_0(\mathrm{T}). \tag{I - 6}$$

I.2.1.2 Equation of motion

The rate of change of angular momentum of a system is equal to the torque that acts on the system. The torque on a magnetic moment $\boldsymbol{\mu}$ in a magnetic field $\mathbf{B}$ is $\boldsymbol{\mu}\times\mathbf{B}$, so that we have the gyroscopic equation [34, 35, 36]

$$\hbar\frac{d\mathbf{S}}{dt} = \boldsymbol{\mu}\times\mathbf{B}_a \tag{I - 7}$$

or

$$\frac{d\boldsymbol{\mu}}{dt} = \gamma\boldsymbol{\mu}\times\mathbf{B}_a \tag{I - 8}$$

The electron spin magnetization **M** is the sum μ_i in a unit volume. If only a single isotope is important, we consider only a single value of γ, so that

$$\frac{d\mathbf{M}}{dt} = \gamma \mathbf{M} \times \mathbf{B}_a \qquad \text{(I - 9)}$$

I.2.1.3 Longitudinal relaxation time

We place the electron spin in a static field $\mathbf{B}_a = B_0\mathbf{z}$. In thermal equilibrium at temperature T the magnetization will be along **z**:

$$M_x = 0\,; \qquad M_y = 0\,; \qquad M_z = M_0 = \chi_0 B_0 = CB_0/T, \qquad \text{(I - 10)}$$

where the Curie constant $C = N\mu^2/3k_B$.

When the magnetization component M_z is not in thermal equilibrium, we suppose that it approaches equilibrium at a rate proportional to the departure from the equilibrium value M_0:

$$\frac{dM_z}{dt} = \frac{M_0 - M_z}{T_1} \qquad \text{(I - 11)}$$

In the standard notation, T_1 is called the longitudinal relaxation time or spin-lattice relaxation time.

If at t = 0 an unmagnetized specimen is placed in a magnetic field $B_0\mathbf{z}$, the magnetization will increase from the initial value $M_z = 0$ to a final value $M_z = M_0$. Before and just after the specimen is placed in the field, the population N_1 will be equal to N_2, as appropriate to thermal equilibrium in zero magnetic field. It is necessary to reverse some spins to establish the new equilibrium distribution in the field B_0. On integrating Eq. (I - 11):

$$\int_0^{M_z} \frac{dM_z}{M_0 - M_z} = \frac{1}{T_1}\int_0^t dt\,, \qquad \text{(I - 12)}$$

or

$$\log\frac{M_0}{M_0 - M_z} = \frac{t}{T_1}; \qquad M_z(t) = M_0[1 - \exp(-t/T_1)] \qquad \text{(I - 13)}$$

The magnetic energy $-\mathbf{M}\bullet\mathbf{B}_a$ decreases as M_z approaches its new equilibrium value.

I.2.1.4 Transverse relaxation time

If in a static field $B_0\mathbf{z}$ the transverse magnetization component M_x is not zero, then M_x will decay to zero, and M_y as well. The decay occurs because in thermal equilibrium the transverse components are zero.

$$\frac{dM_{\perp}}{dt} = -\frac{M_{\perp}}{T_2} \qquad \text{(I - 14)}$$

where, T_2 is called the transverse relaxation time.

The magnetic energy $-\mathbf{M}\bullet\mathbf{B}_a$ does not change as M_x or M_y changes, provided that $\mathbf{B}_a$ is along **z**. No energy needs to flow out of the spin system during relaxation of M_x, M_y, so that the conditions that determine T_2 may be less strict than for T_1. Sometimes the two times are nearly equal, and sometimes $T_1 >> T_2$, depending on local conditions.

The time T_2 is a measure of the time during which the individual moments that contribute to M_x, M_y remain in phase with each other. Different local magnetic fields at the different spins will cause them to process at different frequencies. If initially the spins have a common phase, the phases will become random in the course of time and the values of M_x, M_y will become zero. We can think of T_2 as a dephasing time.

I.2.1.5 Phenomenological Bloch equation

Taking account of Eq. (I - 11) and Eq. (I - 14), the x, y, and z component of the equation of motion Eq. (I - 9) become

$$\frac{dM_x}{dt} = -\gamma(\mathbf{M}\times\mathbf{B})_x - \frac{M_x}{T_2},$$

$$\frac{dM_y}{dt} = -\gamma(\mathbf{M}\times\mathbf{B})_y - \frac{M_y}{T_2}, \qquad \text{(I - 15)}$$

$$\frac{dM_z}{dt} = -\gamma(\mathbf{M}\times\mathbf{B})_z - \frac{M_0 - M_z}{T_1},$$

respectively, where

$$\mathbf{M} = \delta\mathbf{M} \qquad \text{(I - 16)}$$

$$\mathbf{B} = \mathbf{B}_a + \mathbf{B}_{hf} \qquad \text{(I - 17)}$$

The set of equation is called as the Bloch equation. They are not symmetrical in *x*, *y* and *z* because we have the system with a static magnetic field along **z**. In experiments a rf magnetic field is usually applied along the **x** or **y** axes. Our main interest is in the behavior of the magnetization in the combined rf and static fields. The Bloch equations are plausible, but not exact; they do not describe all spin phenomena, particularly not those in solids.

I.2.1.6 A solution for the Bloch equation.

In carrying forward the solution, we shall find that M_x has components in phase and out of phase with B_x; complex numbers are useful to handle. Taking into account of B_x as the real part of $2B_1e^{i\omega t}$, and take the magnetization M_x to be real part of

$$M_x = \chi \cdot 2B_1 e^{i\omega t} \qquad \text{(I - 18)}$$

where χ is the complex susceptibility

$$\chi = \chi' - i\chi'' \qquad \text{(I - 19)}$$

Then

$$M_x = M_x = \chi' 2B_1 \cos\omega t - i\chi'' 2B_1 \sin\omega t \qquad \text{(I - 20)}$$

With the rotating field Eq. (I - 18) added to $\mathbf{B}_0$, the phenomenological equations are

$$\frac{dM_x}{dt} = \gamma(-M_z B_1 \sin\omega t + B_0 M_y) - \frac{M_x}{T_2},$$

$$\frac{dM_y}{dt} = \gamma(-B_0 M_x + M_z B_1 \cos\omega t) - \frac{M_y}{T_2}, \qquad \text{(I - 21)}$$

$$\frac{dM_z}{dt} = \gamma(-M_y B_1 \cos\omega t + M_x B_1 \sin\omega t) + (M_0 - M_z)/T_1,$$

Defining $M_\pm = M_x \pm iM_y$, we have from the first two equations Eq. (I - 21) that

$$dM_\pm/dt = \gamma\left(\mp iM_z B_1 e^{\pm i\omega t} \pm iB_0 M_\pm\right) - M_\pm/T_2 \qquad \text{(I - 22)}$$

Time dependence in each of equations Eq. (I - 22) can be removed by defining $M_\pm = e^{\pm i\omega t}N_\pm$:

$$\pm i\omega N_\pm = i\gamma\left(\mp M_z B_1 \pm B_0 N_\pm\right) - N_\pm/T_2 \qquad \text{(I - 23)}$$

Now we impose the condition $dM_z/dt = 0$ and seek a solution compatible with it. Since

$$M_y \cos\omega t - M_x \sin\omega t = (1/2i)\,(M_+ e^{-i\omega t} - M_- e^{+i\omega t})$$

the term dM_z/dt in Eq. (I - 22) becomes

$$(M_z - M_0)/T_1 = (\gamma B_1/2I)\,(N_+ + N_-) \qquad \text{(I - 24)}$$

Rearranging Eq. (I - 23) gives

$$N_{\pm} = \frac{\gamma B_1 M_z}{\omega_0 - \omega \pm i/T_2} \qquad \text{(I - 25)}$$

Since N_+ and N_- are complex conjugates, we see immediately from Eq. (I - 24) that M_z is real. Therefore

$$M_z = \chi_0 B_0 \frac{1 + T_2^2 \Delta\omega^2}{1 + T_2^2 \Delta\omega^2 + \gamma^2 B_1^2 T_1 T_2} \qquad \text{(I - 26)}$$

where

$$\Delta\omega = \omega_0 - \omega \qquad \text{(I - 27)}$$

The solution $M_x = 1/2\,(M_+ + M_-) = 1/2(N_+ e^{i\omega t} + N_- e^{-i\omega t})$ is

$$M_x = 1/2\,\chi_0 (\gamma_0 B_0 T_2) \frac{T_2 \Delta\omega\, 2B_1 \cos\omega t + 2B_1 \sin\omega t}{1 + T_2^2 \Delta\omega^2 + \gamma^2 B_1^2 T_1 T_2} \qquad \text{(I - 28)}$$

Comparing with Eq. (I - 21) we identify immediately the complex susceptibility:

$$\chi' = 1/2\,\chi_0 \omega_0 T_2 \frac{T_2(\omega_0 - \omega)}{1 + T_2^2(\omega_0 - \omega)^2 + \gamma^2 B_1^2 T_1 T_2}$$

$$\chi'' = 1/2\,\chi_0 \omega_0 T_2 \frac{1}{1 + T_2^2(\omega_0 - \omega)^2 + \gamma^2 B_1^2 T_1 T_2} \qquad \text{(I - 29)}$$

The average rate A at which energy is absorbed per unit volume by the sample from the B_1 field depends, of course, on the out-of-phase component. We have

$$A = (\omega/2\pi)\int_0^{\pi/\omega} \mathrm{B} \cdot (d\mathrm{M}/dt) = 2\omega\chi'' B_2^2$$

For B_1 small and sharp resonance ($\omega_0 T_2 >> 1$), we obtain

$$A = \frac{\omega(\omega_0 T_2)\chi_0 B_1^2}{1 + T_2^2(\omega_0 - \omega)^2} \qquad \text{(I - 30)}$$

which can be plotted as a function of either ω or ω_0, supposing the other to be constant.

Absorption plotted as a function of slowly varying $\omega_0 = \gamma B_0$ defines a resonance curve with maximum at $\omega_0 = \omega$ having a half-width at a half-maximum of $\Delta\omega_{1/2} = 1/T_2 = \gamma \Delta B_{1/2}$. Thus $1/\gamma T_2 = \Delta B_{1/2}$ is the half-width expressed in units of the external field, which is slowly varied through resonance.

I.2.2 Ferromagnetic resonance

- The transverse susceptibility components χ' and χ'' are very large because the magnetization of a ferromagnet in a given static field is very much larger than the magnetization of electronic paramagnets in the same field.
- The shape of the specimen plays an important role. Because the magnetization is large, the demagnetization field is large.
- The strong exchange coupling between the ferromagnetic electrons tends to suppress the dipolar contribution to the line width, so that the ferromagnetic resonance lines can be quite sharp (<1 G) under favorable conditions.
- Saturation effects occur at low rf power levels. It is not possible, as it is with the electron spin systems, to drive a ferromagnetic spin system so hard that the magnetization M_z is reduced to zero or reversed. The ferromagnetic resonance excitation breaks down onto spin wave modes before the magnetization vector can be rotated appreciably from its initial direction.

Consider a specimen of a cubic ferromagnetic insulator in the form of an ellipsoid with principal axes parallel to *x, y, z*-axes of a Cartesian coordinate system. The demagnetization factors $N_x N_y N_z$ are identical with the depolarization factors. The components of the internal magnetic field $\mathbf{B}^i$ in the ellipsoid are related to applied field by

$$B_x^i = B_x^0 - N_x M_x; \qquad B_y^i = B_y^0 - N_y M_y; \qquad B_z^i = B_z^0 - N_z M_z.$$

The Lorentz fields $(4\pi/3)\mathbf{M}$ and the exchange field $\lambda\mathbf{M}$ do not contribute to the torque because their vector product with $\mathbf{M}$ vanishes identically. In SI unit, we replace the components of $\mathbf{M}$ by $\mu_0\mathbf{M}$, with the appropriate redefinition of the N's.

The components of the spin equation of motion $\mathbf{M} = \gamma(\mathbf{M} \cdot \mathbf{B}^i)$ become, for an applied static field $B_0\mathbf{z}$,

$$\frac{dM_x}{dt} = \gamma\left(M_y B_z^i\right) = \gamma\left[B_0 + \left(N_y - N_z\right)M\right]M_y \text{ and}$$

$$\frac{dM_x}{dt} = \gamma\left[M\left(-N_x M_x\right) - M_x\left(B_0 - N_z M\right)\right] = -\gamma\left[B_0 + \left(N_x - N_z\right)M\right]M_x. \qquad \text{(I - 31)}$$

To first order we may set $dM_z/dt = 0$ and $M_z = M$. Solutions of Eq. (I - 31) with time dependence $\exp(-i\omega t)$ exist if

$$\begin{vmatrix} i\omega & \gamma\left[B_0+\left(N_y-N_z\right)M\right] \\ -\gamma\left[B_0+\left(N_x-N_z\right)M\right] & i\omega \end{vmatrix}=0\ , \qquad \text{(I - 32)}$$

so that the ferromagnetic resonance frequency in the applied field B_0 is

$$\omega_0^2=\gamma^2\left[B_0+\left(N_y-N_z\right)\mu_0\mathrm{M}\right]\left[B_0+\left(N_x-N_z\right)\mu_0\mathrm{M}\right]. \qquad \text{(I - 33)}$$

The frequency ω_0 is called as the frequency of uniform mode, in distinction to the frequency of magnon and other nonuniform modes. In the uniform mode all the moments process together in phase with the same amplitude.

For a sphere $N_x = N_y = N_z$, so that $\omega_0 = \gamma B_0$. For a flat plate with B_0 perpendicular to the plate $N_x = N_y = 0$; $N_z = 4\pi$, whence the ferromagnetic resonance frequency is

$$\textbf{(SI)} \qquad \omega_0=\gamma\left(B_0-\mu_0 M\right). \qquad \text{(I - 34)}$$

If B_0 is parallel to the plane of the plate, the xz plane, then $N_x = N_y = 0$; $N_y = 4\pi$, and

$$\textbf{(SI)} \qquad \omega_0=\gamma\left[B_0\left(B_0+\mu_0 M\right)\right]^{1/2}. \qquad \text{(I - 35)}$$

The experiments determine γ, which is related to the spectroscopic splitting factor g by $-\gamma = g\mu_B/\hbar$. Values of g for metallic Fe, Co, Ni at room temperature are 2.10, 2.18, and 2.21, respectively.

I.2.3 Antiferromagnetic resonance

We consider a uniaxial antiferromagnet with spins on two sublattices, 1 and 2. We suppose that the magnetization $\mathbf{M}_1$ on sublattice 1 is directed along the +z direction by an anisotropy field $B_A\mathbf{z}$; the anisotropy field results from an anisotropy energy density $U_K(\theta_1) = K \sin^2 \theta_1$. Here θ_1 is the angle between $\mathbf{M}_1$ and z-axis, whence $B_A = 2K/M$, with $M = |M_1| = |M_2|$. The magnetization M_2 is directed along the -z direction by an anisotropy field $-B_A\mathbf{z}$. If +z is an easy direction of magnetization, so is -z. If one sublattice is directed along +z , the other will be directed along -z.

The exchange interaction between $\mathbf{M}_1$ and $\mathbf{M}_2$ is treated in the mean field approximation. The exchange fields are

$$\mathbf{B}_1(\mathrm{ex}) = -\lambda\mathbf{M}_2; \qquad \mathbf{B}_2(\mathrm{ex}) = -\lambda\mathbf{M}_1, \qquad \text{(I - 36)}$$

where λ is positive. Here $\mathbf{B}_1$ is the field that acts on the spins of sublattice 1, and $\mathbf{B}_2$ acts on sublattice 2. In the absence of an external magnetic field the total field acting on $\mathbf{M}_1$ and $\mathbf{M}_2$ are

$$\mathbf{B}_1 = -\lambda\mathbf{M}_2 + B_A\mathbf{z}; \qquad \mathbf{B}_2 = -\lambda\mathbf{M}_1 - B_A\mathbf{z}, \qquad \text{(I - 37)}$$

respectively as in Figure I - 7.

In what follows we set $M_1^z = M; M_2^z = -M$. The linearized equations of motion are

$$\frac{dM_1^x}{dt} = \gamma\left[M_1^y(\lambda M + B_A) - M(-\lambda M_2^y)\right];$$

$$\frac{dM_1^y}{dt} = \gamma\left[M(-\lambda M_2^x) - M_1^x(\lambda M + B_A)\right]; \qquad \text{(I - 38)}$$

$$\frac{dM_2^x}{dt} = \gamma\left[M_2^y(-\lambda M + B_A) - (-M)(-\lambda M_1^y)\right];$$

$$\frac{dM_2^y}{dt} = \gamma\left[(-M)(-\lambda M_1^x) - M_2^x(-\lambda M - B_A)\right]; \qquad \text{(I - 39)}$$

We define

$$M_1^+ = M_1^x + iM_1^y; M_2^+ = M_2^x + iM_2^y. \qquad \text{(I - 40)}$$

Then Eq. (I - 38) and Eq. (I - 39) become, for time dependence exp(-$i\omega t$),

$$-i\omega M_1^+ = -i\gamma\left[M_1^+(B_A + \lambda M) + M_2^+(\lambda M)\right];$$

$$-i\omega M_2^+ = -i\gamma\left[M_2^+(B_A + \lambda M) + M_1^+(\lambda M)\right]. \qquad \text{(I - 41)}$$

These equations have a solution if, with $B_E \equiv \lambda M$,

$$\begin{vmatrix} \gamma(B_A + B_E) - \omega & \gamma B_E \\ \gamma B_E & \gamma(B_A + B_E) + \omega \end{vmatrix} = 0. \qquad \text{(I - 42)}$$

Thus the antiferromagnetic resonance frequency is given by

$$\omega_0^2 = \gamma^2 B_A(B_A + 2B_E). \qquad \text{(I - 43)}$$

I.2.4 Measurement

A block diagram of the ESR spectrometer (JEOL-RE1X) is shown in Figure I - 8. Microwave is oscillating at X-band (9.4 GHz) with the Gun diode and is led into the cavity where sample is located. The sample is cooled down by a liq. He continuous-flow type cryostat. Static magnetic field is applied by an electric magnet to split electron spin degeneracy together with modulation magnetic

field (100 kHz). Microwave is absorbed in the sample with many kind of process. Reflected back microwave was detected by the homodyne crystal detector and converted electrical signal as out put.

I.2.5 ESR signal for Mn ions

Recently, behavior of the unpaired $3d$ electron spin in $R_{1-x}A_xMnO_3$ with larger ionic radii of the (A, R) site ion, such as $La_{1-x}Ca_xMnO_3$ were studied by ESR.[37, 38, 39] The most common Mn ion that is measured via ESR is Mn^{2+}, which is generally accepted as not being present in these compounds. Of the two accepted ion species in $R_{1-x}A_xMnO_3$. Mn^{3+} ($3d^4$ with $\boldsymbol{S} = 2$) is unlikely to have an observable ESR signal as it exhibits a large zero-field splitting. To our knowledge, there is only one report about Mn^{3+} ever being seen by ESR.[40] Mn^{4+} ($3d^3$ with $\boldsymbol{S} = 3/2$) has been reported to give an ESR signal but only for a few compounds, and generally at low temperature.[41]

As the observed ESR data are inconsistent with either Mn^{3+} or Mn^{4+}. We can only conclude that the EPR signals are a consequence of some complex magnetic entity made of a collection of Mn^{3+} and Mn^{4+} ions. Further theoretical and experimental effort will be needed to identify the correct description for the ground state spin system.

I.3 Powder X-ray Diffraction

I.3.1 Powder x-ray diffraction

When an x-ray beam is irradiated to an atom, two processes may occur:

(a) The beam may be absorbed with an ejection of electrons from the atom.

(b) The beam may be scattered.

The primary beam is an electromagnetic wave with electric vector varying sinusoidal with time and directed perpendicular to the direction of propagation of the beam. This electric field exerts forces on the electrons of the atoms producing accelerations of the electrons. Using second process, x-ray diffraction analysis, it is possible to get a reciprocal understanding from which the crystal structure details are presented.

Let us deliberate upon the scattering from a group of electrons confined to a small volume such as the volume of an atom. Figure I - 10 illustrates the conditions. The primary x-ray beam, of wavelength λ, has a direction represented by a wave number vector $\mathbf{k}_0$. The electrons are clustered about point O, the position of each represented by a vector $\mathbf{r}_j$ at the position of *j*th electron in an atom. We consider scattering at a point of observation P, at a large distance *R* from the electrons, in a direction given by wave number vector $\mathbf{k}_1$.

At distance R, the observed intensity I_e by scattering from a single free electron with an unpolarized primary beam I_0 directed along the x-ray incidence is expressed by the Thomson scattering equation:

$$\mathrm{I}_e = \mathrm{I}_0 \frac{1}{R^2}\left(\frac{e^2}{mc^2}\right)^2 \frac{1+\cos^2\theta}{2} \qquad \text{(I - 44)}$$

where c is the velocity of light, *e* and *m* are the charge and mass of the electron. The factor $(1+\cos^2\theta)/2$ is called the polarization factor for an unpolarized primary beam.

From Eq. (I - 44), the intensity is weak in inverse proportion as m^2. We consider only the electron for the scattering by an atom because the ratio of the nucleus mass to m is of the order of 10^4.

From Figure I - 10 considering that the source and the point of observation are both at distances very large compared to the length $|\mathbf{r}_j|$, a phase difference ϕ between two wave number vectors, $\mathbf{k}_0$ and $\mathbf{k}_1$, is shown by making the usual plane wave approximations:

$$\phi = \frac{2\pi}{\lambda}(\mathbf{s}_1 - \mathbf{s}_0)\cdot\mathbf{r}_j = (\mathbf{k}_1 - \mathbf{k}_0)\cdot\mathbf{r}_j = \mathbf{K}\cdot\mathbf{r}_j, \mathbf{K} = \mathbf{k}_1 - \mathbf{k}_0, \qquad \text{(I - 45)}$$

where $\mathbf{s}_0$, $\mathbf{s}_1$ are the unit vectors of $\mathbf{k}_0$ and $\mathbf{k}_1$.

The scattering vector **K** expressed by

$$|\mathbf{K}| = 2|\mathbf{k}_0|\sin\theta = \frac{4\pi\sin\theta}{\lambda} \qquad \text{(I - 46)}$$

In scattering from a crystal, it is the elastic scattering, which gives to the Bragg reflection. The inelastic scattering from the different electrons is completely incoherent because of the change in wavelength, and accordingly it produces only a diffuse background. To calculate the elastic scattering from an atom, each electron is spread out into a diffuse cloud of negative charge, characterized by a charge density $\rho(\mathbf{r})$ expressed in electron units. The quantity $\rho(\mathbf{r})\,d\mathbf{r}$ is the ratio of the charge in volume $d\mathbf{r}$ to the charge of one electron, so that for each electron $\int \rho(\mathbf{r})\,d\mathbf{r}=1$. The wave mechanical treatment then says that the amplitude of elastic scattering from the element $\rho(\mathbf{r})\,d\mathbf{r}$ is equal to $\rho(\mathbf{r})\,d\mathbf{r}$ times the amplitude of scattering from a single electron. To get the total amplitude of elastic scattering from one electron, we must integrate over the volume occupied by the electron, and in doing this make proper allowance for the phase of the contribution from each element $\rho(\mathbf{r})\,d\mathbf{r}$.

The amplitude of quantity represented by the integral is called f, the atomic scattering factor per electron:

$$f = \int e^{\mathbf{K}\cdot\mathbf{r}}\rho(\mathbf{r})d\mathbf{r} \qquad \text{(I - 47)}$$

Stated in another way, f is the amplitude of elastic scattering per electron, expressed in electron units.

By scattering from an atom the observable quantity is only intensity $I_0(\mathbf{K})$ as in Figure I - 11. Using Eq. (I - 44), the intensity is given by

$$I_0(\mathbf{K}) = I_e f^2 = \frac{I_0}{R^2}\left(\frac{e^2}{mc^2}\right)^2 \frac{1+\cos^2 2\theta}{2} f^2 \qquad \text{(I - 48)}$$

We consider an unpolarized monochromatic beam falling on a small single crystal. Figure I - 10 shows the conditions.

The scheme of repetition is defined by three vectors (**a**, **b**, **c**) called the crystal axes. It is only the magnitude and a direction of the repeating displacements that is of importance, and hence for present purposes, the position chosen as origin is immaterial. The parallelepiped defined by the three axes (**a**, **b**, **c**) is the smallest volume which repeated will make up the crystal This smallest volume is called the unit cell.

Relative to a crystal origin at O, the position of the atom of type j in unit cell n(n_1, n_2, and n_3) is given by the vector

$$\mathbf{R}_{nj} = n_1\mathbf{a} + n_2\mathbf{b} + n_3\mathbf{c} + \mathbf{r}_j \cdot \qquad \text{(I - 49)}$$

The summation over j involves the positions $\mathbf{r}_j$ of the different atoms in the unit cell, and hence it varies from one structure to another. It is called the structure factor and designated by $F(\mathbf{K})$, where

$$F(\mathbf{K}) = \sum_j f_j e^{i\mathbf{K}\cdot\mathbf{r}_{nj}} \cdot \qquad \text{(I - 50)}$$

For purpose of crystal structure determinations, the structure factor $F(\mathbf{K})$ plays a very important role, since it is only on the structure factor that the atomic positions appear.

The resultant field at P due to all the atoms in the crystal is then obtained by summing over j to include all the atoms in a unit cell, and summing over n to include the entire unit cells. For simplicity we shall assume that the crystal has the shape of a parallelepiped with edges $N_1\mathbf{a}$, $N_2\mathbf{b}$, $N_3\mathbf{c}$ parallel to the crystal axes ($\mathbf{a}$, $\mathbf{b}$, $\mathbf{c}$). This restriction will be removed when we consider the integral intensity. The composite amplitude is expressed by

$$\mathrm{A}(\mathbf{K}) = \sqrt{\mathrm{I}_e}\sum_{n,j} f_j e^{i\mathbf{K}\cdot\mathbf{R}_{nj}}$$

$$= \sqrt{\mathrm{I}_e}F(\mathbf{K})\sum_{n_1,n_2,n_3} e^{i\mathbf{K}\cdot(n_1\mathbf{a}+n_2\mathbf{b}+n_3\mathbf{c})} \qquad \text{(I - 51)}$$

Hence value of the intensity at the point of observation is expressed by

$$\mathrm{I}_0(\mathbf{K}) = |\mathrm{A}(\mathbf{K})|^2$$

$$= \mathrm{I}_e F(\mathbf{K})F(\mathbf{K})^* \frac{\sin^2(N_1\mathbf{K}\cdot\mathbf{a})}{\sin^2(\mathbf{K}\cdot\mathbf{a})}\frac{\sin^2(N_2\mathbf{K}\cdot\mathbf{b})}{\sin^2(\mathbf{K}\cdot\mathbf{b})}\frac{\sin^2(N_3\mathbf{K}\cdot\mathbf{c})}{\sin^2(\mathbf{K}\cdot\mathbf{c})}, \qquad \text{(I - 52)}$$

where

$$\mathrm{I}_0(\mathbf{K}) = \mathrm{I}_e|F(\mathbf{K})|^2 L(\mathbf{K}) \qquad \text{(I - 53)}$$

$$L(\mathbf{K}) = \frac{\sin^2(N_1\mathbf{K}\cdot\mathbf{a})}{\sin^2(\mathbf{K}\cdot\mathbf{a})}\frac{\sin^2(N_2\mathbf{K}\cdot\mathbf{b})}{\sin^2(\mathbf{K}\cdot\mathbf{b})}\frac{\sin^2(N_3\mathbf{K}\cdot\mathbf{c})}{\sin^2(\mathbf{K}\cdot\mathbf{c})}. \qquad \text{(I - 54)}$$

Eq. (I - 52) depends sharply upon the Laue function L($\mathbf{K}$). The intensity $\boldsymbol{I}_0(\mathbf{K})$ will be essentially

zero unless the three terms of Eq. (I - 54) are simultaneously close to their maximum values, $N_1^2 N_2^2 N_3^2 = N^2$. For $\boldsymbol{I}_0(\mathbf{K})$ to be a maximum, it must simultaneously satisfy the three conditions

$$\begin{aligned} \mathbf{K} \cdot \mathbf{a} &= 2\pi h \\ \mathbf{K} \cdot \mathbf{b} &= 2\pi k \\ \mathbf{K} \cdot \mathbf{c} &= 2\pi l \end{aligned} \qquad \text{(I - 55)}$$

where h, k, l are three integers, these are called Mirrer indices.

Since a diffracted beam exists only if Eq. (I - 56) are simultaneously satisfied, these three equations together must be equivalent to the Bragg law. Because the spacing of the hkl- planes $d_{hk}l$ is the perpendicular distance between the planes, Bragg law is expressed by

$$2d_{hkl} \sin\theta = \lambda \quad \cdot \qquad \text{(I - 56)}$$

Let a arbitrary scattering vector K are represented in terms of the reciprocal vectors:

$$\mathbf{K} = \mathbf{K}_h = h\mathbf{a}^* + k\mathbf{b}^* + l\mathbf{c}^* \qquad \text{(I - 57)}$$

All the electrons in the atom are combined by means of the atomic scattering factor in Eq. (I - 47). From Eq. (I - 50), all the atoms in the unit cell are combined by means of a structure factor:

$$F(\mathbf{K}) = v\int_0^1 \rho(xyz) e^{2\pi i(hx+ky+lz)} dxdydz \qquad \text{(I - 58)}$$

where v is the volume of a unit cell

$$dv = dxdydz \qquad \text{(I - 59)}$$

For purposes of an hkl-reflection, $F(\boldsymbol{K})_{hkl}$ is the effective number of electrons concentrated at the cell origin.

At the method for representing a crystalline structure, a continuous electron density function $\rho(xyz)$ may be expressed in electrons per unit volume and including all the electrons in the cell. Since $\rho(xyz)$ is triply periodic, it can be expressed by a triple inverse Fourier transform in the distances x, y *and* z parallel to the a-, b-, and c-axes:

$$\rho(x,y,z) = \frac{1}{v}\sum_{hkl} F(\mathbf{K})\, e^{-2\pi i(hx+ky+lz)}. \qquad \text{(I - 60)}$$

The trouble comes from the fact that what we measure is some sort of an integrated intensity, and this is proportional to $F_{hkl}F^*_{hkl}$ even if all the F_{hkl} are real, what we measure is still a quantity proportional to F_{hkl}^2 since Eq. (I - 53), and we obtain the magnitude of all the coefficients of Eq. (I - 60) but not their signs. Hence Eq. (I - 60) represents the electron density $\rho(x,y,z)$ by a Fourier

transformation in which the magnitudes of all the coefficients can be determined from experiment, but for which the phrases are unknown. The trouble is called the phase problem.

I.3.2 Refinement of crystal structure by Rietveld method

Since the advent of the Rietveld method (Rietveld, 1969), this kind of analysis has been used for the crystal structure refinement and the analysis of x-ray powder diffraction data. A FORTRAN program named RIETAN [42] was developed in Japan for Rietveld analysis of angular-dispersive x-ray powder data.

In RIETAN, the profile parameters are refined based on a given structural model [43]. One usually proceeds in steps in Rietveld analysis, first refining only one or two parameters and then gradually letting more and more of the parameters be simultaneously optimized in the successive least-squares refinement cycle. The least-squares method finds the optimum solution $\boldsymbol{x}$ for minimizing function s ($\boldsymbol{x}$) that is given by

$$s(\mathbf{x}) = \sum_i \omega_i \{y_i - f_i(\mathbf{x})\}^2, \qquad \text{(I - 61)}$$

where $\boldsymbol{x}$ is the vector of variable parameters, i is the step number, y_i is the observed intensity, f_i is the calculated intensity, and ω_i (= $1/y_i$) is the weight based on counting statistics.

We use techniques for nonlinear least-squares fitting by the modified Marquardt method [44], which is improved Gauss-Newton method.

In Gauss-Newton algorithm, changes in n variable parameters at each iterative step, matrix, are calculated by:

$$\mathbf{A}\Delta\mathbf{x} = N, \qquad \text{(I - 62)}$$

where $\boldsymbol{A}$ is the coefficient matrix with $n \times n$, and both $\Delta\boldsymbol{x}$ and $\boldsymbol{N}$ are $n \times 1$ column matrices.

The modified Marquardt method also calculates $\boldsymbol{A}$ and $\boldsymbol{N}$, but adds a term of diagonal matrix to $\boldsymbol{A}$ stabilized the convergence to the minimum:

$$\mathbf{A} + \lambda \cdot diag(\mathbf{A})\Delta\mathbf{x} = \boldsymbol{N} \qquad \text{(I - 63)}$$

where λ is Marquardty parameter, and diag($\boldsymbol{A}$) is diagonal matrix by the diagonal elements comprised in $\boldsymbol{A}$.

Let $\lambda = 0$, we obtain the Gauss-Newton solution as Eq. (I - 63). On the other hand, as λ becomes larger $\lambda << |\boldsymbol{A}|$:

$$\Delta \mathbf{x} \cong \frac{N}{\lambda}. \qquad \text{(I - 64)}$$

Accordingly, Δx tends towards the steepest drop direction. The value of λ can take automatically adjusted during a sequence of iterations using a most efficient algorithm, which implements the high performance process by the Marquardt method. The modified Marquardt method is very effective for arranging nonlinear model functions $f_i(x)$ or problems in which initial values for parameters differ remarkably from the true ones.

Rietveld was given the profile shape function by

$$\phi(2\theta_i - 2\theta_K) = \mathbf{F}(2\theta_i - 2\theta_K)a(2\theta_i - 2\theta_K) \qquad \text{(I - 65)}$$

where $2\theta_i$ is the diffraction angle, $2\theta_K$ is the reflection K with Bragg angle, $F(2\theta_i - 2\theta_K)$ is a symmetrical profile shape function, and $a(2\theta_i - 2\theta_K)$ is an asymmetrical correction. As symmetrical profile shape function in program RIETAN, a modified pseudo-Voigt function is used in which the Gauss-Lorentz functions may have equal peak heights and full-width-at-half-maximum intensity. It is simple profile shape function, which fits well the Bragg reflection profiles in x-ray (or neutron) scattering diffraction, empirically.

Consequently, even if initial parameters are far from the true solution, incremental refinements enable very stable convergence to an optimum solution in most metals and inorganic compounds of good crystallinity.

References

1. C. Kittel : " Introduction to Solid State Physics", 6 Edition (1986), John Wiley & Sons Inc., New York, Chap. 13, E. Siegel and K. A. Müller : Phys. Rev. B **20**, 3587 (1979), E. Sawaguchi, Y. Akishige and M. Kobayashi : J. Phys. Soc. Jpn., **54**, 480 (1985).
2. J. G. Bednorz and K. A. Müller : Phys. B **64**, 189 (1986).
3. T. Ida, W.-Z. Hu, M. Izumi, K. Nakanishi, S. Adachi, K. Tanabe, S. Tanaka, Y. Sasago, and K. Uchinokura : NATO Advanced Science Institute, 3/26R, 337 (1997), K. Nakanishi, S. Adachi, K. Tanabe, W.-Z. Hu, T. Ida, and M. Izumi : Advances in Superconductivity IX, 273, (1997), S. Adachi, K. Nakanishi, K. Tanabe, W.-Z. Hu, M. Izumi, N. E. Hussey, K. Nozawa, and H. Takagi : ISS'99 Abstract, (1999).
4. H. Yoshizawa, H. Kawano, Y. Tomioka and Y. Tokura, Phys. Rev., B **52**, 13145 (1995).
5. Y. Tomioka, A. Asamitsu, H. Kuwahara, and Y. Moritomo, Phys. Rev., B **53**, 1689 (1996).
6. S. Jin, T. H. Tiefel, M. McCormack, R. A. Fastnacht, R. Ramesh, L. H. Chen, Science, **264**, 413 (1994).
7. H. Chiba, M. Kikich, K. Kusaba, Y. Muraoka and Y. Syono : Solid State Commun, **99** 499 (1996).
8. E. O. Wollan and W. C. Koeiiler : Phys. Rev., 100, 545 (1955).
9. Z. Jirak, S. Krupicka, Z. Simsa and M. Dlouha and S. Vratislav, J. Mag. Mag. Mat. **53**, 166 (1985).
10. K. Miyano, T. Tanaka, Y. Tomioka and Y.Tokura : Phys. Rev. Lett., **78**, 4257 (1997).
11. A. Asamitsu, Y. Tomioka, H. Kuwahara, and Y. Tokura, *Nature*, **388**, 50 (1997).
12. V. Kiryukhin, D. Casa, J. P. Hill, B. Keimer, A. Vigilante, Y. Tomioka, and Y. Tokura : Nature, **386**, 813 (1997).
13. P. G. Radaelli, D. E. Cox, M. Marezio, and S-W. Cheong : Phys. Rev., B 55, 3015 (1997).
14. E. Pollert, S. Krupicka and E. Kuzmicova, J. Phys. Chem. Solids **43**, 1137 (1982).
15. Z. Jirak, S. Krupicka, V. Nekvasil, E. Pollert, G. Villeneuve and F. Zounova:J. Mag. Mag. Mat. **15-18**, 519 (1980).
16. D. E. Cox, P. G. Radaelli, M. Marezio, S-W. Cheong : Phys. Rev. B, **57**, 3305 (1998).
17. V.B. Podobedov, A. Weber, D.B. Romero, J.P. Roce and H.D. Drew : Sot. Stat. Com., **105**, 589 (1998).
18. M. N. Iliev, M. V. Abrashev, H.-G. Lee, V. N. Popov, Y. Y. Sun, C. Thomsen, R. L. Meng and C. W. Chu, Phys. Rev. B, 57, 2872 (1998)
19. Y. Okimoto, T. Katsufuji, T. Ishikawa, T. Arima and Y. Tokura : Phys. Rev., B 55, 4206 (1997).
20. G. Allodi, R. De Renzi, and Guidi, F. licci, M. W. Pieper : Phys. Rev., B 56, 6036 (1997).
21. Y. Murakami, H. Kawada, H. Kawata, M. Tanaka, T. Arima, Y. Morimoto, and Y. Tokura : Phys. Rev. Lett., 80, 1932 (1998).

22. C. Zener, *Phys. Rev.*, **82** , 403 (1951).
23. P.W. Anderson and H. Hasegawa, *Phys. Rev.*, **100**, 675 (1955).
24. J.B. Goodenough, *Phys. Rev.*, **100**, 564 (1955).
25. A. J. Millis, P. B. Littlewood, and B. I. Shainman : Phys. Rev. B, **74**, 5144 (1995).
26. A. J. Millis, Boris I. Shraiman, and R. Mueller, Phys. Rev. Lett., **77**, 175 (1996).
27. A. J. Millis, Nature, **392**, 147 (1998).
28. P.-G. Gennes : Phys. Rev., **118**, 141, (1960).
29. D. Feinberg, P. Germain, M. Grilli, G. Seibold, *Phys. Rev. B.*, **57**, 5583 (1998).
30. Y. Tomioka, A. Asamitsu, Y. Moritomo, H. Kuwahara, and Y. Tokura : Phys. Rev. Lett., 74, 5108 (1995).
31. H. Kuwahara, Y. Tomioka, A. Asamitsu, Y. Moritomo, and Y. Tokura : Science 270, 961 (1995).
32. V. I. Anisimov, I. S. Elfimov, M. A. Korotin and K Terakura : Phys. Rev., B 55, 15494 (1997).
33. H. Y. Hwang, P. Dai, S-W. Cheong, G. Aeppli, D. A. Tennant, and H. A. Mook : Phys. Rev. Let.t, B 53, 1316 (1998).
34. S. A. Al'tshuler and B. M. Kozvrev : " Electron Paramagnetic Resonace", Academic Press, New York, (1964).
35. G. E. Pake : " Paramagnetic Resonace ", W.A. Benjamin Inc., New York, (1962).
36. C. Kittel : " Introduction to Solid State Physics", 6 Edition, John Wiley & Sons Inc., New York, Chap. 16, (1986).
37. S. B. Oseroff, M. Torikachvili, J. Singley, S. Ali, S.-W. Cheong and S. Schultz : Phys. Rev. B, **53**, 6521 (1996).
38. A. Shengelaya, Guo-meng Zhao, H. Keller, and K. A. Müller : Phys. Rev. Lett., **77**, 5296 (1996).
39. O. Chauvent, G. Goglio, P. Molinie, B. Corraze and L. Brohan : Phys. Rev. Lett., **81**, 1102 (1996).
40. H. J. Gerritsen and E. S. Sabisky : Phys. Rev., **132**, 1507 (1963).
41. K. A. Muller et al. : Solid State Commun. **61**, 21 (1987).
42. F. Izumi : "The Rietveld Method", ed. by R.A. Young, Oxford University Press, Oxford, Chap. 13, (1993).
43. International Tables for Crystallography, Vol. A, Space-Group Symmetry, ed. by Hahn theo, D. Reidel Publishing Com., Dordrecht: Holland/Boston (U.S.A.) (1983).
44. R. Fletcher, Harwell Report, AERE-R, 6799, (1971).

Chapter II
Magnetic and Structural Behavior in $Pr_{0.65}Ca_{0.35}MnO_3$ Powder

II.1 Introduction

In this chapter, the powder form of $Pr_{1-x}Ca_xMnO_3$ (x = 0.35) is studied. [1] As has been noted, the reason of the choice of the material is coming from a few earlier bibliographies reported a sign of the possibility of a photo-induced effect on the magnetic and electronic state in this composition. The energy of the irradiated photon was ranged from near infrared to SOR light, which has made confused understanding. Some of them stated that a photo-induced I-M transition may occur as well as the CMR. Our motivation and task of the present thesis are to get an answer for the question; what is exactly going on in the spin and orbital system under the photon injection? As we describe later, with respect to the photo-induced effect we investigate the spin system and the charge system by the ESR and x-ray diffraction, respectively. They are strikingly a couple of complimentary ways to the task. Below we describe the ordinary magnetic and structural properties without the photon injection studied by our group on the present powder sample.

In the present compound, the structural phase transition associated with the formation of the CO state occurs and the Mn^{3+} and Mn^{4+} alternation retains down to around lig. He temperature. Successive magnetic transitions form the AF spin structure with spin canting at low temperature. Powder x-ray diffraction shows the onset of the CO state at $T_{CO} \sim 215$ K from the appearance of superlattice peak due to the CO structure and gives a sign of the growth of the spin canting in the AF order at $T_{CAF} \sim 125$ K. The ESR revealed the characteristic behavior of $3d$-t_{2g} and $3d$-e_g eletronic spin state on Mn^{3+} and Mn^{4+} ionic sites. The result from the ESR provide an evidence of the formation of AF order at 180 K. The obtained resonance profile exhibits the broadening of linewidth associated with the enhancement of the intensity below the onset temperature of the CAF phase. A complemental information with the ESR is also given by static magnetization from d.c SQUID magnetometer measurement. The magnetoresistance verifies a magnetic field induced I-M transition, so called CMR, in the CAF phase (5.5 T at 80 K). Below, we show the above results in detail.

II.2 Experiment

II.2.1 Sample preparation of $Pr_{0.65}Ca_{0.35}MnO_3$ powder

The powder sample of $Pr_{0.65}Ca_{0.35}MnO_3$ was prepared by using the usual ceramic technique. [1, 2, 3] The mixture of manganese, calcium carbonates and praseodymium oxide was ground and pre-calcined at 600 °C for 6 h. Then the powder was pressed into pellet and calcined again at 1200 °C for 12 h in the air by the electric furnace (TSS. 530. P; Yamada Denki Co. LTD., Japan) and cooled down to room temperature with 100 °C / h. The pellet was ground into powder again. The powder sample was used for the ESR, d.c. magnetization, and the powder x-ray diffraction measurements. For d.c. resistivity measurement, the pellet was used.

II.2.2 Powder x-ray diffraction

Prior the ESR study, we performed the powder x-ray diffraction to verify the existence of single $Pr_{0.65}Ca_{0.35}MnO_3$ phase and to get the atomic parameter as a function of temperature from 300 K down to 10 K.

This sample was attached to quartz sample holder which was mounted on a liq. He closed-cycle type cryostat. The sample temperature was monitored by a thermometer located close to the sample and was controlled within ± 0.1 K. Data were collected using laboratory powder x-ray diffractometer (MXP18; Mac Science Co., Japan) with Cu $K\alpha$ radiation equipped with a rotating anode generator operated at 40 kV and 200 mA. Figure II - 1 shows schematic view of optical component of the laboratory powder x-ray diffractometer. The θ - 2θ step scan mode was used with the step width $\Delta\theta$ = 0.01° - 0.02°, accumulation time 10 - 100 s/step, and scan range 15° - 100° in 2θ.

The calculation of the observed structure factor together with both profile fitting process and the refinement of crystal structure based on the powder diffraction data was performed by Rietveld method with a program RIETAN.[4]

II.2.3 Electron spin resonance measurement

The ESR measurement for the electron spins on Mn^{3+} and Mn^{4+} ionic sites in $Pr_{0.65}Ca_{0.35}MnO_3$ was done using X-band (9.4 GHz) spectrometer (JES-RE1X; JEOL Co., Japan) with 100 kHz field modulation. The amount of the powder sample was 0.5 mg. The sample was mounted in a liq. He continuous-flow type cryostat and was cooled from 300 K down to 10 K. The sample temperature

was monitored by a thermometer located near the sample and was controlled within ±0.5 K. The reproducibility of the measured ESR signals was checked several times.

The resonance absorption of the ESR measurement were observed as a deviative signal curves. Then they were fitted to a Lorentzian curve as shown in

$$I(H) = \frac{I_m}{1+\left(\frac{H_0 - H}{\Delta H_{1/2}/2}\right)^2} ; \qquad \text{(II - 1)}$$

$$\Delta H_{1/2} = \sqrt{3}\Delta H_{p-p} ; \qquad \text{(II - 2)}$$

where ΔH_{p-p}, H_0 and I_m are the linewidth, the central resonace field and ESR intensity at H_0. Then resultant curves were made.

The ESR linewidths ΔH_{p-p}, from which one can estimate the spin-spin interaction through the spin-spin relaxation time, were taken from the half-amplitude linewidth of integration of these curves.

The effective spin susceptibility $\chi_{eff.}$ was obtained from 2 times successive integration of the obtained profile with references to $CuSO_4 \cdot 5H_2O$ whose effective spin susceptibility is well known and Mn marker which is Mn^{2+} ions diluted with MgO.

II.2.4 D.c. magnetization and transport property measurement

II.2.4.1 D.c. magnetization measurement

Static magnetic susceptibility was measured by the variable temperature susceptometer, utilizing superconducting devices, which operates between 2.0 K and 400 K with the magnetic field up to 5.5 T. In this system, rf-SQUID (Superconducting QUantum Interference Device) operated by ac-bias current is used. The rf-SQUID-based flux measurement system consists of flux-transfer circuit and rf-SQUID coupled with so-called tank circuit. Schematic measurement diagram is shown in Figure II - 2. The flux-transfer circuit links the pickup coil (L_1) to the coil (L_2) through twisted and covered superconducting wire leads. Heater circuit is attached to the leads. It is necessary to destroy the superconducting closed loop when we change the magnetic field. Total external flux (f_x) for rf-SQUID is the sum of f_{DC} (flux at L_2) due to the sample and f_{rf} (flux at L_{rf}) originating from rf-current in tank circuit. In hysteric mode operation, variation of the voltage (V_{rf}) with the periodicity

of flux-quanta (2 x 10^{-7} Gauss.cm^2) occurs for the averaged value of f_x. This variation of V_{rf} is interpreted to the variation of the Q-value of the tank circuit because R is the effective resistance, which gives the Q of the circuit. The sample-induced flux change was determined by moving the sample between a pair of counterwound coils, each of which is connected to a rf-SQUID-based system described above. Observed error of the absolute value of the susceptibility in standard sample was about 3%. The resolution of this system in magnetic moment was 10^{-7} Gauss. Thus it is possible that the resolution of the susceptibility under 1 T is up to 10^{-11} emu.

The samples were placed in a plastic straw stuffed cotton and fixed by Kapton film. The magnetic moments of cotton thread, the tiny cup and Aronalpha were measured separately. The contribution of these materials to the magnetic susceptibility was subtracted from the measured value to obtain the intrinsic magnetic moment of the sample. Typical amount of the sample was about 0.5 mg.

The d.c. magnetization under the magnetic field 0.01 T by SQUID susceptometer in the warming run after field cooling run (FC(W)), the cooling run after field cooling run (FC(C)) and the zero field cooling run (ZFC) were measured. In the zero field cooling run (ZFC), measurements were performed after sample was cooled down to a prescribed temperature under zero field, then a field was raised to 0.01 T.

II.2.4.2 Transport property measurement

Temperature dependence of d.c. resistivity was measured with the usual 4-point method under zero field and magnetic field (H = 6 T) from 300 K down to 10 K using superconducting magnet (MagLab 2000; OXFORD Instrument Co., England). Magnetic field dependence of d.c. resistivity was also measured from 0 T up to 6 T at 80 K where the strong suppression of CO state occurs with the external field.

II.3 Results and discussion

II.3.1 Structure and atomic parameter

Figure II - 3 shows the powder x-ray diffraction profile for $Pr_{0.65}Ca_{0.35}MnO_3$ at 290 K together with the result of the profile fit by Rietveld analysis with solid curve. The powder x-ray diffraction analysis indicated that the sample was in single phase with the distorted perovskite structure and symmetry is orthorhombic with the space group Pbnm. The lattice constants are a = 5.428 Å, b = 5.455 Å and c = 7.663 Å at 290 K. The grain size is about 20 μm.

Space group	*Pbnm*		
Symmetry	Orthorhombic		
Lattice constants	a = 5.428 Å	b = 5.455 Å	c = 7.663 Å
	x	y	z
Mn (4b)	1/2	0	0
Pr/Ca (4c)	-0.008	0.0309	1/4
O_I (4c)	0.059	0.487	1/4
O_{II} (8d)	-0.287	0.286	0.035

Table II - 1 Atomic parameter for $Pr_{0.65}Ca_{0.35}MnO_3$ at 290 K determined with the powder x-ray diffraction profile.

Figure II - 4 exhibits the lattice constants as a function of temperature from 300 K down to 10 K from the powder x-ray diffraction measurement. The lattice parameters decrease with decreasing temperature and they exhibit a discontinuity around 215 K which is assigned as the trace of the onset of CO transition. Below 215 K, the lattice constants show the change in the temperature dependence of the length of unit cell around 115 K corresponding to the onset of CAFI state.

II.3.2 Superlattice structure in the CO state

Figure II - 5 shows the powder x-ray diffraction profiles at 296 K, 190 K, 100 K and 50 K. It is clear that some additional diffraction peaks appear below 190 K which is close to $T_{CO} \sim 215$ K. The integrated intensities of the peaks assigned as Bragg reflections based on the unit cell

parameters at 296 K are almost the same above and below T_{CO}. According to the indices as shown in Figure II - 5, the newly appearing peaks are assigned successfully as superlattice reflections with the unit cell parameters at 296 K. In Figure II - 5, a superlattice structure, **a** x 2**b** x **c** relative to the unit cell at 296 K has been confirmed below 200 K, which conducts a further complemental evidence for the CO state associated with the alternation of Mn^{3+} and Mn^{4+} ions. [3, 5] The observed superlattice reflection lines remain down to 50 K via T_{AF}, and T_{CA}, which confirms that the CO state is retained without external stimulation such as electric, magnetic field and etc.

II.3.3 Electrical transport property

Figure II - 6 shows the temperature dependence of the differential resistance (dR/dT) of $Pr_{0.65}Ca_{0.35}MnO_3$ powder sample. It is semiconductor-like without external magnetic field at whole temperature range. The dR/dT shows a prominent peak which is evident due to the second-order phase transition associated with formation of the CO state where the charge is localized on Mn ionic site at $T_{CO} \sim 215$ K together with the Mn^{3+} and Mn^{4+} alternation leading to the superlattice x-ray reflection.

Figure II - 7 shows the magnetic field dependence of the resistance, R of $Pr_{0.65}Ca_{0.35}MnO_3$ powder sample at 80 K. The powder sample shows a CMR effect $(R_M-R_0)/R_0 \sim 400$ % with a threshold magnetic field of about 2 T at the CO state below $T_{CO} \sim 215$ K.

II.3.4 Successive magnetic transitions studied by ESR

II.3.4.1 ESR profile

Figure II - 8 shows the temperature dependence of the ESR profiles for $Pr_{0.65}Ca_{0.35}MnO_3$ powder sample from 300 K to 120 K. The ESR profiles clearly show the Lorentzian shape above 100 K, which has made to parameterize the resonance profiles in frame of the Lorentzian function with relative ease.

Figure II - 9 shows the temperature dependence of the ESR linewidth ΔH_{p-p} (+) and the effective spin susceptibility, $\chi_{eff.}$ (o). The ESR linewidth, ΔH_{p-p} decreases linearly with decreasing temperature leading to the paramagnetic (P) character. Below $T_{CO} \sim 215$ K, the ΔH_{p-p} increases down to $T_{AF} \sim 180$ K with the association of the formation of AF order, and subsequently decreases below T_{AF}, which shows that the exchange interaction is enhanced and forms the AF state, and finally increases abruptly below $T_{CAF} \sim 125$ K showing that the AF exchange interaction is reduced and spin

configuration is away from the precise antiparallel configuration. We can assign T_{AF} as ~ 180 K from the existence of the peak in the temperature dependence of ESR linewidth ΔH_{p-p}. The T_{AF} has been a difficulty to determine in the magnetization measurement so far.

The effective spin susceptibility $\chi_{eff.}$ increases up to T_{CO} with decreasing temperature which is a sign of the paramagnetic state behavior. Then it decreases down to T_{CAF} ~ 125 K which can be interpreted that the AF ordering starts to form before the AF transition. Finally it shows a spontaneous magnetization below T_{CAF} ~ 80 K because of the appearance of the F components in the CAF state. There is a cusp structure near T_{AF} which corresponds to the AF transition.

II.3.4.2 Origin of ESR signal

It is necessary to clarify the origin of the ESR signal in the perovskite manganese for understanding the behavior of the observed ESR profiles in $Pr_{0.65}Ca_{0.35}MnO_3$, the ESR linewidth ΔH_{p-p} and the effective spin susceptibility $\chi_{eff.}$

Recently, Oseroff *et al.* [6, 7] reported the observation of an electron paramagnetic resonace (EPR) signal in $La_{1-x}Ca_xMnO_{3+y}$ compounds with different Ca and oxygen content. They also observed strong EPR signals with an unconventional temperature dependence and suggested that a cooperative spin entity could be responsible for this signal. They proposed that the EPR signal observed in $La_{1-x}Ca_xMnO_{3+y}$ is due primarily to Mn^{4+} ($3d^3$ with $S = 3/2$) ions. Consequently the spin-lattice relaxation is weak, and this makes EPR of Mn^{4+} easy to be observed even at high temperatures [8]. The Mn^{3+} ($3d^4$ with $S = 2$) is unlikely to have an observable EPR signals as it exhibits a large zero-field splitting and strong spin-lattice relaxation (the ground state of the Mn^{3+} ion is the orbital doublet) [9].

However, it is clear that the observed signal cannot be attributed to isolated Mn^{4+} ions. To construct a model of paramagnetic centers responsible for these EPR signals, it is important to point out that doped manganese perovskites are mixed valence compounds with Mn^{4+} and Mn^{3+} ions and strong ferromagnetic double exchange interaction between them. Thus, Shengelaya *et al.* [7] consider the EPR response of the system to contain three distinct components: Mn^{4+} ions, *s*; Mn^{3+} ions, σ; and the lattice, *L*. Figure II - 10 shows a standard schematic picture for such a system, with arrows indicating possible relaxation paths between components. The theory used to describe such a system was developed in connection with the EPR of localized magnetic moments in metals by Barnes.[10] Later, Gulley and Jaccarino [11] applied this formalism to study the EPR of strongly exchange-coupled insulators with two types of paramagnetic ions. In order to describe the spin

relaxation process in $La_{1-x}Ca_xMnO_{3+y}$, Shengelaya *et al.* consider the schematic block diagram shown in Figure II - 10. Assuming that the relaxation rate $R_{\sigma L}$ of the Mn^{3+} spins to the lattice is much smaller than the exchanged-induced cross relaxation rate $R_{\sigma s}$ (and back $R_{s\sigma}$) between Mn^{3+} and Mn^{4+}, and if the direct relaxation of Mn^{4+} ions to the lattice R_{sL} is negligible ($R_{\sigma L}$, $R_{sL} << R_{\sigma s}$, $R_{s\sigma}$), then a so-called "bottleneck" effect will take place in the transfer of energy between the spin subsystems [10]. In this limit, magnetic energy, which is transferred from the Mn^{4+} to the Mn^{3+} spin system, is quite likely to be returned back rather than passed to the lattice. Consequently, the relaxation of the system is dominated by the bottleneck due to the slow Mn^{3+} -lattice relaxation process. Recently, the concept of a bottleneck was successfully applied by Kochelaev *et al.* [12] to explain the EPR of Mn ions in the cuprate superconductor $La_{2-x}Sr_xCuO_4$ in which antiferromagnetic coupling is present. This concept is also helpful in explaining the peculiar EPR features in $La_{1-x}Ca_xMnO_{3+y}$ and is our starting point for the interpretation of the experimental results.

II.3.4.3 D.c. magnetization

Figure II - 11 shows the temperature dependence of d.c. magnetization under 0.01 T. It is gratifying to confirm a complete correspondence between the magnetic behavior observed in the magnetization measurement and the magnetic behavior observed in the ESR measurement.

II.3.4.4 Spin ordering in CO State

The charge and spin ordering in CO state for $0.3 < x < 0.75$ is basically represented by their AF CE-type [3] structure of $x = 0.5$, where Mn^{3+} and Mn^{4+} ions are arranged alternatively within the (001) plane and magnetic lattice is expanded to 4**a** x 4**b** x 2**c** in the pseudocubic setting. This fact indicates that they need the same additional mechanism which stabilizes the CE-type spin structure even at $x = 0.3$ despite a considerable spin disorder in the AF insulator. When x reduces from 0.5 to 0.3, the spin arrangement within the ab plane preserves CE-type feature but that along the c direction changes from antiparallel to parallel. Such an x-dependent AF structure has been discussed in terms of the double exchange interaction along the c-axis direction mediated by the extra electrons[5], the concentration of which is (1/2-x)/Mn site and measures the degree of the discommensuration. The deviation of x from 0.5 plays an important role for a melting of the CO state at the low temperature side. The CO state suppresses the ferromagnetic metal and favors an AF ordering.[5] Another consequence of discommensuration is the CAF state for $0.3 < x < 0.5$ at lower temperature than the AF state. The AF components are parallel to the [001] axis and the

ferromagnetic components lies in the (001) plane. T_{CA} decreases with x approaching 0.5 and as a result the spontaneous magnetization in the CAF state. The CAF state seems to be related with the invasion of the metallic phase toward low fields in the low temperature region $0.3 < x < 0.4$.[5]

II.3.4.5 Size of magnetic moment on Mn ion site

The ferromagnetic moment was determined to be $\mu_F \sim 1.9 \pm 0.2\ \mu_B$ / Mn at 5 K from the integrated intensity of the neutron diffraction profiles.[3, 5] Yoshizawa et al. has also determined the AF moment to be $\mu_{AFI} \sim 1.4 \pm 0.2\ \mu_B$ / Mn for Mn^{3+} ion site and $\mu_{AFI} < 0.5\ \mu_B$ / Mn for Mn^{4+} ion site, respectively.[5] The total moment $\mu_F \sim 2.36\ \mu_B$ /Mn ion site is rather small from 3.7 μ_B / Mn ion site calculated from the molar fraction of Mn^{3+} and Mn^{4+} ions in chemical composition $Pr_{0.65}Ca_{0.35}MnO_3$. In our present study, the magnetic moment was calculated to be $\mu_F \sim 0.83\ \mu_B$ / Mn as AF moment from the effective spin susceptibility $\chi_{eff.}$ in Figure II - 9 and $\mu_F \sim 0.35\ \mu_B$ / Mn as mostly ferromagnetic moment from d.c. magnetization in Figure II - 11. Both of estimations have been done at 100 K under magnetic field 0.01 T. Total moment is around 1.18 μ_B / Mn which is about a half of that obtained by Yoshizawa et al.[5] Relatively smaller values submit to further precise experimental and theoretical re-examination of magnetic state in high quality samples.

II.3.5 Unusual ESR profile behavior at low temperature

II.3.5.1 Unusual ESR profile behavior at low temperature

Figure II - 12 exhibits the ESR profiles at the low temperature region between 105 K and 75 K. The solid lines show the observed ESR profiles. The sharp resonance peaks around 320 mT come from the reference material Mn^{2+}/MgO as a marker. Fitting to a Lorentzian curve was made and the resultant curves are drawn with dotted lines. Below 90 K, there are remarkable changes in the observed ESR profiles. The ESR curves deviate from the Lorentzian shape together with the decomposition of the unique resonance curves and the resonance field seems to shift to the lower magnetic field. There are at least two absorption lines in the ESR profiles and they superpose with each other. This result shows the existence of disorder in the ferromagnetic (F) component of the CAF spin order below 80 K. It is also responsible for the probable spin-glass state which occurs below 80 K as shown in Figure II - 13.

II.3.5.2 Behaver of d.c. magnetization at low temperature

Figure II - 13 shows the d.c. magnetization under the magnetic field 0.01 T in the warming run after field cooling run (FC(W)), the cooling run after field cooling run (FC(C)) and the warming run after zero field cooling (ZFC), respectively. A spontaneous magnetization appears below T_{CAF} ~ 115 K. The irreversible hysteresis between the FC(W) and ZFC grows remarkably T_{CAF} ~125 K with a decrease in temperature, especially below 115 K.

II.3.5.3 Spin-glass state

The present observation is a typical magnetic behavior in case of the existence of spin-glass state as prescribed above. [13] The magnetic diffuse scattering is observed around the fundamental magnetic Bragg reflection of the parent spin structure in the neutron diffraction study which may indicate that the spin glass type disorder exists in the system. This diffuse scattering decreases drastically by applying a relatively weak field of ~ 2.0 T, and the component parallel to the field increases rapidly. Such behavior also supports that the diffuse scattering should be attributed to the spin-glass component which is sensitive to a weak external magnetic field. [5] In $Pr_{0.65}Ca_{0.35}MnO_3$, the concentration, x of Mn^{3+} ions does not retain a commensurate such as x = 1/4, 1/3 and 1/2. The observed magnetic structure in the orthorhombic ab plane is that of the commensurate value x = 1/2 structure as reported in an early study. [3] Thus, the formation of charge-ordering (CO) after CE-type configuration makes excess Mn^{3+} ions intersperse randomly over Mn^{4+} ion sites. Then the onset of some kind of frustrated exchange interaction leads to the spin glass like behavior at low temperature as detected by the present ESR profiles.

References

1. O. Yanagisawa, M. Izumi, W.-Z. Hu, K. Nakanishi, and H. Nojima : J. of Superconductivity, **12**, 307 (1999).
2. E. Pollert, S. Krupicka and E. Kuzmicova, J. Phys. Chem. Solids **43**, 1137 (1982).
3. Z. Jirak, S. Krupicka, Z. Simsa and M. Dlouha and S. Vratislav, J. Mag. Mag. Mat . **53**, 166 (1985).
4. F. Izumi, "The Rietveld Method", ed. by R.A. Young (1993) Oxford University Press, Oxford, Chap. 13.
5. H. Yoshizawa, H. Kawano, Y. Tomioka and Y. Tokura, Phys. Rev., B **52**, 13145 (1995).
6. S. B. Oseroff, M. Torikachvili, J. Singley, S. Ali, S.-W. Cheong and S. Schultz : Phys. Rev. B, **53**, 6521 (1996).
7. A. Shengelaya, Guo-meng Zhao, H. Keller, and K. A. Müller : Phys. Rev. Lett., **77**, 5296 (1996).
8. K. A. Müller : Phys. Rev. Lett. **2**, 341 (1959).
9. A. Abragam and B. Bleaney : *Electron Paramagnetic Resonance of Transition Ions* (Clarendon Press, Oxford, 1970).
10. S. E. Barnes : Adv. Phys. **30**, 801 (1981).
11. J. E. Gulley and V. Jaccarino : Phys. Rev. B, **6**, 58 (1972).
12. B. I. Kochelaev, L. Kan, B. Elschner and S. Elscner : Phys. Rev. B, **49** 13106 (1994).
13. Y. Tomioka, A. Asamitsu, H. Kuwahara, and Y. Moritomo, Phys. Rev., B **53**, 1689 (1996).

Chapter III

Photo-Induced Spin Susceptibility on the Charge-Ordered State in $Pr_{0.65}Ca_{0.35}MnO_3$ Powder

III.1 Introduction

In this section, we discuss the photo-induced effect on the effective spin susceptibility ($\chi_{eff.}$) and the absorption profile observed in the ESR under the photon injection with photon energy, hυ = 1.17 eV and 1.96 eV by laser in powder sample of $Pr_{0.65}Ca_{0.35}MnO_3$. [1, 2] The results under the photon injection at various temperatures exclude the laser heating as the origin of the above effect. The observed photo-induced effect appears remarkably around 80 K - 90 K, which is the characteristic temperature range below T_{CAF} ~ 115 K only with the photon injection with hυ = 1.17 eV. [3, 4, 5]

III.2 ESR Measurement under the Photon Injection.

For the photon injection, a Nd-YAG cw laser and a He-Ne cw laser were employed. The photon energy of Nd-YAG laser is near infrared region (photon energy, hυ = 1.17 eV and wavelength, λ = 10640 Å). On the other hand, He-Ne laser is visible region (hυ = 1.96 eV and λ = 6330 Å). The laser power were adjusted with an optical slit. They were 5 mW, 50 mW and 175 mW ($9x10^{17}$ photons / sec.), for the Nd YAG laser and 5 mW ($1.6x10^{16}$ photons/sec.), for the He-Ne laser.

The laser light was introduced into the sample situated in a cavity resonator through a double shielded quartz tubes letting the mixed gas and liq. He flow for low temperature measurements. The penetration depth of the laser light is estimated to be about 0.2 μm for the present sample.[6] The ESR measurement was done under the sequence, in which ESR profiles were measured without the photon injection, then with the photon injection by the He-Ne laser, subsequently by the Nd-YAG laser and finally without the photon injection again to check if any kind of damage to the sample occur.

III.3 Photo-Induced Spin Susceptibility on the CO State

III.3.1 ESR profiles without the photon injection

In Figure III - 1 (a) thin solid curves show the ESR profiles for the $Pr_{0.65}Ca_{0.35}MnO_3$ without the photon injection (dark) down to 80 K. It is the paramagnetic at room temperature (PI), then turns into the COI at $T_{CO} \sim 215$ K, successively into the AFI at $T_{AF} \sim 180$ K, and eventually into the canted antiferromagnetic state (CAFI) $T_{CAF} \sim 115$ K with a good agreement with the phase diagram of $Pr_{1-x}Ca_xMnO_3$.[3, 5] With the above successive phase transitions, the ESR profiles retain Lorentzian curvature down to around 100 K, which is below T_{CAF}. Below 100 K, the ESR profiles become broadened as shown in Figure III - 1 (b) with some kind of dissociation of total magnetic moments, which is in accordance with the behavior of d.c. magnetization in the warming run after zero-field cooling [7]. The exact mechanism of disappearance of the ESR signal is not clear. Further investigation is necessary to clarify in this point. The d.c. magnetization exhibits a spin-glass behavior, which has also been signaled from the magnetic neutron scattering study. [4]

III.3.2 ESR profiles under the photon injection with $h\upsilon = 1.17$ eV

In both Figure III - 1 (a) and 1(b), the thick solid curves show the representative ESR profiles measured under the photon injection with $h\upsilon = 1.17$ eV at representative temperatures. It is clear that the ESR intensity initiate to depend on the photon injection below $T_{CO} \sim 215$ K with decreasing temperature. Remarkably, the effect of photon injection on the ESR profile becomes predominant below 100 K which is close to the expected onset temperature of the spin glass state below $T_{CAF} \sim 115$ K. [3, 7]

One might suspect that this transition is simply driven by the laser heating. The evidence against the laser heating is provided by the temperature dependence of ESR profiles. The ESR profiles with the photon injection show different behavior which is expected from temperature dependence of ESR profiles without the photon injection shown in Figure II - 11 when temperature increase was happened. Also there is no difference among those ESR profiles at lowest temperature where ESR profile is expected to be sensitive for this kind of heating. This transition was reproducible, not permanent and also not due to any damage to the sample by the laser irradiation. In fact, the ESR profile after the post-measurement with the photon injection shows almost identical with that obtained prior to the measurement under the photon injection.

In the temperature range of 100 - 80 K, the obtained photo-induced effect indicates that the $\chi_{eff.}$ increases due to the photon injection. In contrast, the ESR profiles at 50 K exhibits that the $\chi_{eff.}$ decreases under the photon injection with good reproducibility. It is remarked that no

significant difference was observed at 70 K, 60 K and below 30 K. Simple interpretation of the above effect is due to the increase of the spin susceptibility together with the dissociation of AF state based on CO state to F state. The present interpretation indicates that the photo-induced I-M transition, equivalently collapse of CO state, occurs under the excitation by laser light with optimal energy.

The photo-induced effect is remarkable at the temperature range of 100 K - 80 K which is in the CAF state. We speculate that the CAF state, in which spin moment and orbital angular moment as well appear from magnetic interaction, may play an important role in this photo-induced effect. The correlation between the injected photon and the orbital angular momentum leads to the photo-induced effect.[8]

Also the existence of the spin glass state [7] makes easy to lead the onset of I-M (AF-F) transition due to the short-range ordered CAF state. Such transition induces the enhancement of metallicity associated with the double-exchange interaction. It proves the photo-induced increase of the $\chi_{eff.}$ as shown in Figure III - 1 (80 K), which confirms the increase of the number of ferromagnetic spin. The spin glass state postulated by Yoshizawa et al.[1] may play an important role to realize photo-induced effect around 80 K. The composition of $Pr_{0.65}Ca_{0.35}MnO_3$ is not responsible for commensurate CO as in $Pr_{0.5}Ca_{0.5}MnO_3$. In case of $Pr_{0.5}Ca_{0.5}MnO_3$, the commensurate CO order with regular charge alternation is long range as $-Mn^{3+}-Mn^{4+}-Mn^{3+}-$. For $Pr_{0.65}Ca_{0.35}MnO_3$, as far as we consider trivalent (high spin) and tetravalent ionic (low spin) states, some kind of discommensuration should appear. In this case, the commensurability conducts to random distribution of AF and F exchange interactions, which eventually forms the spin glass state. Such state can be reorganized by laser excitation with optimal photon energy.

At 50 K, it is notable that the incident photons eventually decreases the $\chi_{eff.}$ with enough reproducibility. The above results are reversible for repetition of the measurements with and without the photon injection.

III.3.3 Photon energy dependence of photo-induced spin susceptibility

Figure III - 2 (a) and (b) show the ESR profiles without photon injection (dark) and with photon injection with $h\upsilon$ = 1.96 eV. In contrast to the photon injection with $h\upsilon$ = 1.17 eV, the ESR resonance intensity is not affected much under the photon injection with $h\upsilon$ = 1.96 eV.

Figure III - 3 shows the detailed ESR profiles for $Pr_{0.65}Ca_{0.35}MnO_3$ at 80 K, 50 K and 40 K under the photon injection with $h\upsilon$ = 1.17 eV and 1.96 eV, where obvious change in ESR profiles is given at temperature range in the CAF state. Large enhancement of the ESR intensity

occurs around 80 K.

Photon energy, hυ = 1.2 eV is characteristic in the optical spectra in $R_{1-x}A_xMnO_3$.[9, 10] It has been assigned as a charge-transfer excitation energy of an electron from the lower Jahn-Teller split e_g of Mn^{3+} to the e_g of adjacent Mn^{4+} ion, which exhibits the promotion of the dipole active photoionization of the small polaron. Our present result suggests that the simple near-infrared laser irradiation with the characteristic photon energy, hυ ~ 1.2 eV enhances some kind of vibronic state and eventually releases the cooperative Jahn-Teller distortion associated with CO state.

III.3.4 Laser power dependence of the photo-induced spin susceptibility

Figure III - 4 exhibits the incident laser power dependence of the ESR profiles for $Pr_{0.65}Ca_{0.35}MnO_3$ under the photon injection with hυ = 1.17 eV at 80 K and 50 K. These ESR profiles show different laser power dependence at 80K and 50 K. At 80 K, there are obvious change in ESR profiles and the $\chi_{eff.}$ increases with increasing laser power. It is noted that the described value of the laser power does not mean the exact value injected to the sample due to the double shielded He flow guide made from quartz glass as mentioned above. At 50 K there is a few change as a function of incident laser power in ESR profiles.

References

1. O. Yanagisawa, M. Izumi, W.-Z. Hu, K. Nakanishi, and H. Nojima : J. of Superconductivity, **12**, 311 (1999).
2. O. Yanagisawa, M. Izumi, W.-Z. Hu, K.-H. Huang, K. Nakanishi, and H. Nojima : NATO Science Series, 3. High Technology, **72**, 263 (1999).
3. Z. Jirak, S. Krupicka, Z. Simsa and M. Dlouha and S. Vratislav, J. Mag. Mag. Mat. **53**, 166 (1985).
4. H. Yoshizawa, H. Kawano, Y. Tomioka and Y. Tokura, Phys. Rev., B **52**, 13145 (1995).
5. Y. Tomioka, A. Asamitsu, H. Kuwahara, and Y. Moritomo, Phys. Rev., B **53**, 1689 (1996).
6. K. Miyano, T. Tanaka, Y. Tomioka and Y.Tokura : Phys. Rev. Lett., **78**, 4257 (1997).
7. O. Yanagisawa, M. Izumi, W.-Z. Hu, K. Nakanishi, and H. Nojima : J. of Superconductivity, **12**, 307 (1999).
8. I. Solovyev : To be published to Phys. Rev. B.
9. S. Kaplan, M. Quijada, H.D. Drew, D.B. Tanner, G.C. Xiong, R. Ramesh, C. Kwon, T. Venkatesan : Phys. Rev. Lett., **77**, 2081 (1996).
10. Y. G. Zhao, J.J.Li, R. Shreekala, H.D.Drew, C.L.Chen, W.L.Cao, C.H.Lee : Phys. Rev. Lett., **81**, 1310 (1998).

Chapter IV
Evidence of Photo-Induced Melting of the Charge-Ordered State in $Pr_{0.65}Ca_{0.35}MnO_3$ Powder by X-ray Diffraction

IV.1 Introduction

To investigate the origin of photo-induced effect observed in the ESR under the photon injection discussed in Chapter III [1], we study behavior of the superlattice reflections arisen from the CO structure by powder x-ray diffraction in this section.[2, 3] Intensity of the superlattice reflections was reduced under the photon injection with hυ = 1.17 eV. The origin of the present photo-induced effect is attributed to the formation of short-range FM states due to the breaking of AF ordering, which is triggered by the collapse of the CO states induced by the photon injection.

IV.2 Powder X-ray Diffraction Measurement under the Photon Injection

For the photon injection, a Nd-YAG cw laser with hυ = 1.17 eV was employed. Due to the difficulty to equalize the incident photon number for each, we did not apply other photon energy for comparison such as photon energy dependence of x-ray diffraction profile. The maximum laser power was monitored to be 175 mW ($9x10^{17}$ photons / sec.). The laser light was introduced into the sample situated in the He cryostat through a window shielded with the Kapton film. It is noted that the described value of the monitored laser power does not indicate the precise value injected into the samples due to the existence of the window shielded with the Kapton film as mentioned above. The powder x-ray diffraction was carried out under the sequence in which we measure the powder x-ray diffraction profile without the photon injection (dark), subsequently with the photon injection and finally without the photon injection.

IV.3 Photo-Induced Melting of Superlattice Reflections from the CO State

IV.3.1 Superlattice reflections in x-ray diffraction in the CO state

Figure II - 5 shows the powder x-ray diffraction profiles at 296 K, 190 K, 100 K and 50 K. The integrated intensities of the peaks assigned as the Bragg reflections are almost the same between those above and below T_{CO}. The superlattice reflection peaks appear below $T_{CO} \sim 215$ K. According to the indices as shown in Figure II - 5, the newly appearing peaks are assigned.

successfully as superlattice reflections with the unit cell parameters at 296 K as space group Pbnm. Hence, a superlattice structure, **a** x 2**b** x **c** relative to the unit cell at 296 K has been confirmed below 200 K, which provides a complementary evidence for the existence of the CO state associated with the charge alternation of Mn^{3+} and Mn^{4+} ions [4, 5].

Figure IV - 1 shows the temperature dependence of the integrated intensity of superlattice reflection at (3, 0.5, 2), which is one of the reflection which prominent increase below T_{CO}. These superlattice reflection peaks appear around T_{CO} associated with onset of the CO state and grows rapidly [6]. It is noted that the reflection intensity tends to be independent of temperature below $T_{AF} \sim 180$ K. The present result confirms that the CO state is firmly retained in the ground state which provides the AFI. The observed superlattice reflection intensity does not change under the x-ray diffraction measurement without the photon injection as far as we concern: i.e., no trace of photo-induced effect was observed in the CO state by using the present laboratory x-ray source in contrast to the previous synchrotron orbit radiation x-ray study [6, 7].

IV.3.2 Powder x-ray diffraction under the photon injection

The photo-induced effect for these superlattice reflections was studied under the photon injection with $h\upsilon = 1.17$ eV. Figure IV - 2 (a) and (b) show the powder x-ray diffraction profiles of superlattice reflections from (2 1.5 0) and (2 0.5 2) together with Bragg reflection from (1 1 3). These reflections were selected for clarity to compare the Bragg reflection intensities with superlattice reflection ones. As shown in Figure IV - 2, in contrast to the Bragg reflections, a prominent suppression of the superlattice reflection intensities was found out under the photon injection.

One might suspect that this transition is simply driven by the laser heating. The evidence against it is given as follows. In any case, if the incident laser light works on the increase of temperature one should observe the change of the lattice spacing. There is no remarkable difference in both intensity and shift of the Bragg reflection angle (shift less than 0.04 % of the length of lattice spacing as estimated from the Bragg reflection angles with and without the photon injection) for (1 1 3) reflection. The length of the lattice spacing should be quite sensitive for this kind of heating.

The observed intensity change of superlattice reflections was reproducible for alternation of switch-on and off of laser, not permanent and no remarkable trace of the damage to the sample was found to diffraction profiles. It is stressed that the almost identical Bragg profile without the photon injection was obtained to the powder x-ray diffraction measurement under the

photon injection. The remaining intensity of the superlattice reflections under the photon injection is possibly from the non-irradiated fraction of the powder particles with a mesh 20 μm and gradually melting CO domains [6], while the penetration depth of the laser light has been estimated to be about 0.2 μm [8] for the present sample.

IV.4 Mechanism of the Photo-Induced Effect

IV.4.1 Jahn-Teller small polaron

The observed suppression of the superlattice reflection evidently indicates that near-infrared photon injection with hυ ~ 1.2 eV induces the collapse of CO state which would be together with the transition from AF-CO to F-CD. In fact, Yoshizawa et al [5] showed the suppression of the superlattice intensity at (2, 1.5, 0) under magnetic field as an evidence of the collapse of the CO state. However, it is the first to our knowledge that laser light irradiation suppresses the superlattice intensity at (2, 1.5,0) structuraly. The present observation is not far from the previously observed I-M transition triggered by photocarrier generation by Miyano et al [8]. Without a structural evidence, they reported the trace of the collapse of the CO state by observation of photocurrent under the coexistence of the applied electric field and pulse laser irradiation with 1.2 eV in the photon energy range 0.6 to 3.5 eV.

We discuss the reason why we detect the collapse of CO state for photon energy ~ 1.2 eV. This energy value is characteristic in the optical spectra in these manganites. For example, there is a broad peak in the photoconductivity function centered around 1.2 eV in similar compound, $La_{0.7}Ca_{0.3}MnO_3$ [9] and $Nd_{0.7}Ca_{0.3}MnO_3$ [10]. It is assigned as a charge-transfer excitation of an electron from the lower Jahn-Teller split e_g of Mn^{3+} to the e_g of adjacent Mn^{4+} ion, which exhibits the promotion of the dipole active photoionization of the Jahn-Teller small polaron [9].

Our present result suggests that the photon injection with the characteristic photon energy ~ 1.2 eV which is near-infrared region enhances the vibronic state and eventually releases the cooperative Jahn-Teller distortion associated with CO state. Figure IV - 3 shows schematically the electronic structure of the Mn^{3+} and Mn^{4+} ions in $Pr_{0.65}Ca_{0.35}MnO_3$ and possible optical charge transitions. It shows the energy of Mn $3d$-e_g and $3d$-t_{2g} levels for adjacent Mn^{3+} and Mn^{4+} ions in the AF state associated with the CO state. The spin up e_g levels in the Mn^{3+} ions are split by E_{JT} due to the Jahn-Teller effect. In the Mn^{4+} the spin up e_g states are shifted upwards (relative to the unsplit Mn^{3+} ion spin up e_g levels) by E_B due to the oxygen breathing mode distortions. The spin down e_g level (not shown in the figure) of Mn^{4+} is higher by Hund's coupling energy $E_J = J_H S_C$

relative to the spin up e_g level of Mn^{4+}, where J_H is the exchange constant of Hund's coupling, S_C is the Mn ion core spin ($S_C = 3/2$). We estimate that the charge transition energy from the spin up e_g levels in the Mn^{3+} to the spin up e_g level of Mn^{4+} is about 1.2 eV.

This process leads in promoting the hopping of an electron from a Mn^{3+} to a neighboring Mn^{4+} with the transfer energy, t and mixing species of Mn^{3+} and Mn^{4+} ion site. It corresponds to the transition from the CO state to the CD state with the metallic property. In other word, it is the photoionization of the Jahn-Teller small polaron.

The large J_H means that the hopping of an outer-shell electron between two Mn sites is affected by the relative alignment of the core spins, being maximal when the core spins are parallel and minimal when they are antiparallel. This results in the double-exchange interaction between the localized spins, the core t_{2g} orbital (S=3/2) mediated by the hopping e_g orbital electron. The insulating sate is AF and the metallic state is ferromagnetic (F). We stress that laser induced conductance change in $La_{0.7}Ca_{0.3}MnO_3$ [9] has been observed near the PI to FM transition temperature. Highly polarized state of Mn^{3+} and Mn^{4+} spins as a ferromagnetic order is necessary to achieve the d.c. conductivity based on the collapsed CO state.

The present result of x-ray diffraction provides not only a structural evidence of collapse of the CO state by photon injection but also the photo-induced I-M transition occurs together with the increase of the spin canting toward the spin polarization of Mn sites. The present results also reconfirm inadequacy of simple double-exchange model and the importance of the influence of the lattice distortion as well as the AF ordering.

IV.4.2 Discommensuration effect

We state that the present observation of the collapse of the CO state with relative ease is strongly related to the discommensuration for the charge and spin ordering in CO state for $0.3 \leq x \leq 0.75$, which is basically represented by their AF CE-type [4]. In the composition with $x = 0.5$, where Mn^{3+} and Mn^{4+} ions are arranged alternately within the (001) plane and magnetic lattice is expanded to 4**a** x 4**b** x 2**c** in the pseudocubic setting. This fact indicates that they need some additional mechanism which stabilizes the CE-type spin structure even at $x = 0.35$ despite a considerable spin disorder in the AF insulator. When x reduces from 0.5 to 0.3, the spin arrangement within the ab plane preserves CE-type feature but that along the c direction changes from antiparallel to parallel configuration. Such an x-dependent AF structure has been discussed in terms of the double-exchange interaction along the c-axis direction mediated by the extra electrons [5], the concentration of which is (1/2-x)/Mn site and measures the degree of the

discommensuration. The deviation of x from 0.5 plays an important role for a melting of the CO state with relative ease at the low temperature side. The CO state suppresses the FM and favors an AF ordering [5, 11], eventually leading to the CAF state below T_{CAF} = 125 K lower than T_{AF}. The AF components are parallel to the [001] axis and the ferromagnetic components lies in the (001) plane. In the present results, the CAF state seems to be related with the appearance of the metallic phase based on the collapse of the CO state with the photon injection with $h\upsilon$ = 1.17 eV.

References

1. O. Yanagisawa, M. Izumi, W.-Z. Hu, K. Nakanishi, and H. Nojima : J. of Superconductivity, **12**, 311 (1999).
2. O. Yanagisawa, M. Izumi, W.-Z. Hu, K.-H. Huang, K. Nakanishi, and H. Nojima Physica B, **271**, 235 (1999).
3. O. Yanagisawa, M. Izumi, W.-Z. Hu, K.-H. Huang, K. Nakanishi, and H. nojima : NATO Science Series, 3. High Technology, **72**, 263 (1999).
4. Z. Jirak, S. Krupicka, Z. Simsa and M. Dlouha and S. Vratislav : J. Mag. Mag. Mat. **53**, 166 (1985).
5. H. Yoshizawa, H. Kawano, Y. Tomioka and Y. Tokura, Phys. Rev., B **52**, 13145 (1995).
6. D. E. Cox, P. G. Radaelli, M. Marezio, S-W. Cheong : Phys. Rev. B, **57**, 3305 (1998).
7. V. Kiryukhin, D. Casa, J. P. Hill, B. Keimer, A. Vigilante, Y. Tomioka, and Y. Tokura Nature, **386**, 813 (1997).
8. K. Miyano, T. Tanaka, Y. Tomioka and Y.Tokura : Phys. Rev. Lett., **78**, 4257 (1997).
9. Y. G. Zhao, J.J.Li, R. Shreekala, H.D.Drew, C.L.Chen, W.L.Cao, C.H.Lee : Phys. Rev. Lett., **81**, 1310 (1998).
10. S. Kaplan, M. Quijada, H.D. Drew, D.B. Tanner, G.C. Xiong, R. Ramesh, C. Kwon, T. Venkatesan : Phys. Rev. Lett., **77**, 2081 (1996).
11. Y. Tomioka, A. Asamitsu, H. Kuwahara, and Y. Moritomo, Phys. Rev., B **53**, 1689. (1996).

Chapter V

Comparative Study of Photo-Induced Effect in $Pr_{0.65}Ca_{0.35}MnO_3$ in Powder and Thin Films

V.1 $Pr_{0.65}Ca_{0.35}MnO_3$ Thin Films

In Chapter III and IV, the photo-induced effect observed with the ESR and the x-ray diffraction in the powder sample of $Pr_{0.65}Ca_{0.35}MnO_3$ under the near-infrared laser irradiation (photon energy, hυ = 1.17 eV) has been thoroughly discussed. This photo-induced effect is perhaps due to the photo-induced collapse of the CO and is associated with the AFI - FM transition similar to the CMR effect. This photo-induced effect has a grate potentiality in the industrial application for the optical-magnetic hybrid device, with which one can control the electric property by the photo injection and/or the magnetic field. In fact, the CMR effect [1, 2, 3] in the manganese have already been applied for the super high density magnetic recording system, e.g., a magnetic pick up sensor for hard disk drive (HDD). The bolometer effect, which is the sharp AFI - FM transition by thermal heating with light has as well been applied for the night scope. [4, 5, 6] However, in the $R_{1-x}A_xMnO_3$, it is noted that the threshold energy for this photo-induced effect (order of 10 mW) is the smallest in the AFI - MF transition. This fact in turn rises up the potentiality of photo-induced effect in industrial application.

On the other hand, the fabrication of the thin film also provides a good advantage for application. The first reason is its ability to enhance the sensitivity of the photo-induced effect found in the powder sample against the small penetration depth of the laser light, and the second is its ability to process the large integrated circuit (LSI) with the usual micro-processing technology for the semiconductor LSI. However, the phenomenon of oxygen semiconductor in the thin films varies in the preparatory condition and influences the charge carrier concentration as well as electrical properties like most of the metal oxides. A strain effect due to the lattice mismatch between the film and the substrate plays an important role resulting in a distortion of perovskite structure of manganite and eventually in the population of Mn^{3+} and Mn^{4+} ions.

In this chapter, a property of the $Pr_{0.65}Ca_{0.35}MnO_3$ thin-film samples prepared by the sol-gel method has been compared to the $Pr_{0.65}Ca_{0.35}MnO_3$ powder sample focussing on the photo-induced effect. It is shown that there is a large difference between the powder and the thin films with respect to the existence of the CO state. [7]

V.2 Experiment

V.2.1 Sample preparation of $Pr_{0.65}Ca_{0.35}MnO_3$ thin film

The thin film samples of $Pr_{0.65}Ca_{0.35}MnO_3$ with 5000 Å thickness were prepared by the sol-gel method on $SrTiO_3$ (100) single crystal substrates. First, a repetition of the spin-coating was done starting with a xylene-MOD solution and following by a dry and pyrolysis process at 430 °C, 10 min. Second, the crystallization was done by RTA (Rapid Thermal Annealing) under N_2O gas flow. The optimal crystallization was obtained at 900 °C.[7]

The x-ray diffraction was carried out at room temperature to study the crystallographic characters of the thin film samples. The temperature dependence of d.c. resistance was measured by a conventional four-probe method from 290 K to 5 K under an applied magnetic field up to 6 T using a superconducting magnet (Oxford Maglab 2000).

V.2.2 ESR measurement

The EPR study for the spin states of $3d$-t_{2g} (S=2) and/or $3d$-e_g (S=3/2) on Mn^{3+} and Mn^{4+} ionic sites was done using a spectrometer operated at 9.0 GHz (X-band) from 300 K down to 10 K. For the thin-film sample, the static magnetic field H_0 was applied perpendicular to the c-axis of the film.

To investigate the photo-induced effect, a He-Ne CW laser of photon energy, $h\upsilon$ = 1.96 eV and a Nd-YAG CW laser of $h\upsilon$ = 1.17 eV were employed for the photon injection. The laser power was adjusted with an optical slit resulting in 5 mW, 50 mW and 175 mW ($9x10^{17}$ photons/sec.) for the Nd YAG laser, and 5 mW for the He-Ne laser.

V.3 Results and Discussion

V.3.1 X-ray diffraction analysis

Figure V - 1 shows the x-ray diffraction profile of $Pr_{0.65}Ca_{0.35}MnO_3$ thin film at 290K. The peak profile of the 002 peak is shown with the 002-diffraction peak of the $SrTiO_3$ substrate. The x-ray diffraction indicates the formation of high degree of crystalline order and orientation of the c-axis due to the annealing procedure under N_2O gas flow. The typical sample thickness is around 5000 Å.

V.3.2 Transport property

The electric transport property of the powder and the thin-film samples are significantly different.

Figure II - 6 shows the temperature dependence of the differential resistance (dR/dT) of $Pr_{0.65}Ca_{0.35}MnO_3$ powder sample. It is semiconductor-like without external magnetic field at whole temperature range. The dR/dT shows a prominent peak which is a sign of onset of the second-order phase transition associated with formation of the CO state where the charge is localized on Mn ionic site at $T_{CO} \sim 215$ K together with the Mn^{3+} and Mn^{4+} alternation leading to the superlattice x-ray reflection. The powder sample shows a CMR effect $(R_M-R_0)/R_0 \sim 400$ % with a threshold magnetic field of about 2 T at the CO state below T_{CO}.

Figure V - 2 shows the temperature dependence of the dR/dT of a $Pr_{0.65}Ca_{0.35}MnO_3$ thin film sample. The dR/dT does not show any clear sign of the onset of the second-order transition that gives an evidence for the existence of the CO state. The present thin-film samples do not show any significant CMR effect at high magnetic fields up to 6T at whole temperature range. It showed rather a positive magnetoresistance.

V.3.3 ESR for $Pr_{0.65}Ca_{0.35}MnO_3$ powder

In Figure III - 3, the dotted curves show the ESR profiles for the $Pr_{0.65}Ca_{0.35}MnO_3$ powder sample without the photon injection (dark). The ESR spectrum exhibits the paramagnetic behavior at room temperature. This paramagnetic feature is retained down to the CO state below $T_{CO} \sim 215$ K. Below the onset of the AF state at $T_{AF} \sim 180$ K, the ESR signal becomes weak with decreasing temperature. Eventually the characteristic feature of the ensemble of spin clusters appears around the onset of the CAF state of $T_{CAF} \sim 115$ K. This is in good agreement with the

phase diagram of $Pr_{1-x}Ca_xMnO_3$. [8, 9, 10] It is stressed that below T_{CAF}, the ESR profiles become broadened with some kind of dissociation of the total magnetic moments, which is in accordance with the behavior of d.c. magnetization in the warming run after zero-field cooling [8].

The resonance is more characteristic of ferromagnetic resonance from a collection of independent and randomly oriented anisotropic crystalline samples. Anti-ferromagnetic resonance is not probable since the individual exchange field of the separate magnetic sublattices would be too large to provide a resonance at 9.0 GHz.

In Figure III - 3, the thick solid curves show the ESR profiles under the photon injection with $h\upsilon$ = 1.17 eV. It is clear that the ESR intensity starts to depend on the photon injection below T_{CO} ~ 215 K with decreasing temperature and strikingly recovers its paramagnetic resonance intensity even below T_{CAF} (115 K). The present photo-induced effect becomes predominant below 100 K [11]. In the temperature range of 100 K - 80 K, the obtained photo-induced effect indicates that the effective spin susceptibility, $\chi_{eff.}$ revives due to the photon injection. These results indicate that the CO state with CAF spin order can be transformed to paramagnetic and/or ferromagnetic order. In the following, the x-ray diffraction profile measured under the photon injection clearly suppresses the super-lattice reflection, which provides us evidence for the melting of the CO sate. It is clear that the energy value of 1.17 e V of laser light is assigned as a charge-transfer excitation of an electron from the lower Jahn-Teller split e_g of Mn^{3+} to the e_g of adjacent Mn^{4+} ion. The present interpretation indicates that the photo-induced I-M transition or equivalently the collapse of the CO state, occurs under the excitation by laser light with optimal energy. In fact, in contrast to the photon injection with $h\upsilon$ = 1.17 eV, the ESR resonance intensity is not affected under the photon injection with $h\upsilon$ = 1.96 e V. The photon energy, $h\upsilon$ = 1.17 e V, is characteristic in the optical spectra in $R_{1-x}A_xMnO_3$. It has been assigned as an excitation energy of the small Jahn-Teller polaron. [12] Our present result suggests that the photon injection with $h\upsilon$ ~ 1.2 eV enhances some kind of vibronic state and eventually releases the cooperative Jahn-Teller distortion associated with the CO state.

V.3.4 ESR for $Pr_{0.65}Ca_{0.35}MnO_3$ thin films

In Figure V - 3, the thin solid curves show the ESR profiles for the $Pr_{0.65}Ca_{0.35}MnO_3$ thin film samples without the photon injection (dark) at temperature range 130 K – 95 K. The ESR was very weak and paramagnetic resonance above 130 K.

In the thin film, the ESR intensity with g ~ 2.0 gradually increases with decreasing temperature, suggesting the existence of paramagnetic susceptibility. Below 120 K, the spectrum splits into at least two lines and the center magnetic field of the resonance profile shifts to a low magnetic field with decreasing temperature. The observed resonance-shift indicates the appearance of the spontaneous magnetization. The temperature dependence of the resonance field-shift below 120 K is in good agreement with the phenomenological order parameter, which is induced from the second-order transition scheme. [13] The precise study to identify the origin of the observed resonance is under progress with respect to both paramagnetic resonance of ferromagnetic clusters and the propagation of magnetic polarons [14, 15].

Figure V - 3 shows temperature dependence of the ESR profiles for $Pr_{0.65}Ca_{0.35}MnO_3$ thin film under the photon injection with $h\upsilon$ = 1.17 eV by dotted lines. The ESR profiles in the present thin film exhibit a weak modification under the photon injection in temperature range 110 K - 95 K. We estimate that the present result is a kind of photo-induced effect. However, the mechanism of this effect does not come from the photo-induced melting of the CO state as in the powder sample. This is because there is no evidence for the existence of the CO state in this present thin film.

V.3.5 Origin of difference between thin film and powder

The electrical and magnetic properties of thin film and powder samples of $Pr_{0.65}Ca_{0.35}MnO_3$ are quite different as we mentioned above. The difference may be due to the oxygen stoichiometry , the degree of order of the population of Mn ions, the charge carrier concentration and eventually electron hopping like in most metal oxide materials. A strain effect due to the lattice mismatch between the film and the substrate is plausible and it may control the distortion of perovskite structure.

With the laser irradiation, we find the shift of the resonance line to high magnetic field. We think that the present photo-induced effect is not due to the same mechanism as in the powder sample since the thin-film form does not possess the CO state. Probably, the present transition in the thin films is a ferromagnetic transition with some kind of photo-induced effect, which is in contrast to the photo-induced effect in bulk compounds.

Reference

1. Y. Tomioka, A. Asamitsu, H. Kuwahara, and Y. Moritomo, Phys. Rev. B. **53**, 1689 (1996).
2. S. Jin, T. H. Tiefel, M. McCormack, R. A. Fastnacht, R. Ramesh, L. H. Chen, Science, **264**, 413 (1994).
3. H. Chiba, M. Kikich, K. Kusaba, Y. Muraoka and Y. Syono : Solid State Commun, **99** 499 (1996).
4. N. Mathur : Nature, **390**, 229 (1997).
5. M. Rajeswari, C. H. Chen, A. Goyal, C. Kwon, M. C. Robson, R. Ramch, T. Venkatesan and S. Lakeou : Appl. Phys. Lett., **68**, 3555 (1996).
6. A. Goyal, M. Rajeswari, R. Shreekala, S. E. Lofland, S. M. Bhagat, T. Boettcher, C. Kwon, R. Ramch, and T. Venkatesan : Appl. Phys. Lett., **71**, 2535 (1997).
7. O. Yanagisawa, M. Izumi, K.-H. Huang, W.-Z. Hu, Y. Shen, K. Nakanishi, Y. Takahashi and H. Nojima : Accepted to J. of Magnetism and Magnetic Material at Jun. 1, 1999.
8. O. Yanagisawa, M. Izumi, W.-Z. Hu, K. Nakanishi, and H. Nojima : J. of Superconductivity, **12**, 307 (1999).
9. Z. Jirak, S. Krupicka, Z. Simsa and M. Dlouha and S. Vratislav, J. Mag. Mag. Mat . **53**, 166 (1985).
10. Y. Tomioka, A. Asamitsu, H. Kuwahara, and Y. Moritomo, Phys. Rev., B **53**, 1689 (1996).
11. O. Yanagisawa, M. Izumi, W.-Z. Hu, K. Nakanishi, and H. Nojima : J. of Superconductivity, **12**, 311 (1999).
12. A. J. Millis, Boris I. Shraiman, and R. Mueller, Phys. Rev. Lett., **77**, 175 (1996).
13. R.A. Cowley : Advances in Phys., 29,1 (1980).
14. D. C. Worledge, L. Mieville, T. H. Geball : J. Appl. Phys., 83, 5913 (1998).
15. O. Chauvet, G. Goglio, P. Molinie, B. Corraze, L. Brohan : Phys. Rev. Lett., 81, 1102 (1998).

Chapter VI

Comparative Study of Photo-Induced Effect in Thin Films of $La_{0.67}Ca_{0.33}MnO_3$ and $Pr_{0.65}Ca_{0.35}MnO_3$

VI.1 $La_{0.67}Ca_{0.33}MnO_3$ Thin Film

In Chapter V, the $Pr_{0.7}Ca_{0.3}MnO_3$ (PCMO) thin film prepared by the sol-gel method has been studied focusing on the photo-induced effect observed in the PCMO powder sample. However, the photo-induced effect and the CO state which plays an important role for the I-M transition by the external stimulation such as the CMR effect are absent in the present PCMO thin film sample. Refer to the data updated, no success has recently been reported for the I-M transition such as the CMR effect in the PCMO thin film.

The $R_{1-x}A_xMnO_3$ with small ionic radii of the (A, R) ions, such as PCMO, has a delicate physical property which competes between the CD metallic state with ferromagnetic spin order plus small Jahn-Teller distortions, and the CO insulating state due to the small transfer integral. The physical property of the PCMO thin film is strongly affected by the thin film preparation factor such as the oxygen stoichiometry and the strain effect.

On the contrary, the $R_{1-x}A_xMnO_3$ with large ionic radii of the (A, R) ions, such as LCMO, is not affected by the thin film preparation factor. It is much easier to be prepared in thin film samples. The proper choice of La/Ca atomic radius ratio such as the $La_{0.67}Ca_{0.33}MnO_3$ (LCMO) results in the double exchange ferromagnetic ground state. The LCMO exhibits a metallic conduction below the I-M transition temperature (T_c) and the CMR around T_c.

In this chapter, the LCMO thin film samples prepared by the sol-gel method are studied competitively with the PCMO thin films to optimize the CO state and to achieve the photo-induced effect in the PCMO thin films with the X-band ESR and the resistivity measurement. [1]

VI.2 Sample Preparation of $La_{0.67}Ca_{0.33}MnO_3$ Thin Film

LCMO thin film samples were prepared by the sol-gel method on the $SrTiO_3$ (100) substrate as mentioned in Chapter V. The optimal crystallization was obtained at 1000 °C for LCMO thin films. [1]

With the x-ray diffraction technique, we can confirm that these samples have the high degree of crystallinity and proper orientation on the c-axis. Figure VI - 1 shows the x-ray diffraction profiles of LCMO and PCMO thin film samples. For the substrate, the 002 diffraction peak profile is shown with the 002 peak. In the case of LCMO thin films, the repetition of the post-crystallization annealing at 800 °C is remarkable with increase in T_C. This is directly connected to the I-M transition temperature obtained from the d.c. resistance measurements. The increase in T_c (the highest T_c = 310 K) is most probably caused by the increase in oxygen content. The LCMO and PCMO thin films were typically 5000 Å thick. [1]

VI.3 Results and Discussion

VI.3.1 Transport properties

Figure VI - 2 presents the d.c. resistivity as a function of temperature in $Pr_{0.65}Ca_{0.35}MnO_3$ (PCMO) and $La_{0.67}Ca_{0.33}MnO_3$ (LCMO) thin film samples. The PCMO thin films shows the semiconducting behavior with the activation energy of 48 meV without any sign of the formation of the CO state (see the temperature derivative resistance dR/dT curve). This is in contrast with the observation of the CO phase transition in the bulk PCMO sample at 215 K [2, 3]. Due to either a mismatch of the optimal lattice constant of PCMO with that of the applied substrate or some kind of lattice defects, the optimal population of Mn^{3+} and Mn^{4+} ions looks difficult to be achieved in the studied films. In the subsequent discussion, we will focus on the survey of the onset of some kind of magnetic transition in the PCMO thin film. For LCMO composition, the thin film shows the I-M transition at 260 K (T_c) together with a large CMR.

VI.3.2 Magnetic transition

VI.3.2.1 ESR profile

Figure VI - 3 shows the ESR profiles for PCMO and LCMO thin films. The static magnetic

field H_0 was applied parallel to the surface of the films ($H_0 \perp$ c-axis). In PCMO sample, the ESR signal intensity of g ~ 2.0 gradually increases with decreasing temperature, suggesting the existence of the paramagnetic susceptibility. Below T_c ~ 125 K, the resonance magnetic field of ESR profile shifts to a lower magnetic field with decreasing temperature. The observed resonance-shift signals the appearance of the spontaneous magnetization. The obtained results are in contrast with the observed ESR signals for the PCMO powder sample with the same nominal composition.

The thin film of LCMO shows the paramagnetic behavior down to 270 K and the spectrum splits into two lines around T_c ~ 260 K. One of them shifts to a lower resonance field with the broad line. The other resonance line remains with g ~ 2 band and gradually disappear.

VI.3.2.2 Temperature dependence of resonance shift

In Figure VI - 4, the resonance magnetic field in both PCMO and LCMO thin films have been plotted. These values were taken from the simple unconvoluted experimental ESR spectrum. The observed shift of the resonance magnetic field is noted as Δg (shift of the resonance g value from the g value at room temperature).

The temperature dependence of Δg below T_c indicates the critical behavior in the case of the existence of the second-order magnetic transition. According to the simple phenomenological Landau theory of the second-order phase transition [4], we have performed the theoretical fit to the obtained center magnetic field Δg as $\alpha(T_c\text{-}T)^{1/2}$ where α is the positive constant. As shown in Fig. 4, a good agreement between the obtained resonance shift and the calculated $(\Delta g)^2$ was achieved for both compounds below T_c. It has been reported that LCMO undergoes into the FM state below T_c ~ 260 K [5]. The present PCMO thin films similarly show the magnetic transition with ferromagnetic order at T_c ~ 120 K.

In summary, in the PCMO thin films, there is no onset of the CO state around 215 K in the d.c. resistivity behavior as seen in the PCMO powder sample [1]. The mismatch between the lattice constants of PCMO and those of substrate or some kind of lattice defects and strains, the insufficient population of Mn^{3+} and Mn^{4+} ions might prevent the realization of the identical properties as seen in the PCMO powder sample [6].

In contrast to the bulk PCMO, we have found the existence of the onset of the magnetic transition at 120 K in the PCMO thin films. The temperature dependence of the resonance field-shift below 120 K is consistent with the phenomenological order parameter induced from the

second-order transitional scheme. In order to identify the origin of the observed resonance, the more precise studies are presently in progress. We concern in both the paramagnetic resonance of ferromagnetic clusters and the propagation of magnetic polarons [7, 8]. Finally, we suggest the existence of probable spin-fold over the effect of the spin wave below 90 K for PCMO and 150 K for LCMO thin films, which is a characteristic behavior of ferromagnetic thin films.

References

1. O. Yanagisawa, M. Izumi, W.-Z. Hu, K. Nakanishi, and H. Nojima : J. of Superconductivity, **12**, 307 (1999).
2. H. Yoshizawa, H. Kawano, Y. Tomioka and Y. Tokura : Phys. Rev., B **52**, 13145 (1995).
3. D. E. Cox, P. G. Radaelli, M. Marezio, S-W. Cheong : Phys. Rev. B, **57**, 3305 (1998).
4. R.A. Cowley : Advances in Phys., **29**, 1 (1980).
5. Q. Huang, A. Santoro, J.W. Lynn, R.W. Erwin, J.A. Borchers, J.L. Peng, K. Ghosh, R.L. Greene : Phys. Rev. B, **58**, 2684 (1998).
7. K.A. Thomas, P.S.I.P.N. de Silva, L.F. Cohen, A. Hossain, M. Rajeswari, T. Venkatesan, R. Hiskes, J.L. MacManus-Driscoll : J. Appl. Phys., **84**, 3939 (1998).
7. D. C. Worledge, L. Mieville, T.H. Geballe : J. Appl. Phys., **83**, 5913 (1998).
8. O. Chauvet, G. Goglio, P. Molinie, B. Corraze, L. Brohan : Phys. Rev. Lett., **81**, 1102 (1998).

Chapter VII
Conclusion

With respect to the photo-induced effect, we investigated the spin system and the charge system in $Pr_{0.7}Ca_{0.3}MnO_3$ by ESR and x-ray diffraction, respectively. As the first step, magnetic and structural behavior of $Pr_{0.65}Ca_{0.35}MnO_3$ (Space group: *Pbnm* at 296 K) in powder form was studied. The onset of the charge-ordered (CO) state at $T_{CO} \sim 215$ K was verified from the change of lattice constants and the appearance of superlattice reflections. The antiferromagnetic transition was found out at $T_{AF} \sim 180$ K based on the ESR linewidth $\Delta H_{P\text{-}P}$. The canted antiferromagnetic transition was observed at $T_{CAF} \sim 125$ K from both the appearance of the spontaneous d.c. magnetization and an abrupt increase of the $\Delta H_{P\text{-}P}$. The resonance intensity in ESR profile becomes weakened with decreasing temperature, suggesting the existence of magnetic disorder below 90 K. It is responsible for behavior of d.c. magnetization below T_{CAF}. They provide an evidence of the existence of the spin-glass state.

To investigate a photo-induced effect, the ESR for $Pr_{0.65}Ca_{0.35}MnO_3$ powder was measured under the photon injection by a He-Ne cw laser with photon energy, $h\upsilon = 1.96$ eV and a Nd-YAG cw laser with $h\upsilon = 1.17$ eV. Both significant change of the ESR curve and increase of the effective spin susceptibility was clearly found out under the photon injection with $h\upsilon = 1.17$ eV between 90 K - 80 K, in the canted antiferromagnetic state associated with the CO structure. The temperature dependence of ESR profile excludes the possibility of laser heating. On the contrary, the ESR corve is not affected much under the photon injection with $h\upsilon = 1.96$ eV. Photon energy, $h\upsilon \sim 1.2$ eV is characteristic in the optical spectra in distorted perovskite manganese. It has been assigned as a charge-transfer excitation energy of an electron from the lower Jahn-Teller split e_g of Mn^{3+} to the e_g of adjacent Mn^{4+} ion, which exhibits the promotion of the dipole active photoionization of the small polaron. Our present result suggests that the photon injection with the characteristic photon energy, $h\upsilon \sim 1.2$ eV enhances vibronic state and eventually releases the cooperative Jahn-Teller distortion associated with CO state.

The behavior of CO state in $Pr_{0.65}Ca_{0.35}MnO_3$ powder under the photon injection with $h\upsilon = 1.17$ eV was studied with the x-ray diffraction to understand the mechanism of present photo-induced effect. Below T_{CO}, the superlattice reflections appeared associated with the formation of the CO state and the CO sate was maintained down to at least 10 K. The photon injection led to the prominent decrease of the intensity of superlattice reflections. The present result provides a

structural evidence of the collapse of CO state by the photon injection. The present result suggests that a photo-induced I-M transition occurs due to the propagation of delocalized carriers via probable double-exchange interaction in the collapsed CO state created by the photon injection.

As the second step, $Pr_{0.65}Ca_{0.35}MnO_3$ thin films were prepared to improve the sensitivity of the photo-induced effect against small penetration depth of the laser light and to get the advantages in industrial application. The thin films of $Pr_{0.65}Ca_{0.35}MnO_3$ with 5000 Å thickness were prepared by the sol-gel method on $SrTiO_3$ (100) substrates. In the ESR study, the thin films exhibit the ferromagnetic transition at $T_c \sim 120$ K and some kind of weak photo-induced effect at low temperature. However, the ground state of the discussed thin films are not accompanied by the CO state, which plays an essential role on the photo-induced effect. These differences are due to the oxygen stoichiometry and strain effect due to the lattice mismatch.

Thin film of distorted perovskite manganese with large size rare earth and alkaline earth ions, $La_{0.67}Ca_{0.33}MnO_3$ is less effected in the oxygen stoichiometry and/or the strain effect. To enhance the photo-induced effect in $Pr_{0.65}Ca_{0.35}MnO_3$ thin film against these process parameters, $La_{0.67}Ca_{0.33}MnO_3$ thin films were comparatively studied. $La_{0.67}Ca_{0.33}MnO_3$ undergoes the transition from the paramagnetic insulating state into the ferromagnetic metallic state at the Curie temperature, $T_c \sim 260$ K. The temperature dependence of the ESR resonance magnetic field in both $Pr_{0.65}Ca_{0.35}MnO_3$ and $La_{0.67}Ca_{0.33}MnO_3$ thin films obeys a critical behavior of a second-order phase transition, corresponding to the appearance of the spontaneous magnetic moment.

Increase of the effective spin susceptibility and collapse of CO state was found in $Pr_{0.65}Ca_{0.35}MnO_3$ powder under photon injection ($h\upsilon = 1.17$ eV). This photo-induced effect has the lowest threshold in I-M transitions found in $Pr_{1-x}Ca_xMnO_3$. However, $Pr_{0.65}Ca_{0.35}MnO_3$ thin films prepared by the sol-gel method does not show photo-induced effect and is not accompanied by the CO state.

Acknowledgments

The author would like to express the genuine appreciation to Professor Mitsuru Izumi (Tokyo University of Mercantile Marine, Japan) for discussions, suggestions and continuous encouragement.

The author would like to express his gratitude to Professor Kunimitsu Uchinokura (University of Tokyo, Japan) and Professor Yuuichi Ochiai (University of Chiba, Japan) as examining committee of doctoral thesis.

The author would like to express the special thank to Dr. Kenji Nakanishi, Dr. Hideo Nojima, Dr. Yoshihiro Takahashi (Functional Devices Research Laboratory, Sharp Co., Japan) and Dr. N. Tsuchimine (Toshima Mfgs Co. Ltd., Japan) for powder sample preparation, SQUID measurement and discussion.

The author would like to express the gratitude to Dr. D. B. Romero (NIST, U.S.A.) and Dr. A. Weber (NIST, U.S.A.) for thin film sample preparation and useful suggestions.

The author would like to thank Wei-Zhi Hu (Tokyo Univ. of Mercantile Marine, Japan) and Dr. Ayako Yamamoto (ISTEC, Japan) for the powder x-ray diffraction measurement and discussion.

Finally the author is pleased to acknowledge Dr. Hitoshi Ohnuki, Kai-hua Huang, Takahiro Nakayama, Yi Shen and all members of the research group under Professor Mitsuru Izumi in Laboratory of Applied Physics for useful discussion and continuous encouragement.

Figure Captions

Figure I - 1 Crystal structure of the distorted perovskite manganese, $R_{1-x}A_xMnO_3$ (R = trivalent rare earth element and A = divalent alkaline earth element).

Figure I - 2 Electronic configuration of ionic state of Mn^{3+} and Mn^{4+} ions in the distorted perovskite manganese according to the Hund's rule.

Figure I - 3 Double-exchange mechanism in the distorted perovskite manganese, $La_{1-x}Sr_xMnO_3$ with the larger ionic radii.

Figure I - 4 Phase diagram of $Pr_{1-x}Ca_xMnO_3$ determined by resistivity, magnetization and neutron diffraction by Y. Tomioka et al. J. Phys. Soc. Jpn., 65, 1043 (1996).

Figure I - 5 The schematic spin structure of the pseudo CE-type antiferromagnetic structure (a) for the collinear intermediate phase and (b) for the canted low temperature phase. Lines of the open circles (Site 1) and the closed circle (Site 2) may appear either along the x direction or along the y direction due to domain.

Figure I - 6 Mechanism of the electron spin resonance.

Figure I - 7 Effective fields in antiferromagnetic resonance. The magnetization $\mathbf{M}_1$ on sublattice 1 sees a field $\mathbf{B}_1$, $-\lambda\mathbf{M}_2 + B_A\mathbf{z}$; The magnetization $\mathbf{M}_2$ on sublattice 2 sees a field $\mathbf{B}_2$, $-\lambda\mathbf{M}_1 - B_A\mathbf{z}$. Both ends of the crystal axis are "easy axes" of magnetization.

Figure I - 8 The block diagram of the electron spin resonance spectrometer.

Figure I - 9 Definition of the electron spin resonance linewidth $\Delta H_{p\text{-}p'}$.

Figure I - 10 Scattering by a group of electrons at positions $\mathbf{r}_j$. The wave numbervectors $\boldsymbol{k}_0$ and $\boldsymbol{k}_1$ give the direction of the primary x-ray beam and the direction to the point of observation P.

Figure I - 11 The function $\sin^2 Nx / \sin^2 x$ for $N = 10$. The function peaks at values of x, which are integral multiples of π and it is essentially zero everywhere else.

Figure II - 1 Schematic view of optical component of the laboratory powder x-ray diffractometer.

Figure II - 2 Schematic view of the d.c. magnetic susceptibility measurement.

Figure II - 3 Powder x-ray diffraction profiles with + mark and the Rietveld fitting result with solid lines for $Pr_{0.65}Ca_{0.35}$ powder at 290 K.

Figure II - 4 Lattice constants for $Pr_{0.65}Ca_{0.35}MnO_3$ powder from the x-ray diffraction as a function of temperature from 300 K down to 10 K.

Figure II - 5 Superlattice reflections observed in the powder x-ray diffraction profiles for $Pr_{0.65}Ca_{0.35}MnO_3$ powder at representative temperature.

Figure II - 6 The temperature dependence of the differential resistance (dR/dT) of $Pr_{0.65}Ca_{0.35}MnO_3$ powder.

Figure II - 7 The magnetic field dependence of the resistance, R of $Pr_{0.65}Ca_{0.35}MnO_3$ powder at 80 K. The CMR effect $(R_M-R_0)/R_0$ is about 400 %. The threshold magnetic field is about 2 T.

Figure II - 8 Electron spin resonance profiles for $Pr_{0.65}Ca_{0.35}MnO_3$ powder at temperature range between 300 K to 120 K.

Figure II - 9 Temperature dependence of electron-spin resonance linewidth ΔH_{p-p} (+) and the effective spin susceptibility $\chi_{eff.}$ (o) for $Pr_{0.65}Ca_{0.35}MnO_3$ powder from 300 K down to 10 K. The PI, COI, AFI, and CAFI denote the paramagnetic insulator, the charge-ordered insulator, antiferromagnetic insulator, and canted antiferromagnetic insulator, respectively. T_{CO}, T_N and T_{CA} denote charge-ordering transition temperature, Néel temperature, canted antiferromagnetic transition temperature, respectively.

Figure II - 10 A block diagram showing the energy flow paths for the Mn^{4+} and Mn^{3+} spin subsystems and the lattice. The relaxation rate R_{ab} represents relaxation from subsystem a to subsystem b. The thickness of the arrows is a measure of the

magnitude of the particular relaxation rate R_{ab}

Figure II - 11 D.c. magnetization for $Pr_{0.65}Ca_{0.35}MnO_3$ powder as a function of temperature from 300 K down to 10 K.

Figure II - 12 Electron spin resonance profiles for $Pr_{0.65}Ca_{0.35}MnO_3$ powder at temperature range between 105 K to 75 K.

Figure II - 13 D.c. magnetization as a function of temperature in $Pr_{0.65}Ca_{0.35}MnO_3$ powder. FC(C), FC(W) and ZFC denote, the magnetization in the coolong run after field cooling run, the warming run after field cooling run, the warming run after zero field cooling, respectively. Measurements have been done under the magnetic field 0.1 T. In the zero field cooling (ZFC), measurements were performed after sample was cooled to a prescribed temperature under zero field.

Figure III - 1 (a), (b) ESR profiles for $Pr_{0.65}Ca_{0.35}MnO_3$ powder without optical excitation (Dark) and with optical excitation by Nd-YAG laser (photon energy, hυ = 1.17 eV).

Figure III - 2 (a), (b) ESR profiles for $Pr_{0.65}Ca_{0.35}MnO_3$ powder without optical excitation (Dark) and with optical excitation by He-Ne laser (photon energy, hυ = 1.96 eV).

Figure III - 3 ESR profiles for $Pr_{0.65}Ca_{0.35}MnO_3$ powder at 80K, 50K and 40K under optical excitations by Nd-YAG laser (photon energy, hυ = 1.17 eV) and by Nd-YAG laser (photon energy, hυ = 1.96 eV), where obvious change in ESR profiles, at the CAF state temperature region.

Figure III - 4 ESR profiles for $Pr_{0.65}Ca_{0.35}MnO_3$ powder at 80K and 50K under different excitation power by Nd-YAG laser (photon energy, hυ = 1.17 eV).

Figure IV - 1 Temperature dependence of the integrated intensity of superlattice reflection at (3, 0.5, 2) which is one of the prominent superlattice reflections below $T_{CO} \sim 215$ K in the $Pr_{0.65}Ca_{0.35}MnO_3$ powder at temperature range from 240 K down to 30 K.

Figure IV - 2 Powder x-ray diffraction profiles for $Pr_{0.65}Ca_{0.35}MnO_3$ powder at 30 K (a) and 40 K (b) from (2, 1.5, 0), (2 ,0.5, 2) and (1, 1, 3) reflections with (dotted curve) and without (solid curve) Nd-YAG cw laser irradiation (photon energy, hυ = 1.17 eV).

Figure IV - 3 The schematic the electronic structure of the Mn^{3+} and Mn^{4+} ions in $Pr_{0.65}Ca_{0.35}MnO_3$ and possible optical charge transitions.

Figure V - 1 The x-ray diffraction profiles (Cu-$K\alpha$) around [002] of $Pr_{0.65}Ca_{0.35}MnO_3$ (PCMO) thin film in addition to the [002] line from the $SrTiO_3$ [001] substrate at 290 K

Figure V - 2 The temperature dependence of the dR/dT of $Pr_{0.65}Ca_{0.35}MnO_3$ (PCMO) thin film.

Figure V - 3 Temperature dependence of the X-band ESR profiles for $Pr_{0.65}Ca_{0.35}MnO_3$ (PCMO) thin film without (Dark) and with the photon injection under $H_0 \perp$ c-axis geometry.

Figure VI - 1 The x-ray diffraction (Cu-$K\alpha$) profiles around [002] of $La_{0.67}Ca_{0.33}MnO_3$ (LCMO) and $Pr_{0.65}Ca_{0.35}MnO_3$ (PCMO) thin films in addition to the [002] line from the $SrTiO_3$ [001] substrate at 290 K. The lengths of the c-axis were 3.884 Å and 3.843 Å in LCMO and PCMO, respectively.

Figure VI - 2 The temperature dependence of d. c. resistivity of $Pr_{0.65}Ca_{0.35}MnO_3$ (PCMO) and $La_{0.67}Ca_{0.33}MnO_3$ (LCMO) thin film samples. PCMO films exhibit the semiconductive behavior with the activation energy of 48 meV. The LCMO film shows the insulator - metal transition at 260 K (Tc) together with a large CMR.

Figure VI - 3 Temperature dependence of the X-band ESR profiles for $La_{0.67}Ca_{0.33}MnO_3$ (LCMO) thin-films without the photon injection (Dark) under $H_0 \perp$ c-axis geometry.

Figure VI - 4 The temperature dependence of the resonance magnetic field of the ESR spectrum (closed circles) in $Pr_{0.65}Ca_{0.35}MnO_3$ (PCMO) and $La_{0.67}Ca_{0.33}MnO_3$ (LCMO) thin films. The broken curves show the calculated values for $(\Delta g)^2$ which is defined as an order parameter under the Landau theory of the second-order phase transition.

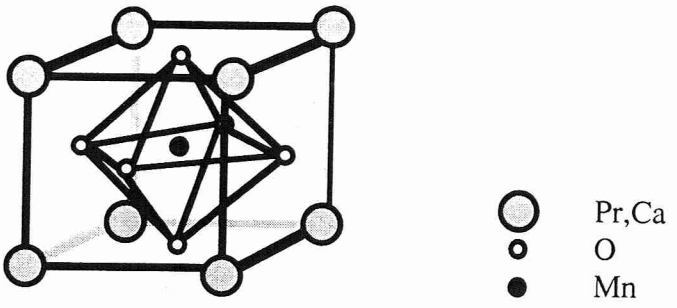

(a) Perovskite Structure

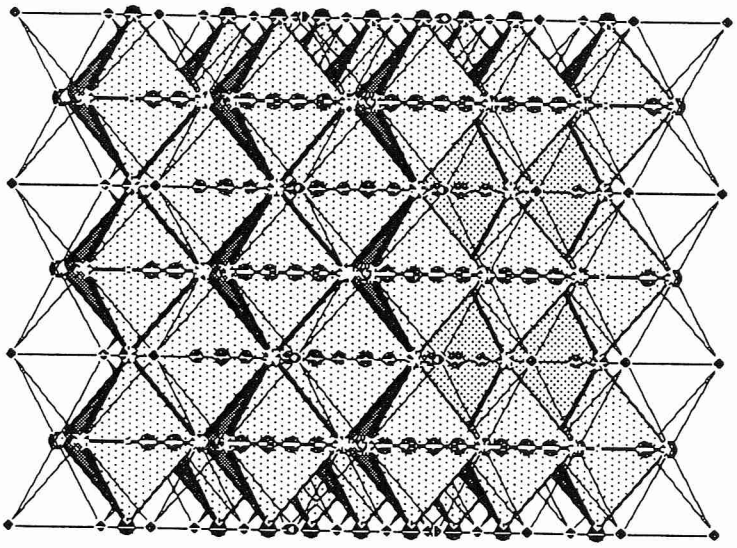

(b) Cubic

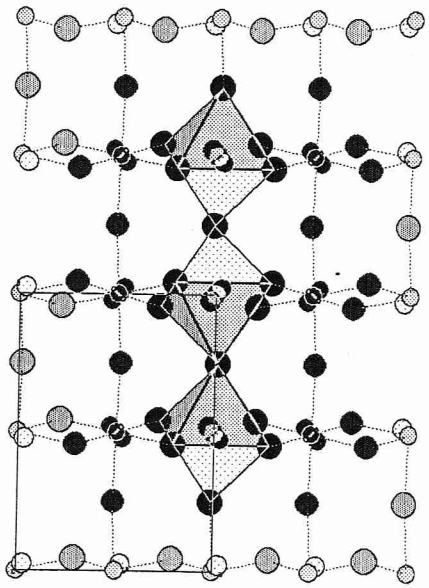

(c) Orthorhombic

Figure I - 1

Eletronic configuration of Mn^{3+} and Mn^{4+} ions

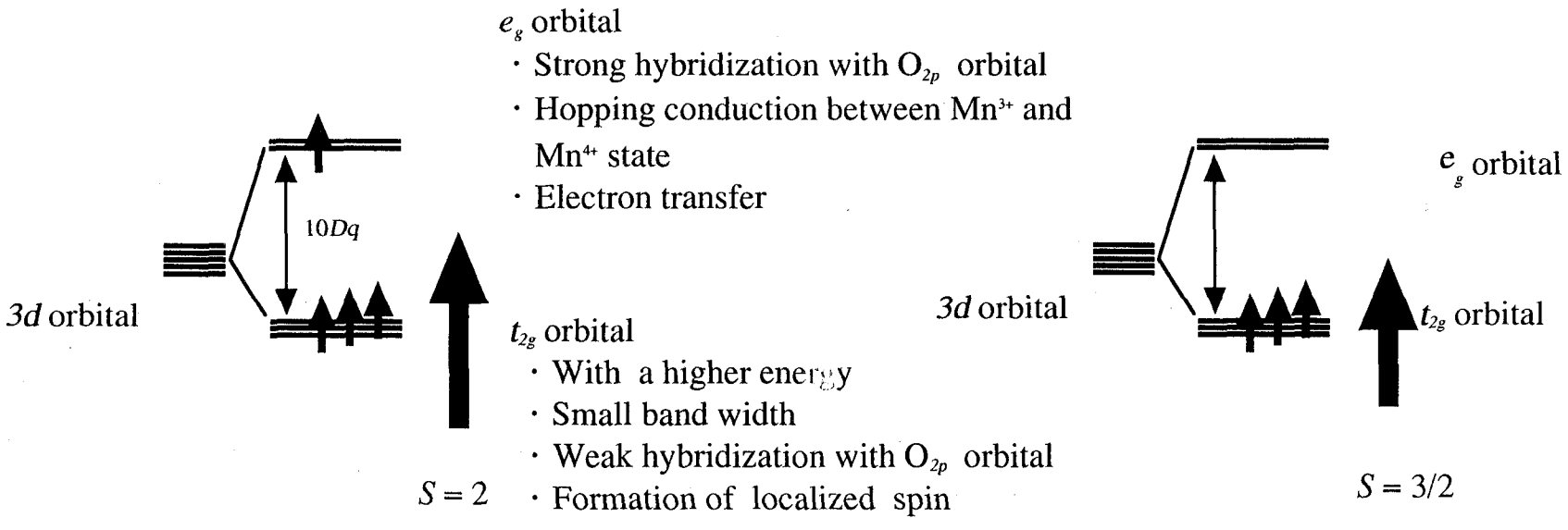

Mn^{3+} ion

Mn^{4+} ion

Figure I - 2

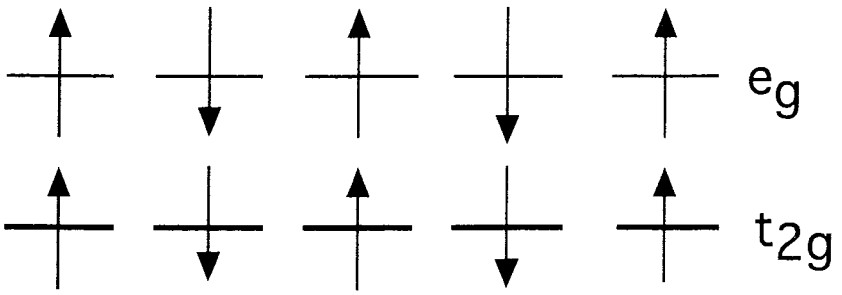

(a) $LaMnO_3$

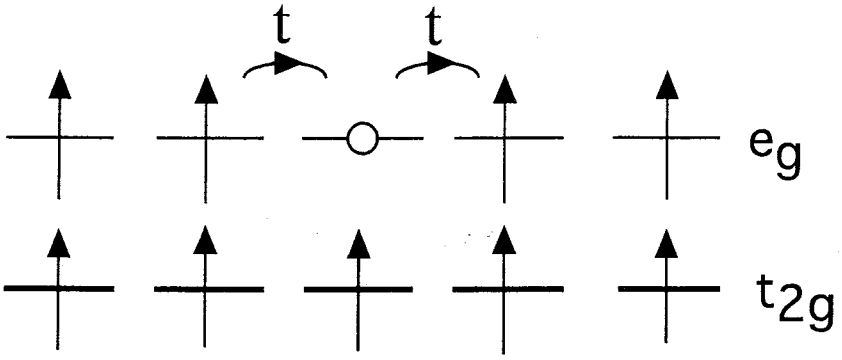

(b) $La_{1-x}Sr_xMnO_3$ ($T \ll T_C$)

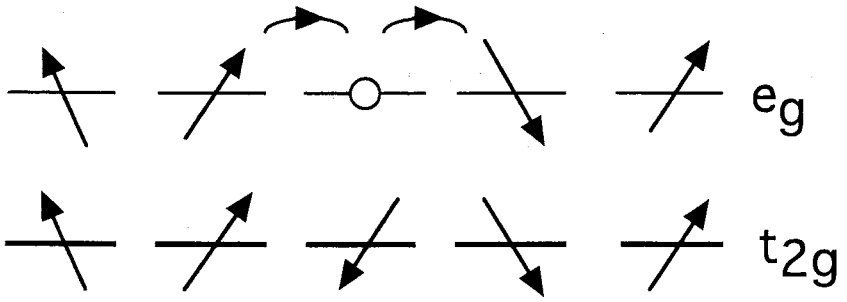

(c) $La_{1-x}Sr_xMnO_3$($T \cong T_C$)

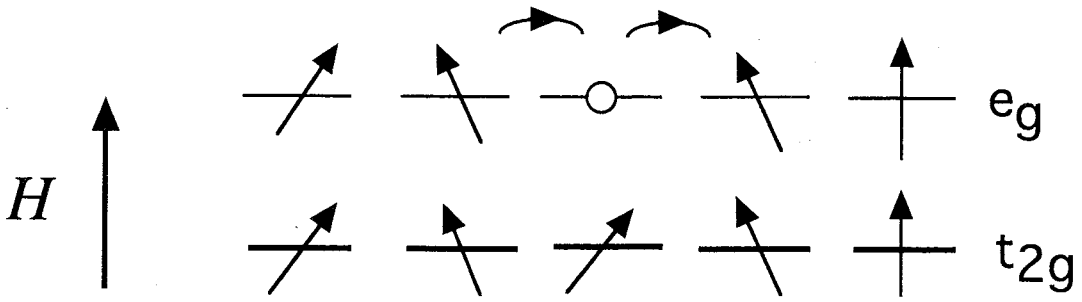

(d) $La_{1-x}Sr_xMnO_3$ ($T \cong T_C$)

Figure 1 - 3

A. Asamitsu *et al.*, Solid State Phys. **32**, 258 (1997)

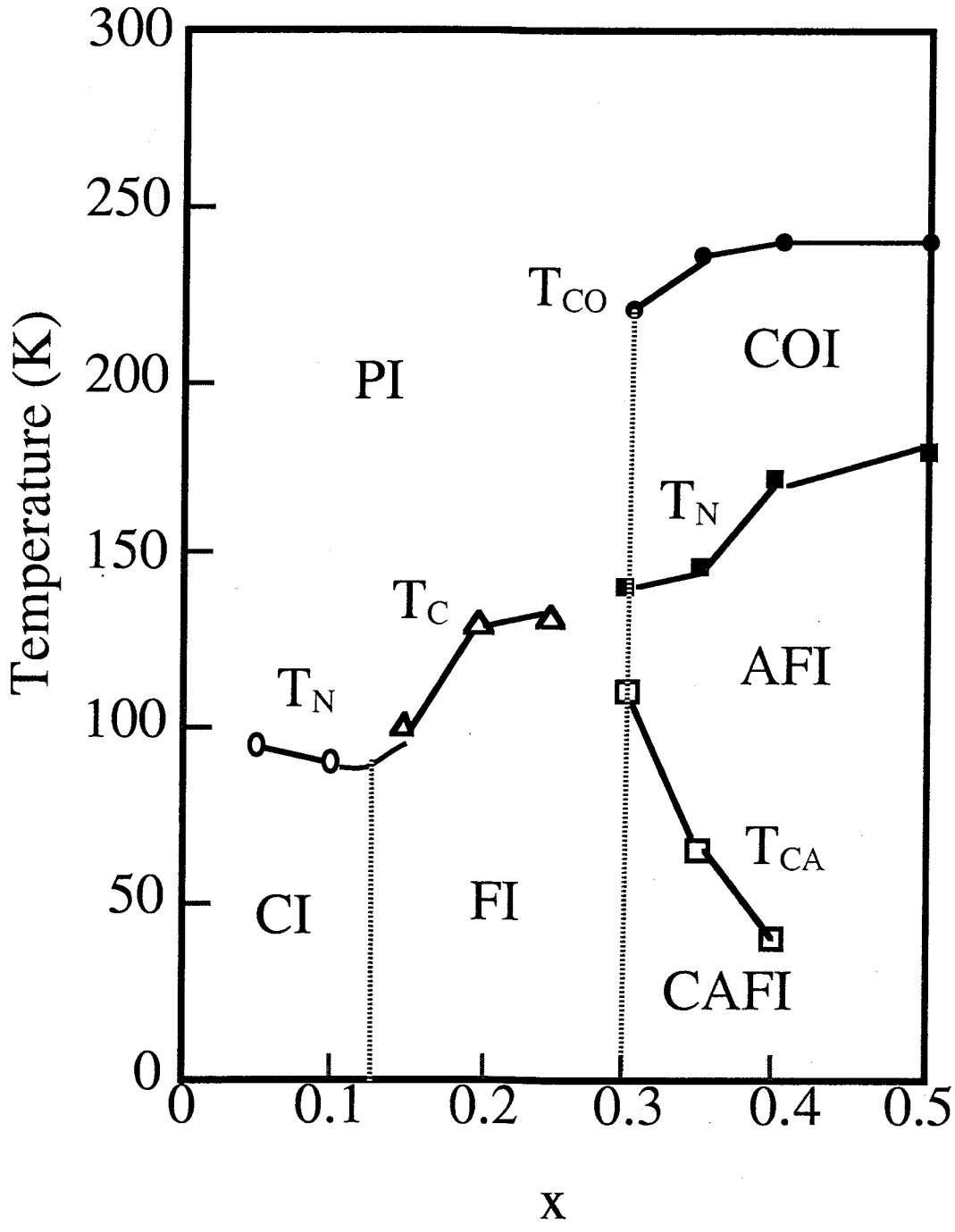

Figure I - 4

Y. Tomioka *et al.*, J. Phys. Soc. Jpn., **65**, 1043 (1996)

A) collinear CE-type spin structure for $T_{CA} \leqq T \leqq T_N$

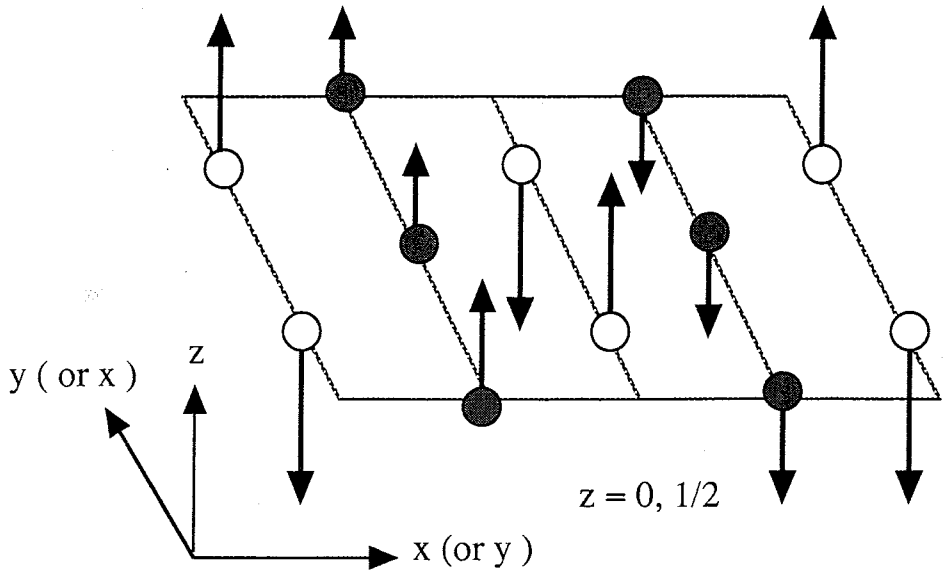

B) canted CE-type spin structure for $T \leqq T_N$

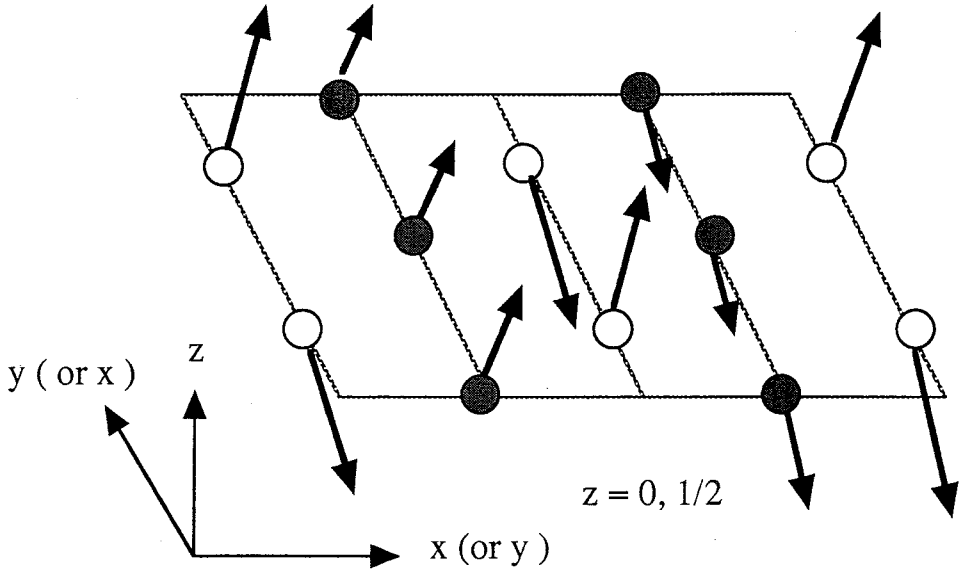

site 1 ○ $\mu_{AF1} \fallingdotseq 1.4 \pm 0.2\,\mu_B$

site 2 ● $\mu_{AF2} \leqq 0.5\,\mu_B$

$\mu_F \fallingdotseq 1.9 \pm 0.2\,\mu_B$

Figure I - 5

H. Yoshizawa *et al.*, Phys. Rev. B, **52**, 13145 (1995)

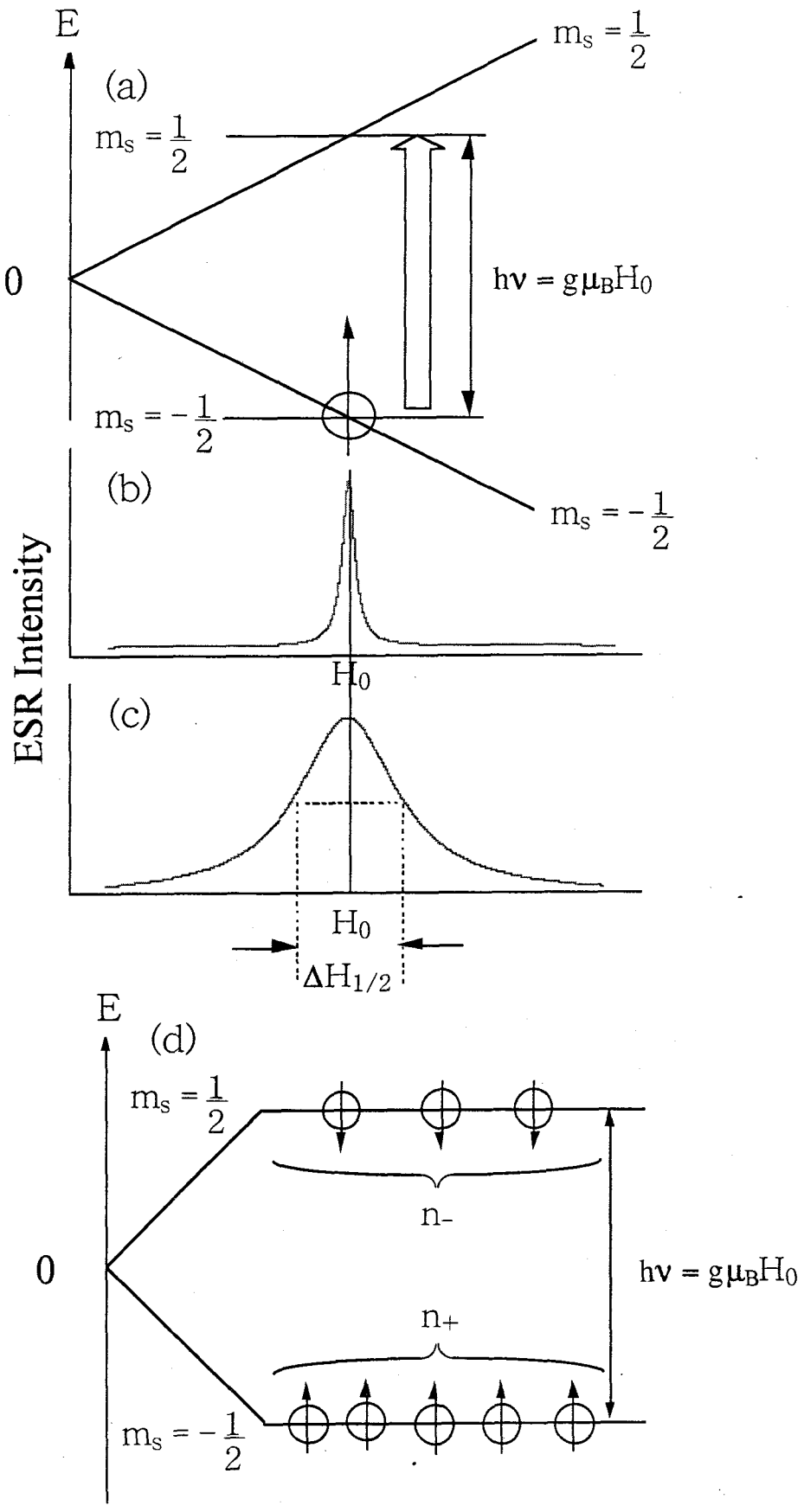
E
(a)
$m_s = \frac{1}{2}$
$m_s = -\frac{1}{2}$
0
$h\nu = g\mu_B H_0$
(b)
(c)
ESR Intensity
H_0
H_0
$\Delta H_{1/2}$
E
(d)
$m_s = \frac{1}{2}$
$m_s = -\frac{1}{2}$
0
n_-
n_+
$h\nu = g\mu_B H_0$

Figure 1-6

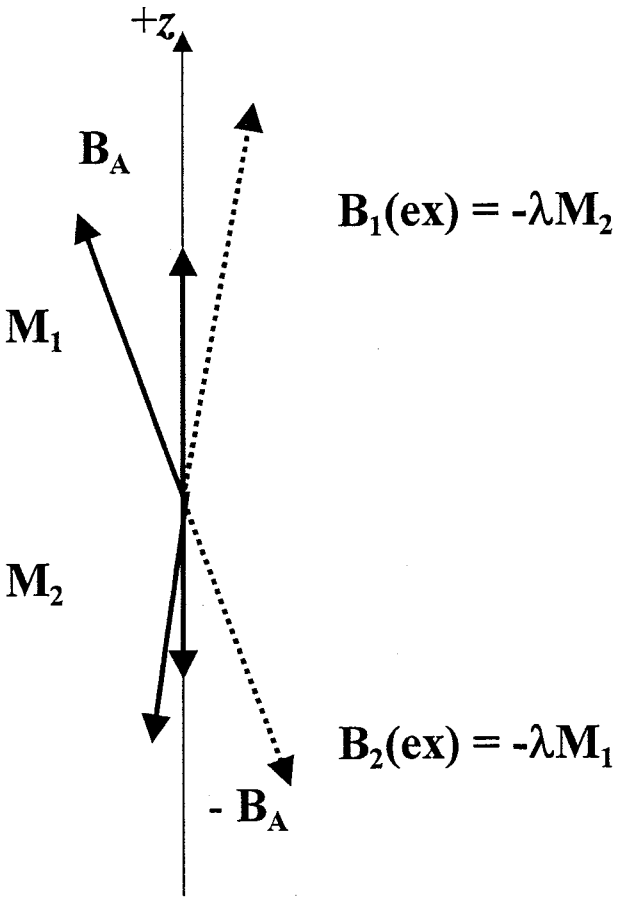

Figure I - 7

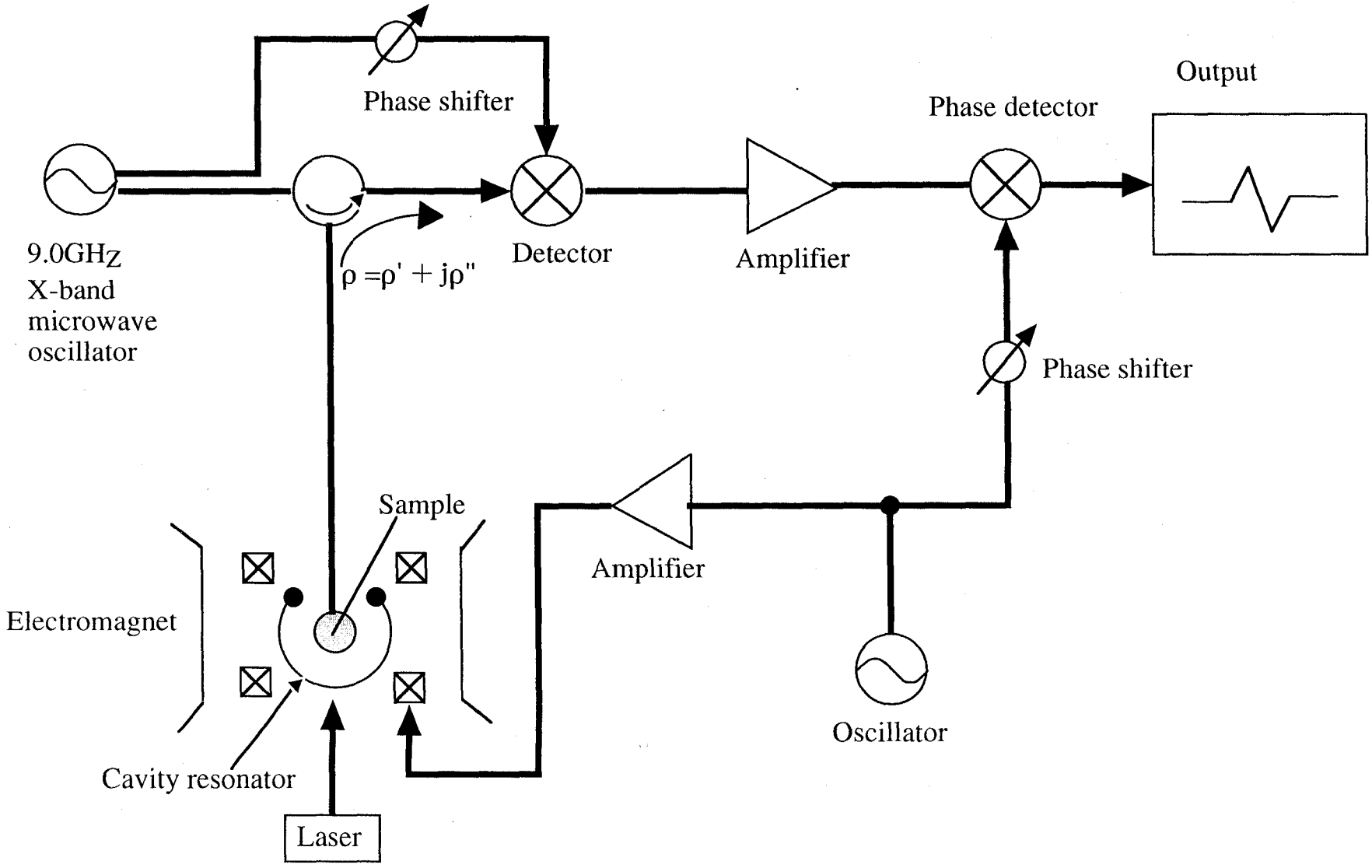
Phase shifter
Output
Phase detector
9.0GHz
X-band
microwave
oscillator
ρ =ρ' + jρ"
Detector
Amplifier
Phase shifter
Sample
Amplifier
Electromagnet
Oscillator
Cavity resonator
Laser

Figure I - 8

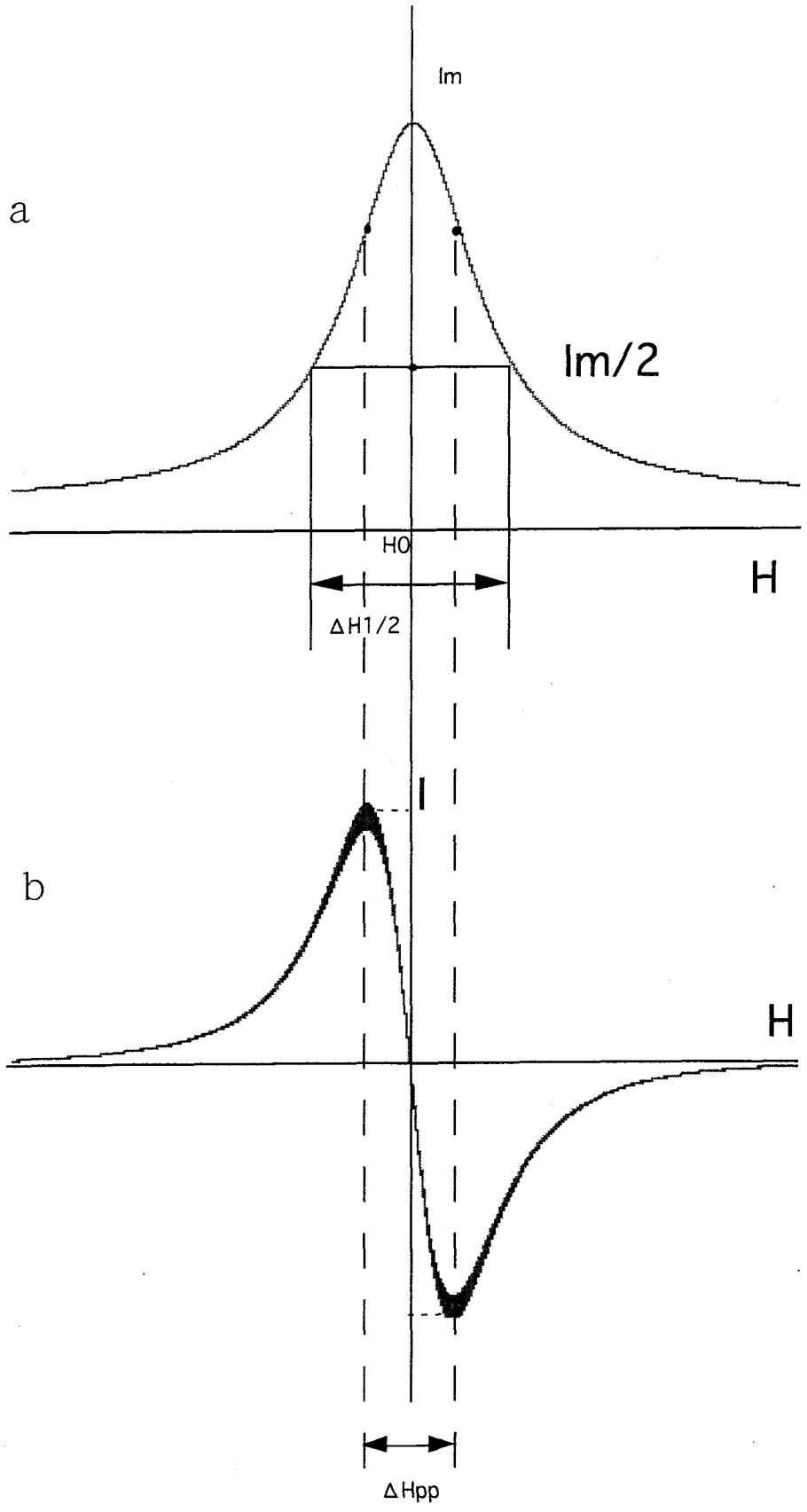

Figure I - 9

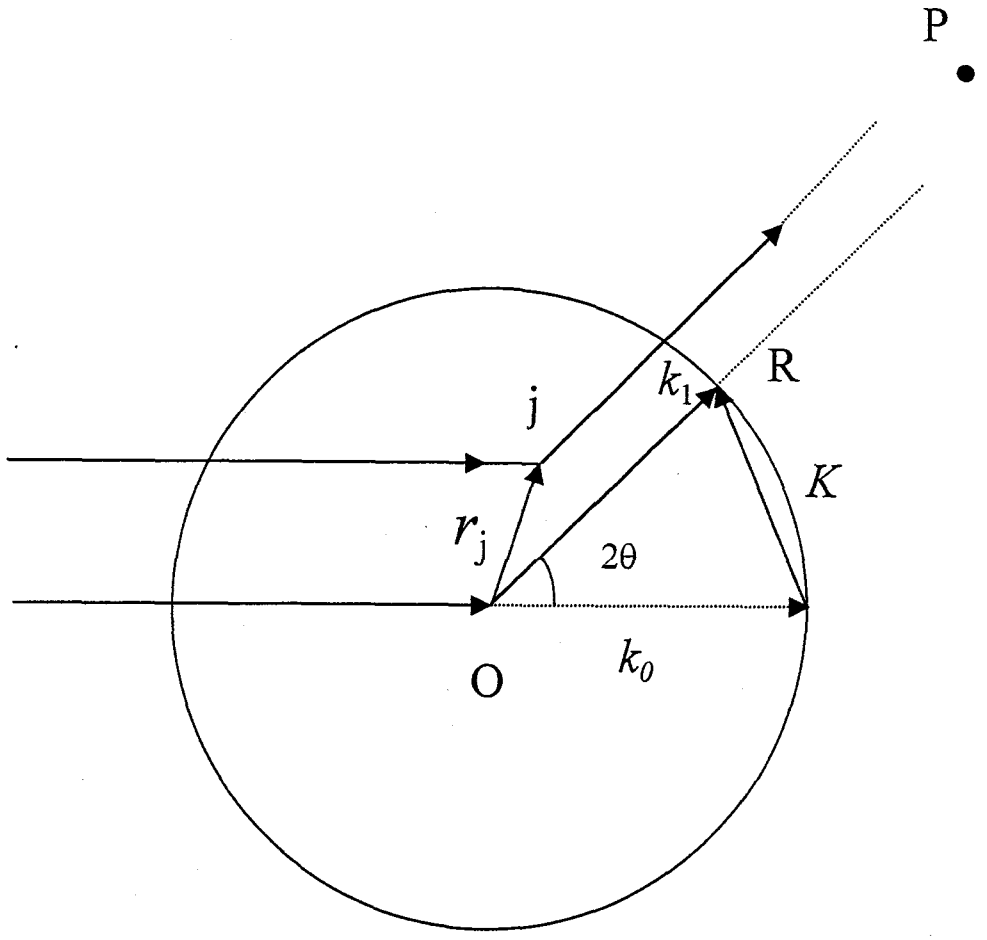

Figure I - 10

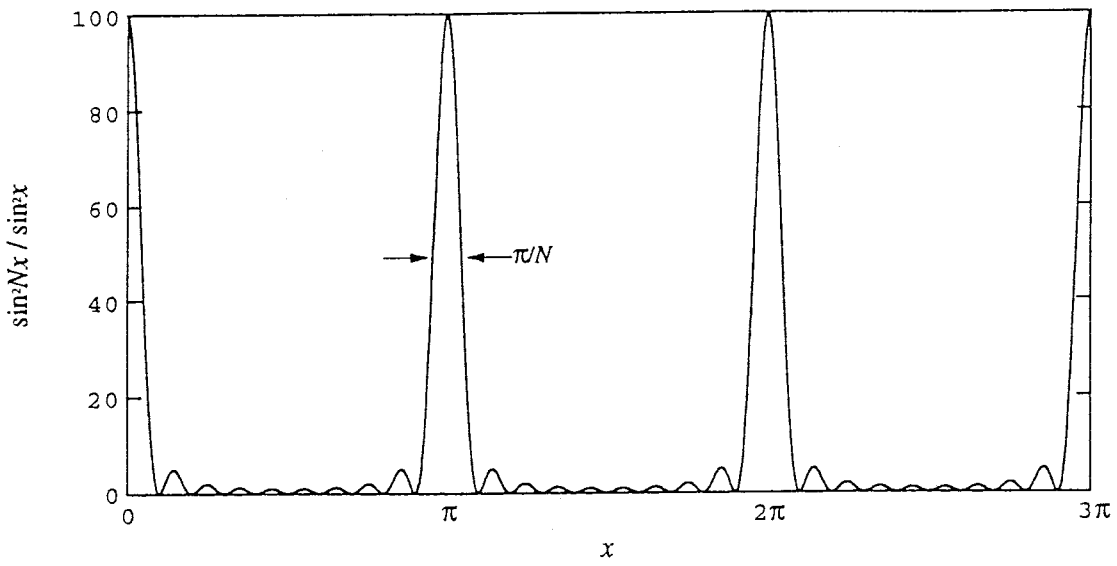

Figure I - 11

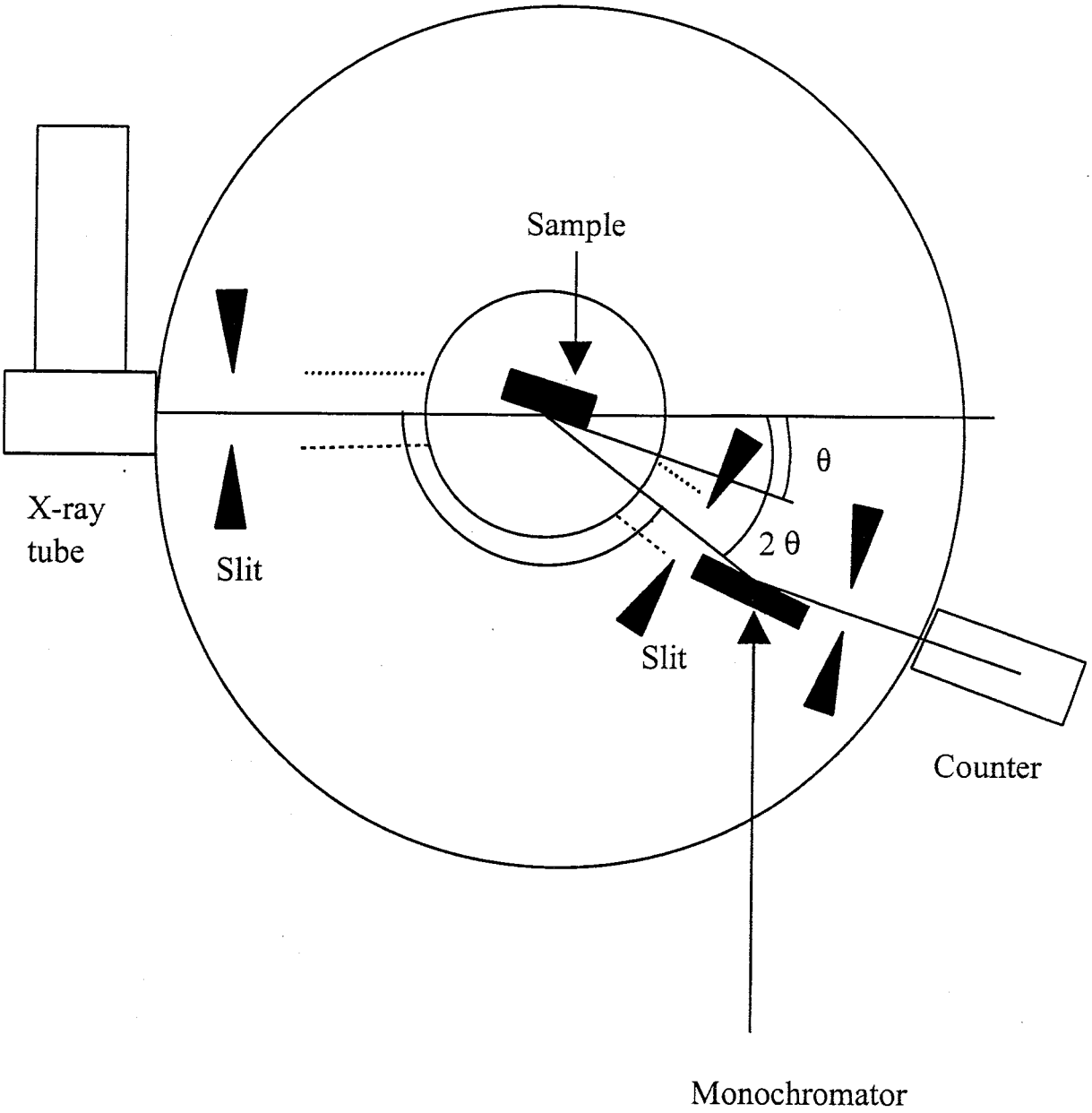

Figure II - 1

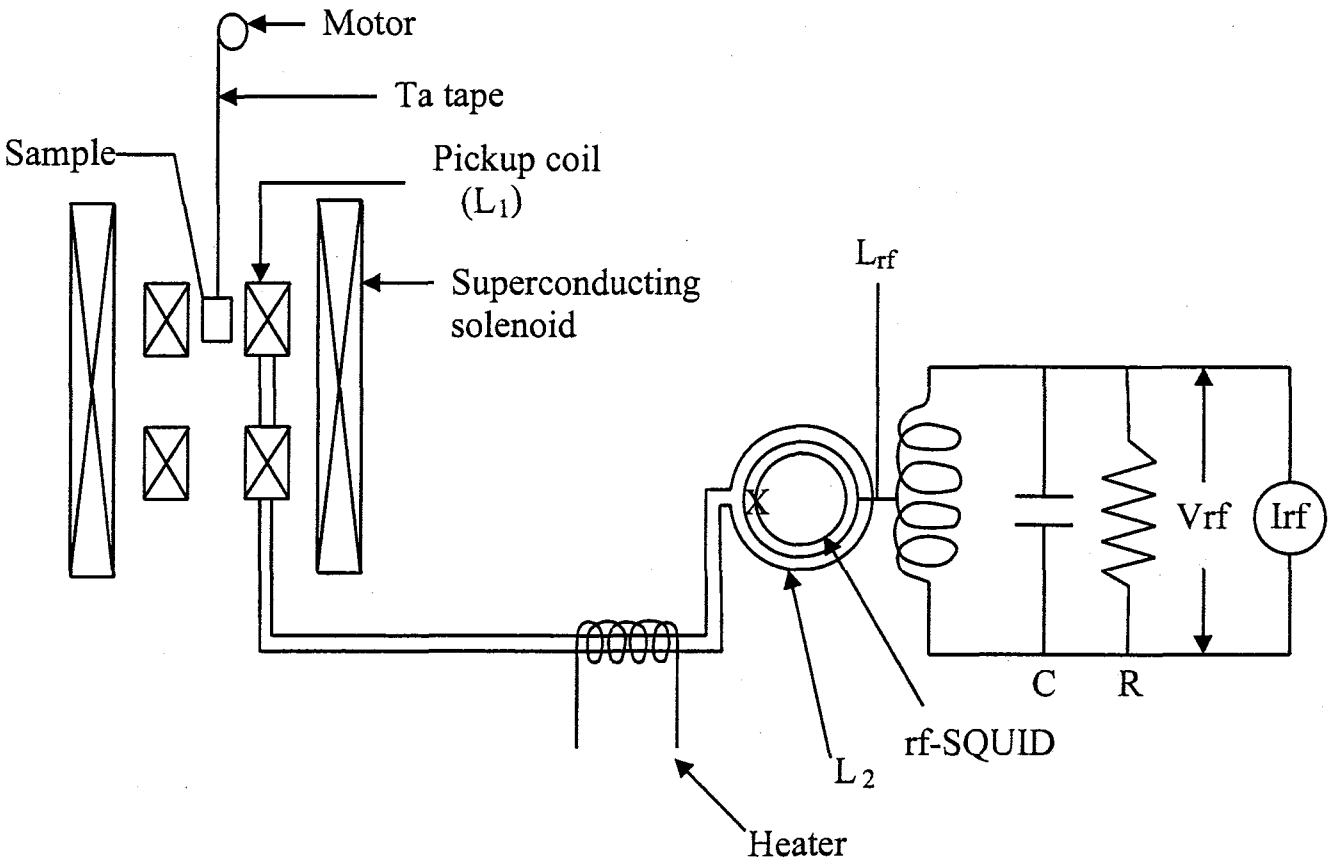
Motor
Ta tape
Sample
Pickup coil
(L_1)
Superconducting
solenoid
L_{rf}
X
Vrf
Irf
C
R
rf-SQUID
L_2
Heater

Figure II - 2

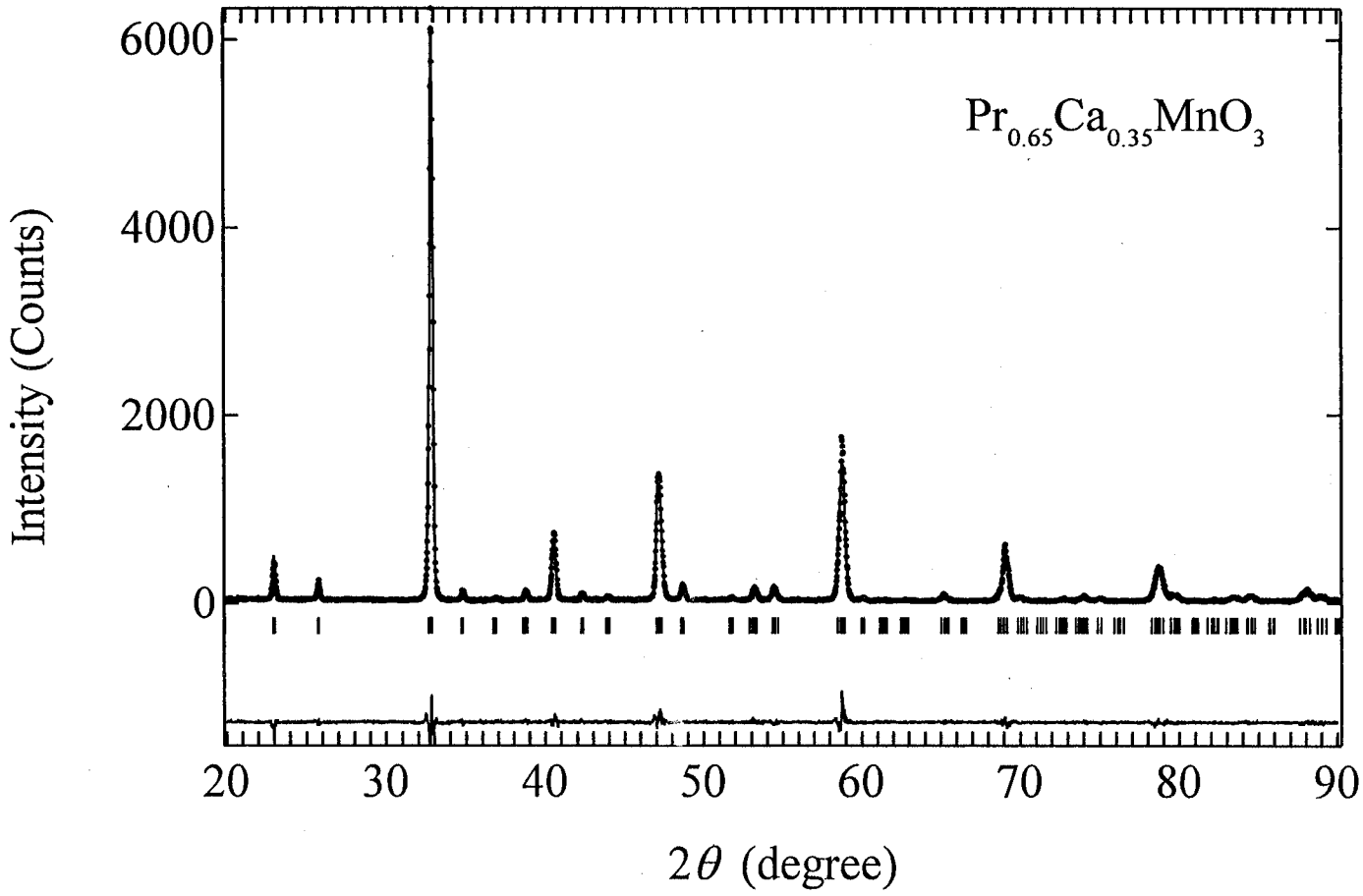
6000
4000
2000
0
Intensity (Counts)
$Pr_{0.65}Ca_{0.35}MnO_3$
20
30
40
50
60
70
80
90
2θ (degree)

Figure II - 3

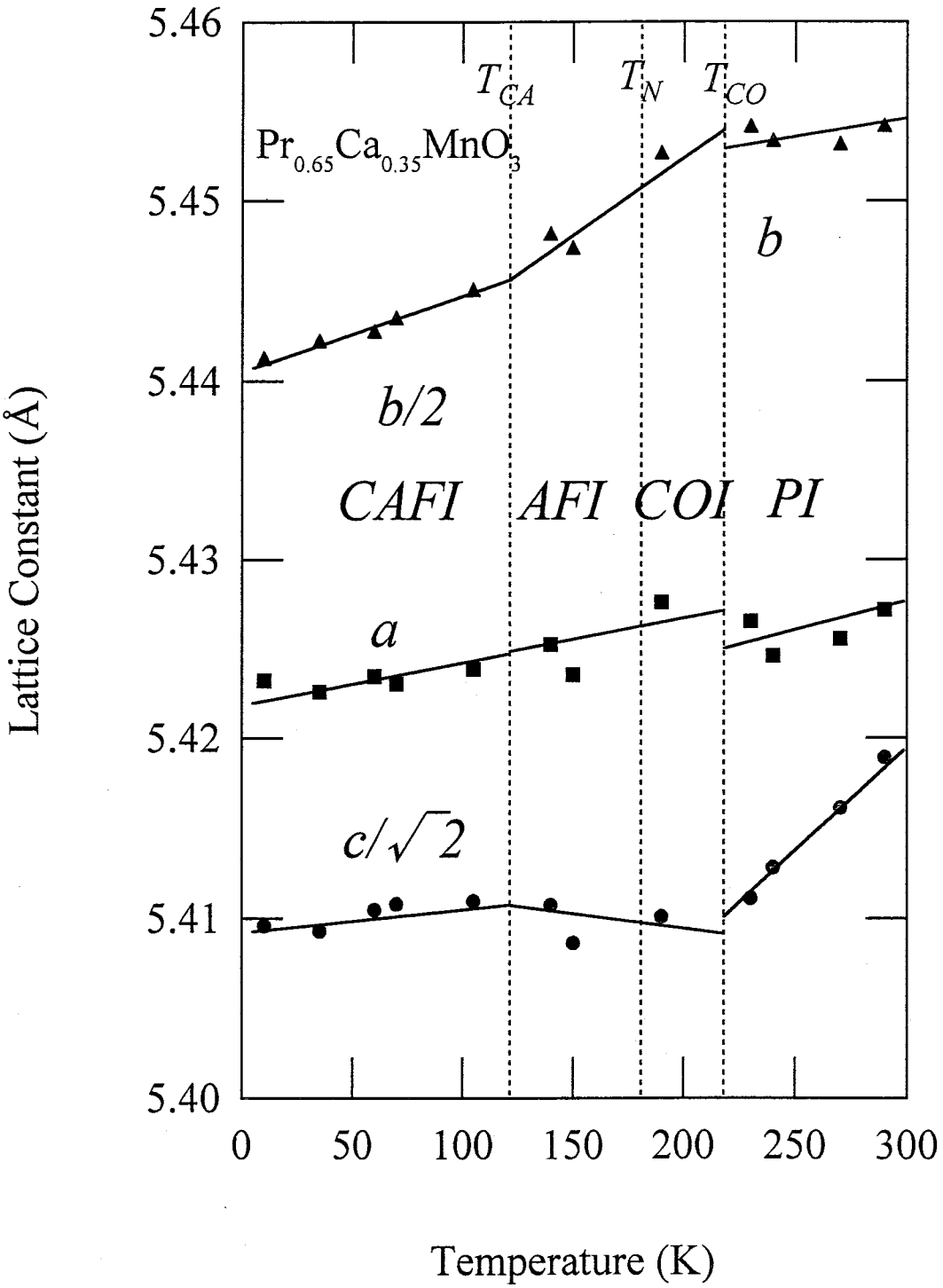
5.46
5.45
5.44
5.43
5.42
5.41
5.40
0
50
100
150
200
250
300
Lattice Constant (Å)
Temperature (K)
T_{CA}
T_N
T_{CO}
$Pr_{0.65}Ca_{0.35}MnO_3$
b
b/2
a
$c/\sqrt{2}$
CAFI
AFI
COI
PI

Figure II - 4

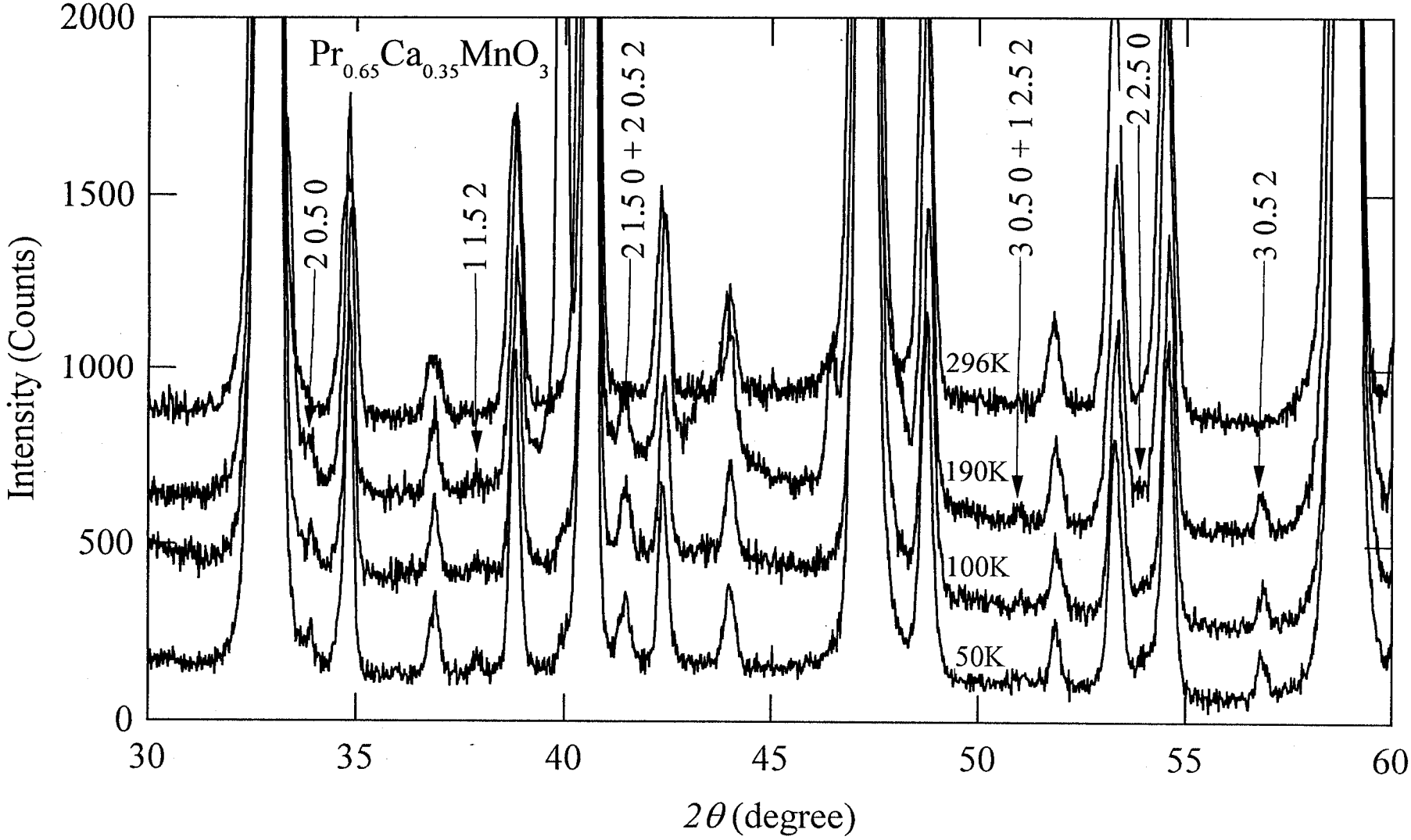
$Pr_{0.65}Ca_{0.35}MnO_3$
2 0.5 0
1 1.5 2
2 1.5 0 + 2 0.5 2
3 0.5 0 + 1 2.5 2
2 2.5 0
3 0.5 2
296K
190K
100K
50K
Intensity (Counts)
2000
1500
1000
500
0
30
35
40
45
50
55
60
2θ (degree)

Figure II - 5

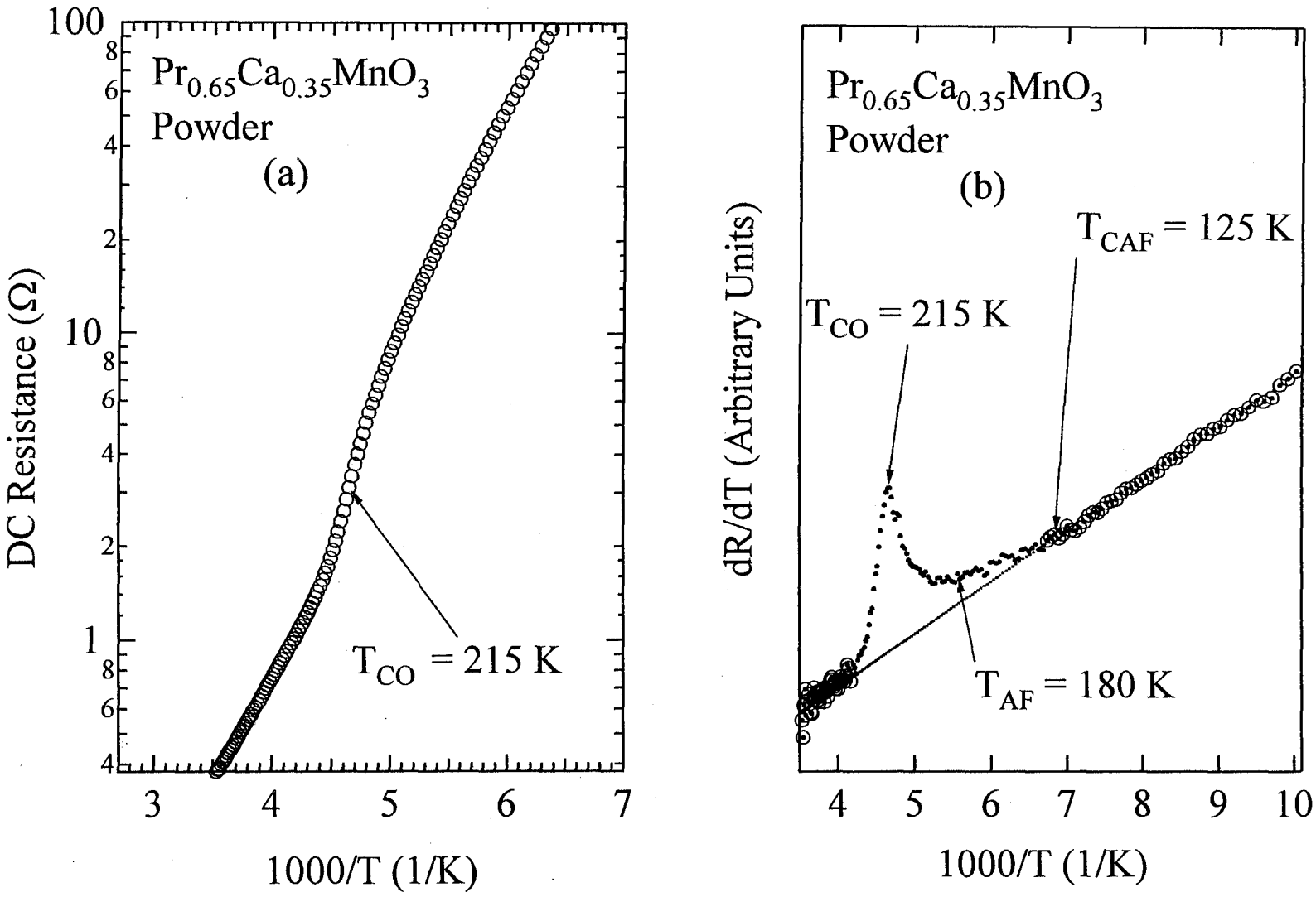
100
8
6
4
2
10
8
6
4
2
1
8
6
4
DC Resistance (Ω)
$Pr_{0.65}Ca_{0.35}MnO_3$
Powder
(a)
T_{CO} = 215 K
3
4
5
6
7
1000/T (1/K)
$Pr_{0.65}Ca_{0.35}MnO_3$
Powder
(b)
T_{CAF} = 125 K
T_{CO} = 215 K
T_{AF} = 180 K
dR/dT (Arbitrary Units)
4
5
6
7
8
9
10
1000/T (1/K)

Figure II - 6

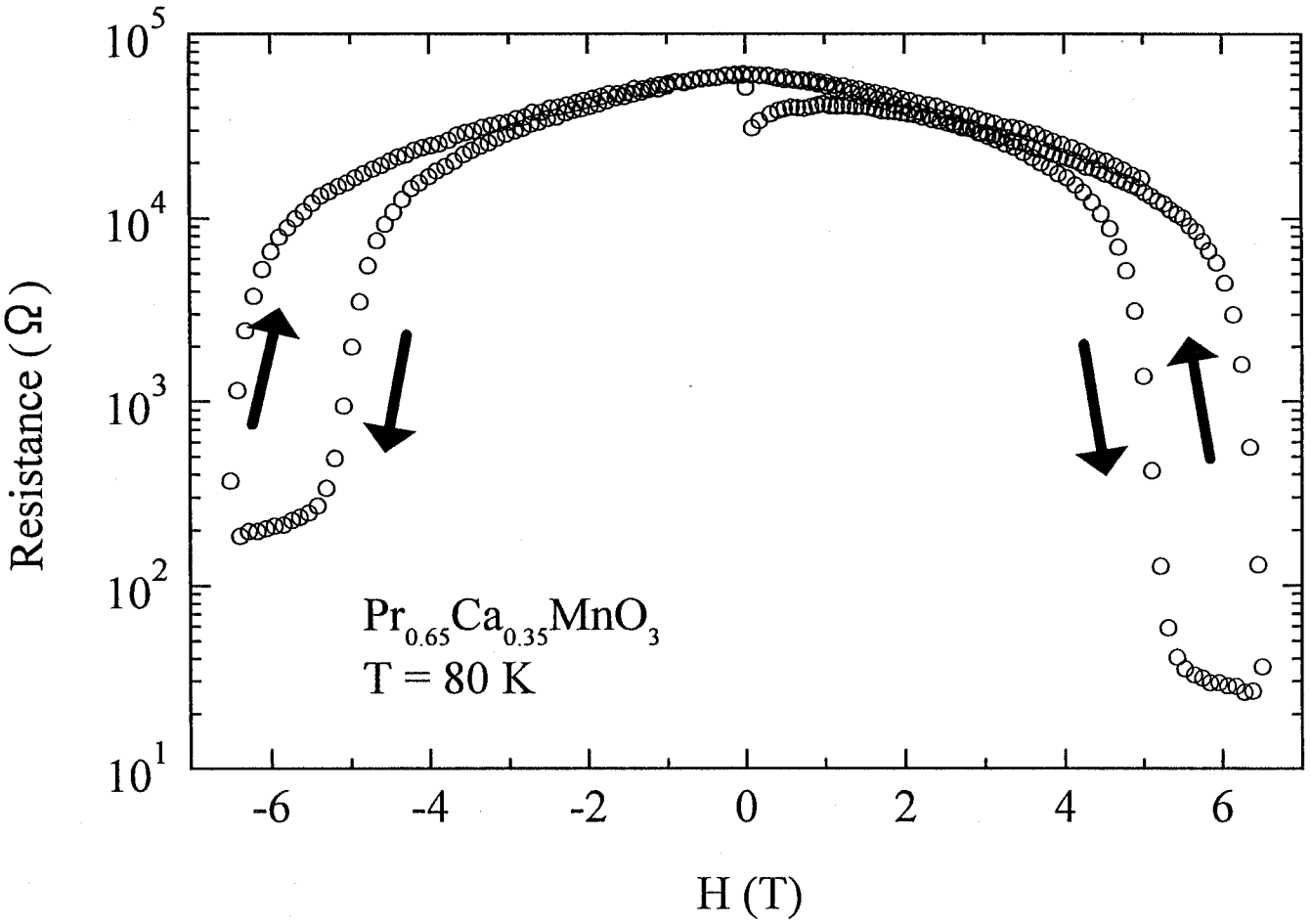
Resistance (Ω)
10^5
10^4
10^3
10^2
10^1
$Pr_{0.65}Ca_{0.35}MnO_3$
T = 80 K
-6
-4
-2
0
2
4
6
H (T)

Figure II - 7

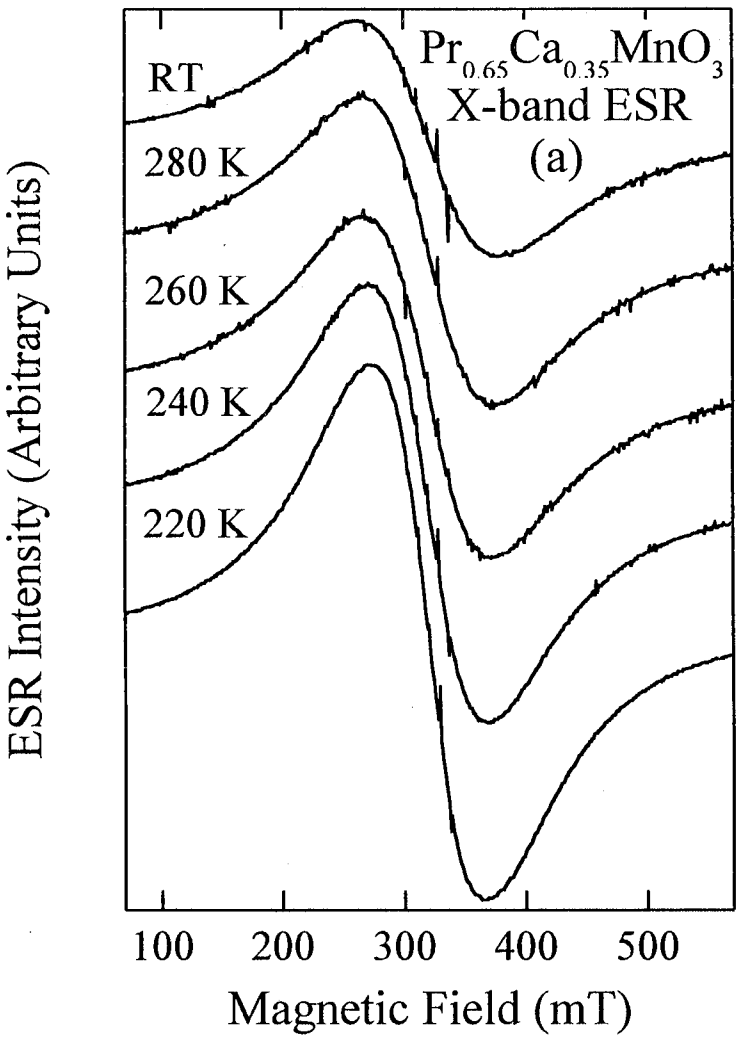
RT
280 K
260 K
240 K
220 K
$Pr_{0.65}Ca_{0.35}MnO_3$
X-band ESR
(a)
ESR Intensity (Arbitrary Units)
100
200
300
400
500
Magnetic Field (mT)

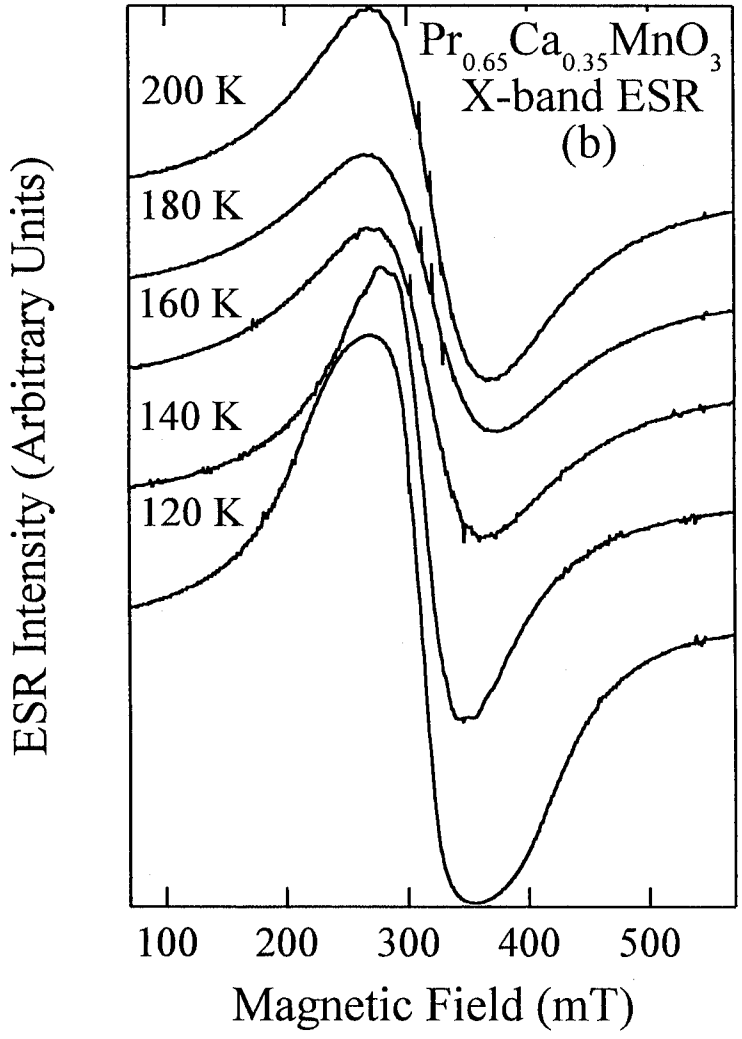
200 K
180 K
160 K
140 K
120 K
$Pr_{0.65}Ca_{0.35}MnO_3$
X-band ESR
(b)
ESR Intensity (Arbitrary Units)
100
200
300
400
500
Magnetic Field (mT)

Figure II - 8

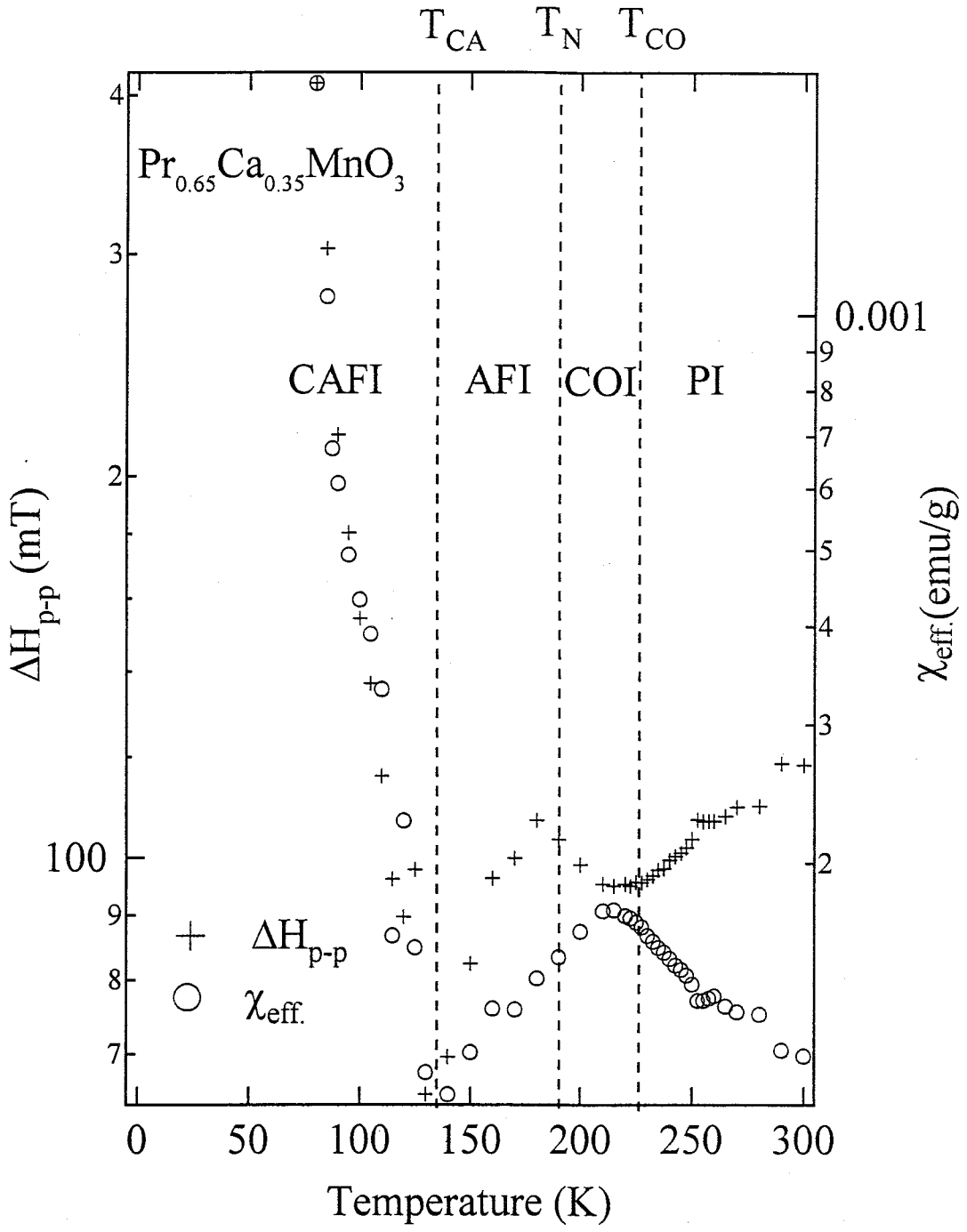
T_{CA} T_N T_{CO}
$Pr_{0.65}Ca_{0.35}MnO_3$
CAFI
AFI
COI
PI
ΔH_{p-p} (mT)
$\chi_{eff.}$(emu/g)
0.001
100
ΔH_{p-p}
$\chi_{eff.}$
0 50 100 150 200 250 300
Temperature (K)

Figure II - 9

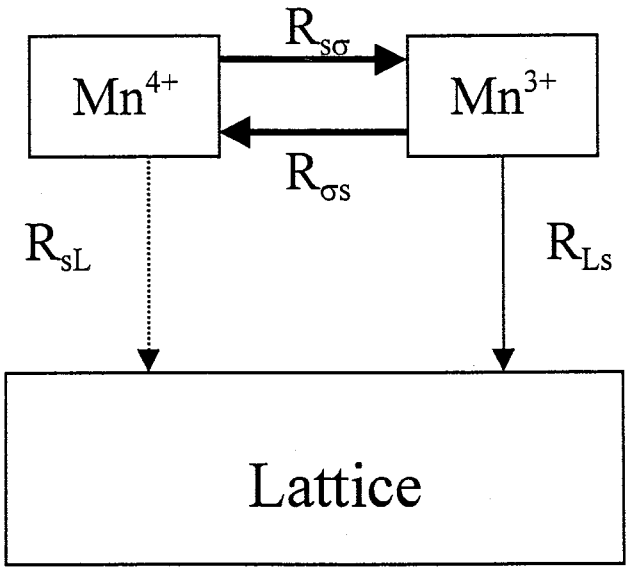

Figure II - 10

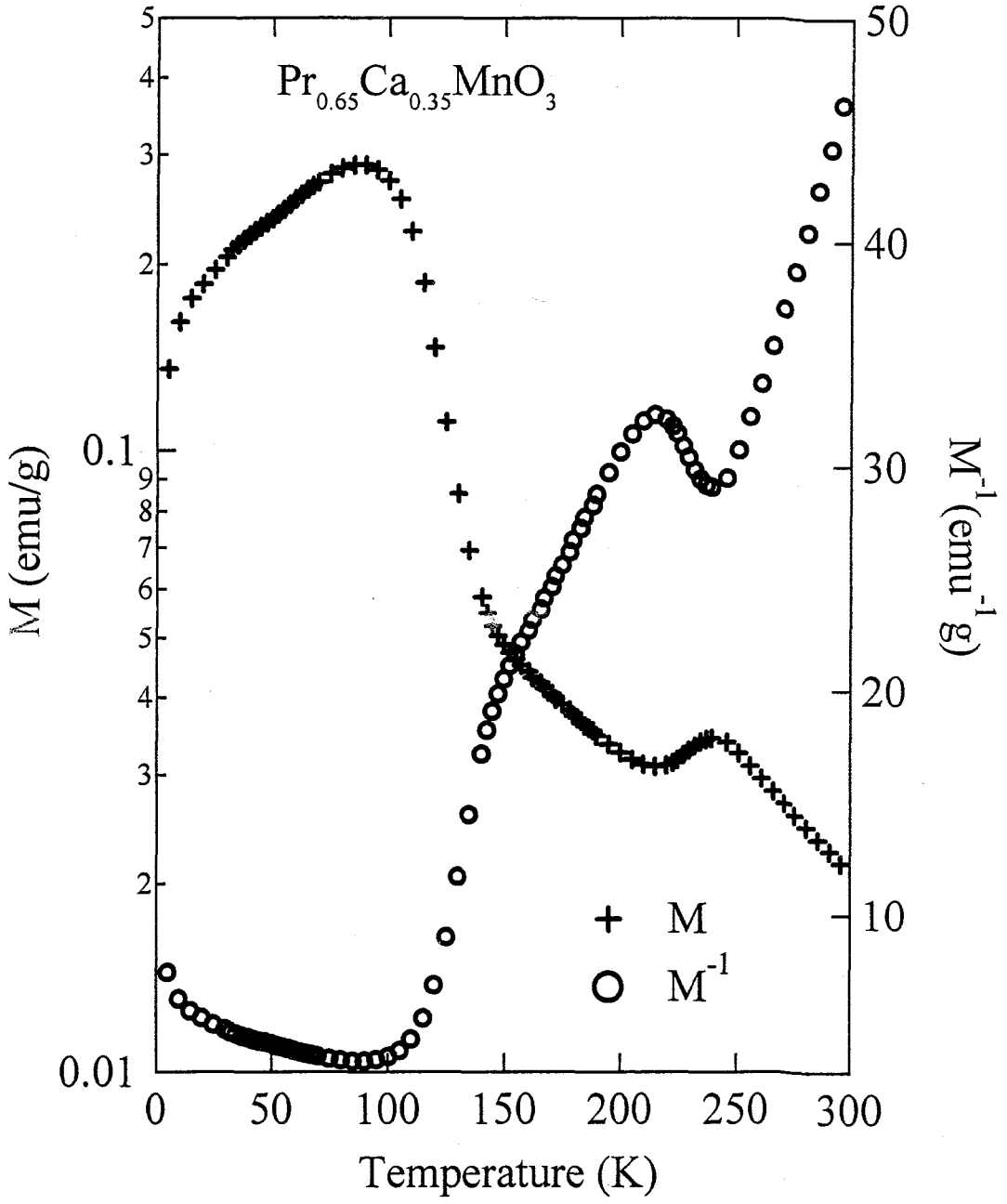
$Pr_{0.65}Ca_{0.35}MnO_3$
M (emu/g)
M^{-1} (emu^{-1} g)
Temperature (K)
M
M^{-1}
0.01
0.1
0
50
100
150
200
250
300
10
20
30
40
50

Figure II - 11

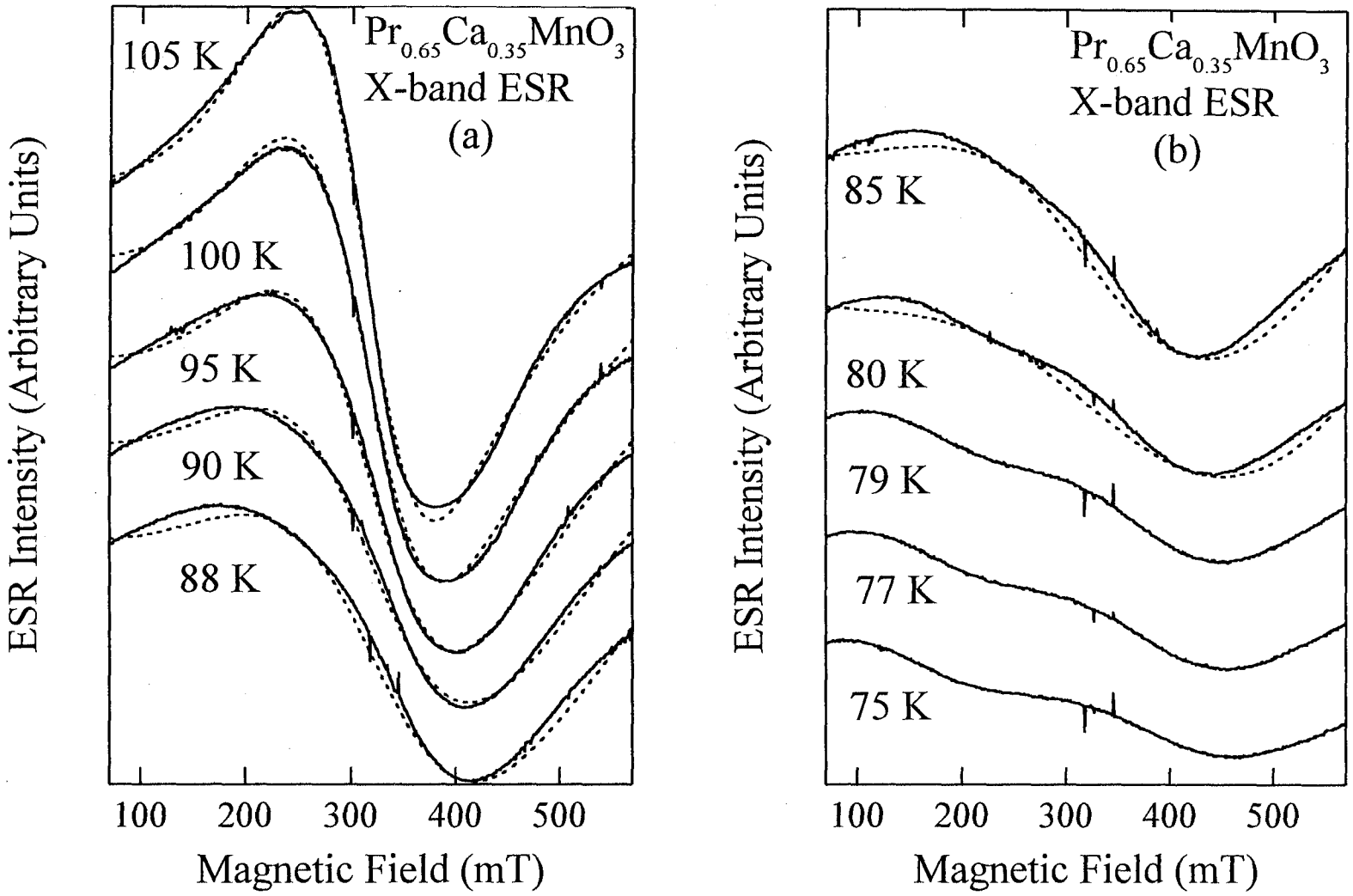
105 K
100 K
95 K
90 K
88 K
$Pr_{0.65}Ca_{0.35}MnO_3$
X-band ESR
(a)
ESR Intensity (Arbitrary Units)
100
200
300
400
500
Magnetic Field (mT)
85 K
80 K
79 K
77 K
75 K
$Pr_{0.65}Ca_{0.35}MnO_3$
X-band ESR
(b)
ESR Intensity (Arbitrary Units)
100
200
300
400
500
Magnetic Field (mT)

Figure II - 12

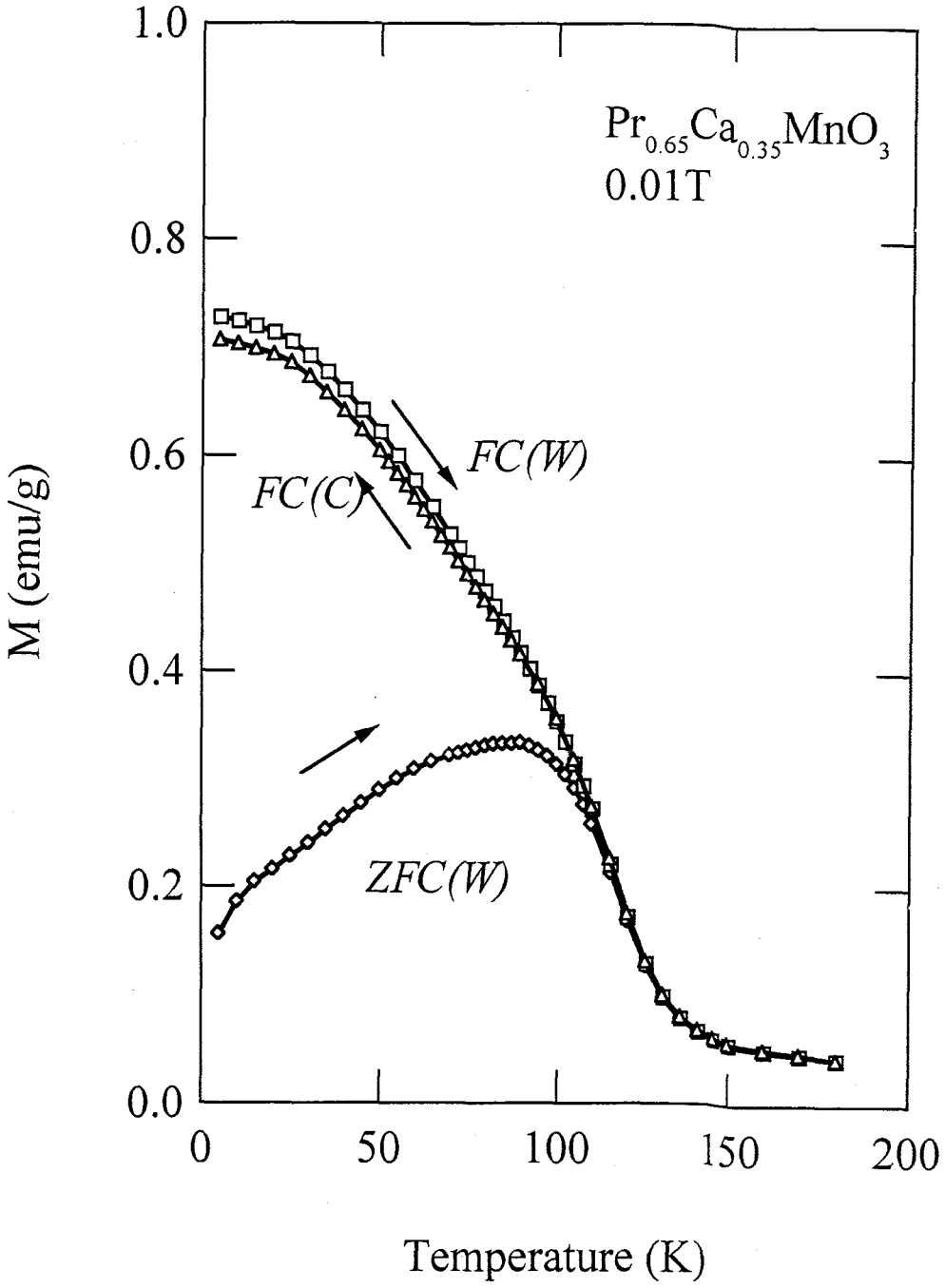
1.0
0.8
0.6
0.4
0.2
0.0
M (emu/g)
0
50
100
150
200
Temperature (K)
$Pr_{0.65}Ca_{0.35}MnO_3$
0.01T
FC(W)
FC(C)
ZFC(W)

Figure II - 13

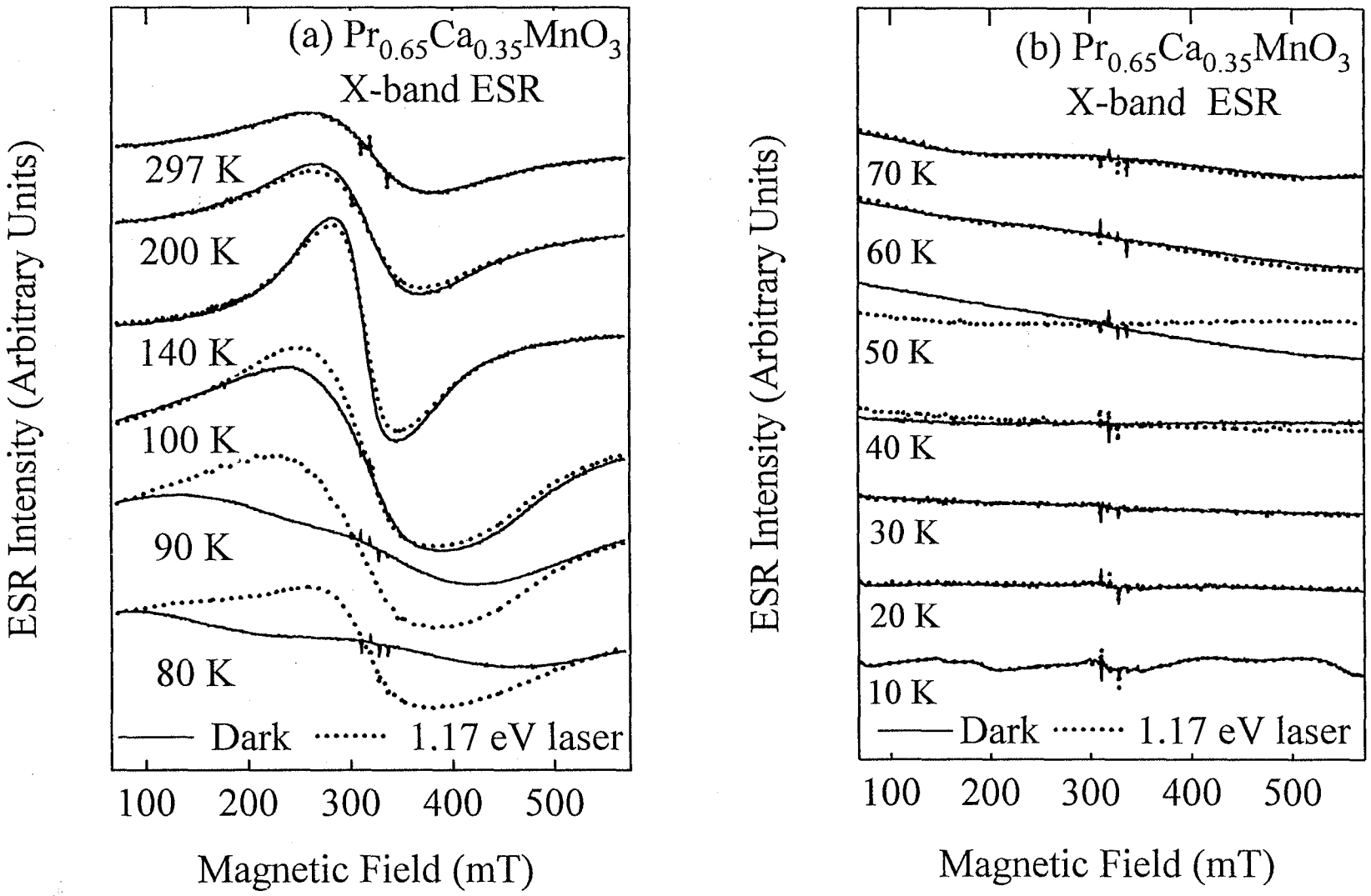
(a) $Pr_{0.65}Ca_{0.35}MnO_3$
X-band ESR
297 K
200 K
140 K
100 K
90 K
80 K
Dark
1.17 eV laser
ESR Intensity (Arbitrary Units)
100
200
300
400
500
Magnetic Field (mT)
(b) $Pr_{0.65}Ca_{0.35}MnO_3$
X-band ESR
70 K
60 K
50 K
40 K
30 K
20 K
10 K
Dark
1.17 eV laser
ESR Intensity (Arbitrary Units)
100
200
300
400
500
Magnetic Field (mT)

Figure III - 1

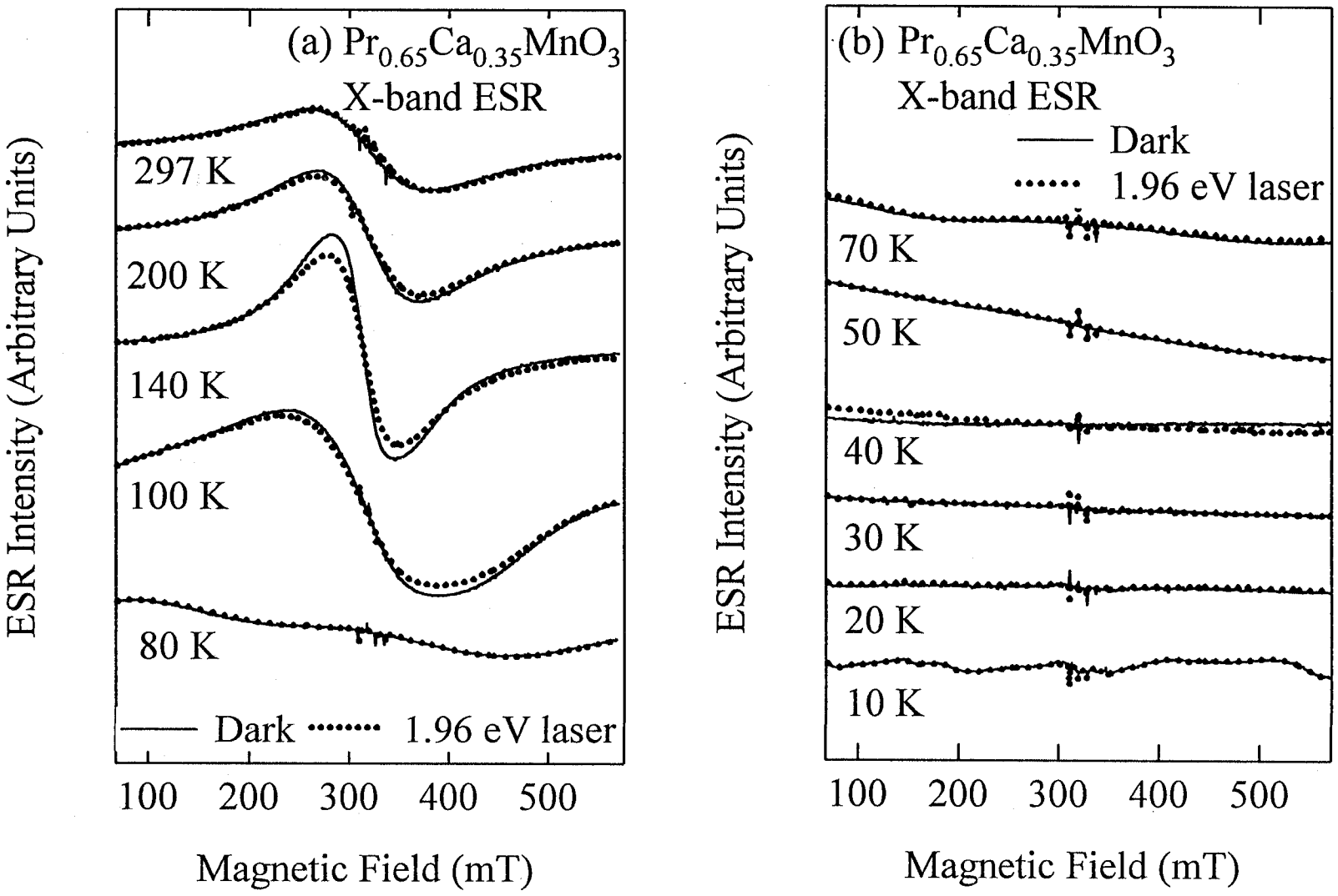
(a) $Pr_{0.65}Ca_{0.35}MnO_3$
X-band ESR
297 K
200 K
140 K
100 K
80 K
Dark
1.96 eV laser
ESR Intensity (Arbitrary Units)
100
200
300
400
500
Magnetic Field (mT)
(b) $Pr_{0.65}Ca_{0.35}MnO_3$
X-band ESR
Dark
1.96 eV laser
70 K
50 K
40 K
30 K
20 K
10 K
ESR Intensity (Arbitrary Units)
100
200
300
400
500
Magnetic Field (mT)

Figure III - 2

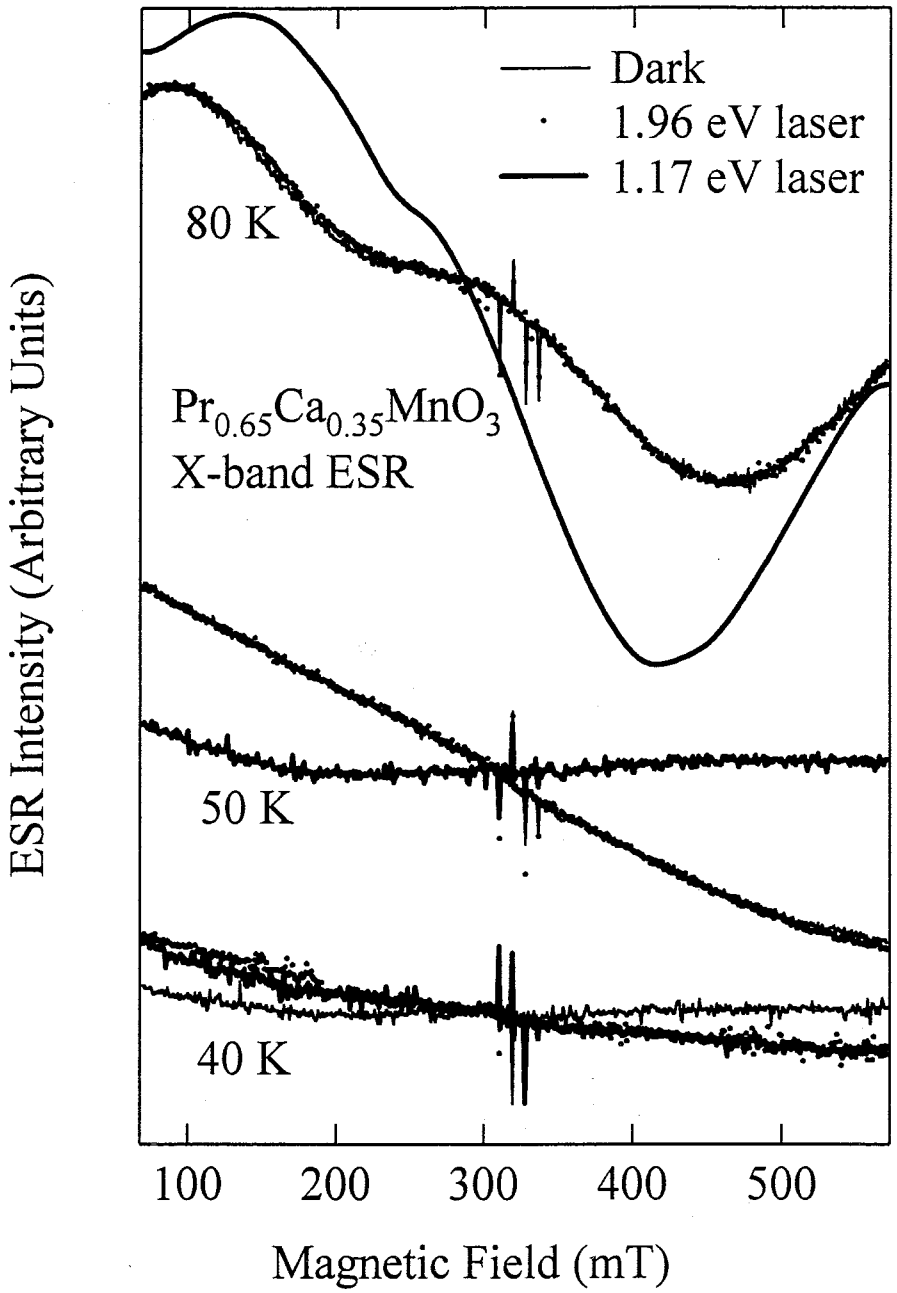
Dark
1.96 eV laser
1.17 eV laser
80 K
$Pr_{0.65}Ca_{0.35}MnO_3$
X-band ESR
50 K
40 K
ESR Intensity (Arbitrary Units)
100
200
300
400
500
Magnetic Field (mT)

Figure III - 3

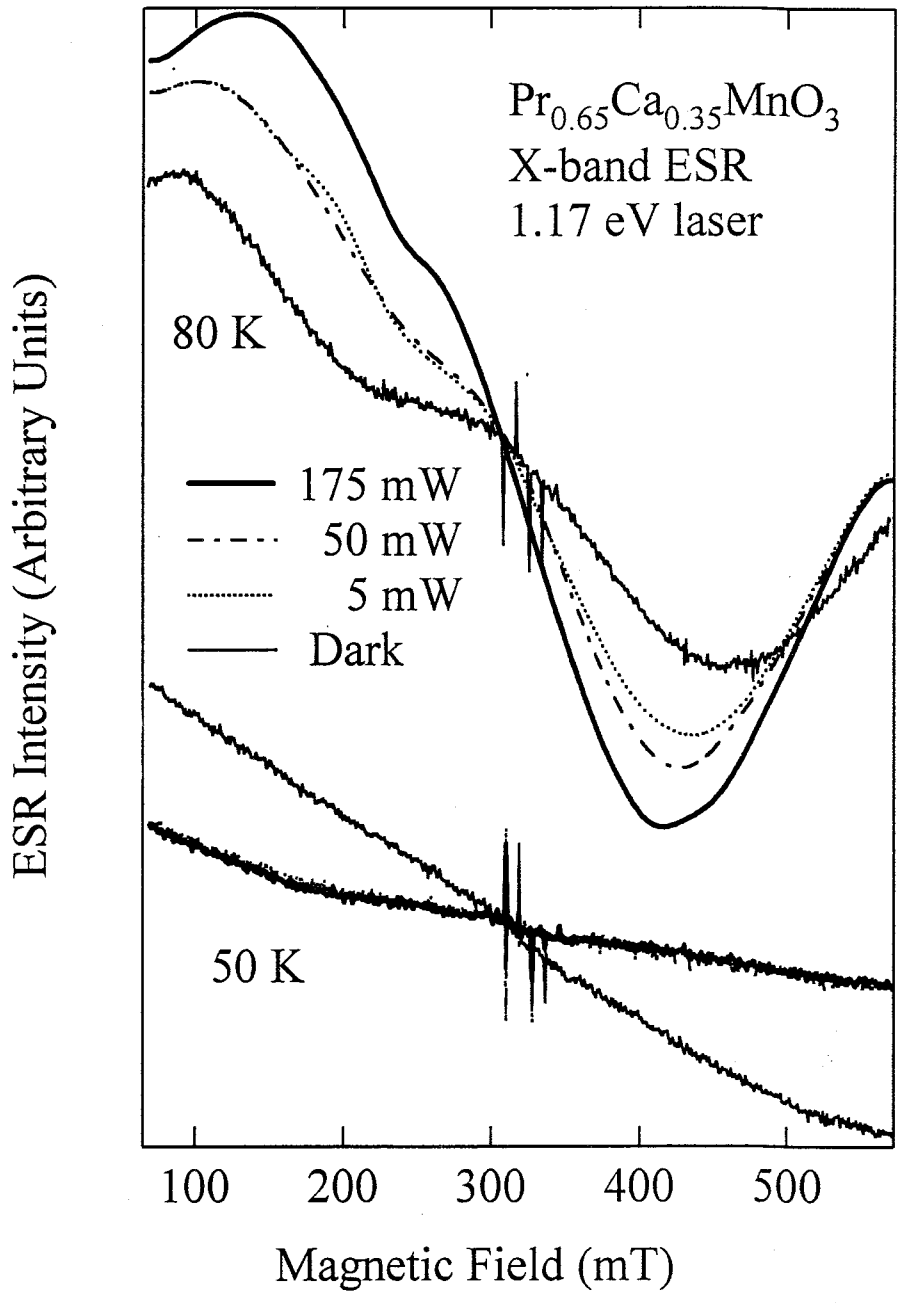
$Pr_{0.65}Ca_{0.35}MnO_3$
X-band ESR
1.17 eV laser
80 K
175 mW
50 mW
5 mW
Dark
50 K
ESR Intensity (Arbitrary Units)
100
200
300
400
500
Magnetic Field (mT)

Figure III - 4

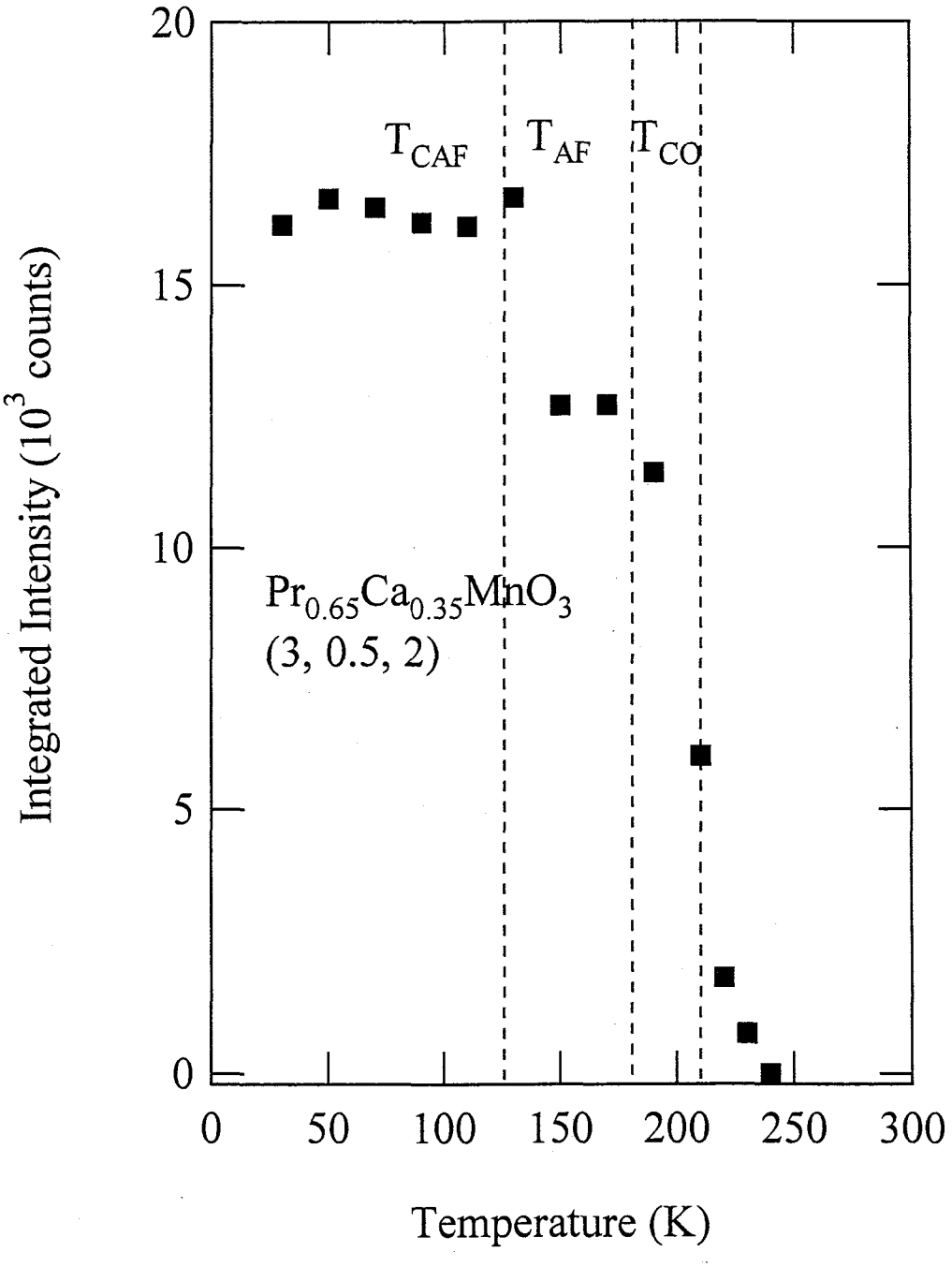
20
15
10
5
0
0
50
100
150
200
250
300
T_{CAF}
T_{AF}
T_{CO}
$Pr_{0.65}Ca_{0.35}MnO_3$
(3, 0.5, 2)
Integrated Intensity (10^3 counts)
Temperature (K)

Figure IV - 1

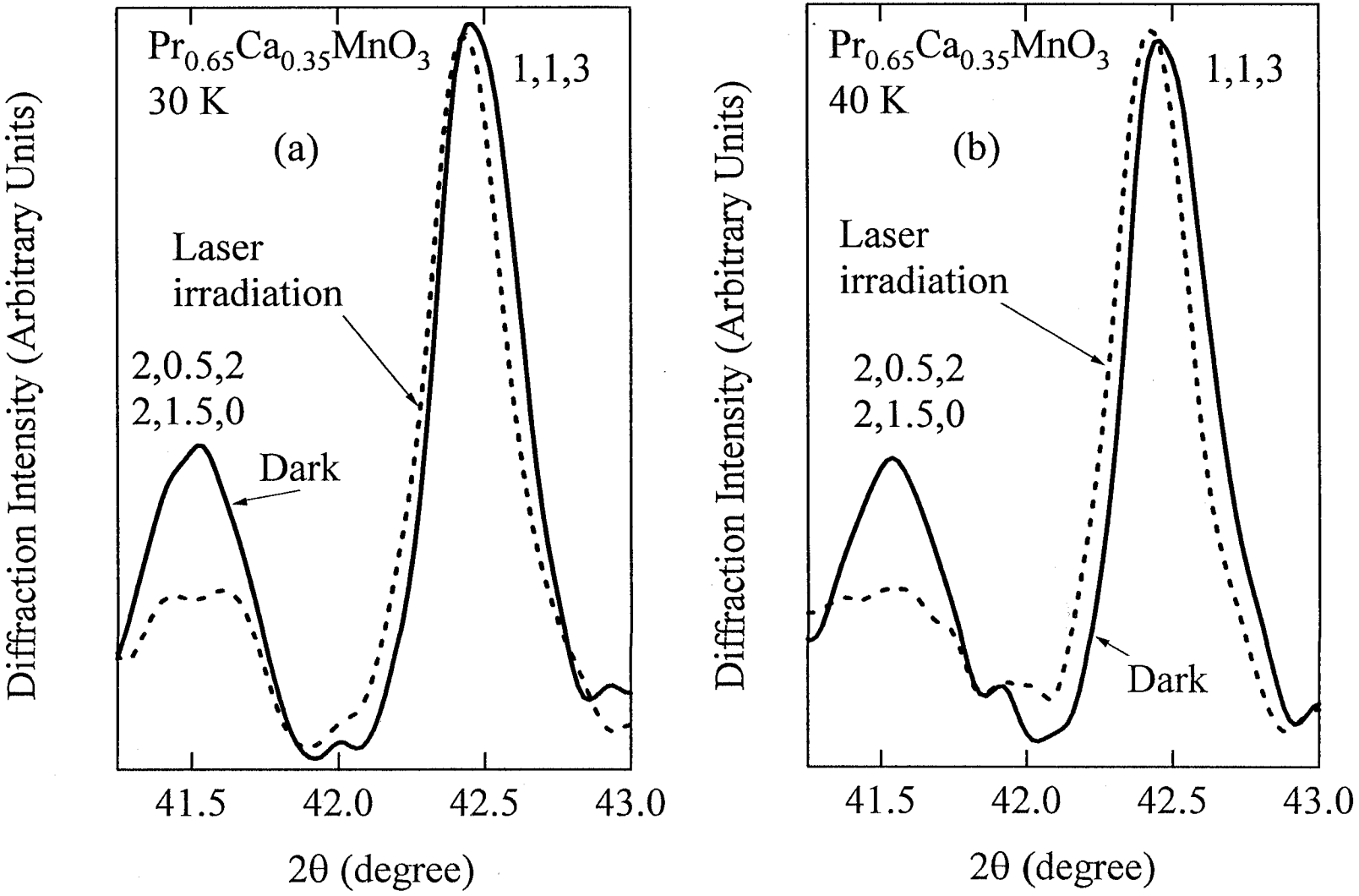
Pr0.65Ca0.35MnO3
30 K
(a)
1,1,3
Laser
irradiation
2,0.5,2
2,1.5,0
Dark
Diffraction Intensity (Arbitrary Units)
41.5
42.0
42.5
43.0
2θ (degree)
Pr0.65Ca0.35MnO3
40 K
(b)
1,1,3
Laser
irradiation
2,0.5,2
2,1.5,0
Dark
Diffraction Intensity (Arbitrary Units)
41.5
42.0
42.5
43.0
2θ (degree)

Figure IV - 2

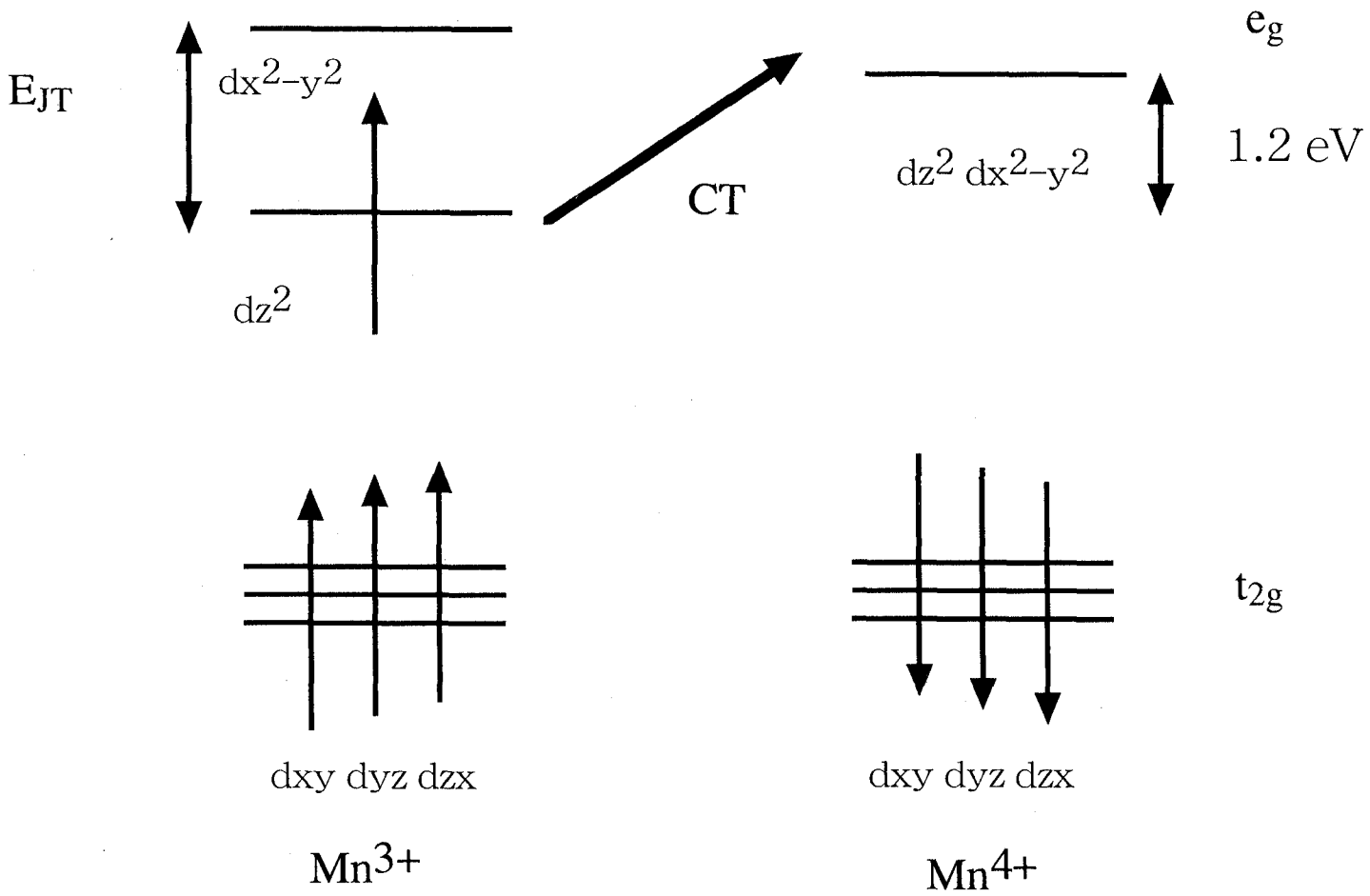
E_{JT}
dx^{2-y^2}
dz^2
CT
e_g
dz^2 dx^{2-y^2}
1.2 eV
t_{2g}
dxy dyz dzx
dxy dyz dzx
Mn^{3+}
Mn^{4+}

Figure IV - 3

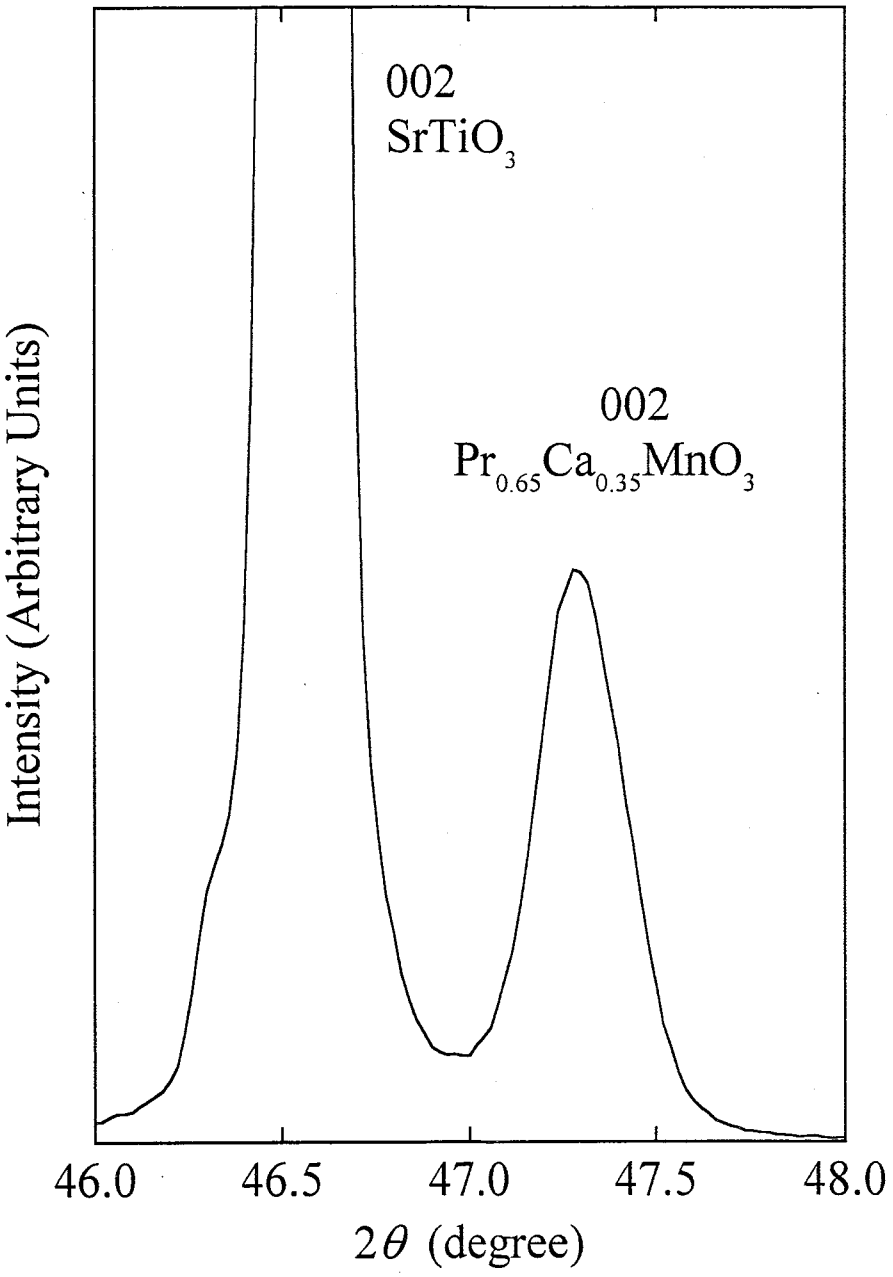
002
SrTiO3
002
Pr0.65Ca0.35MnO3
Intensity (Arbitrary Units)
46.0
46.5
47.0
47.5
48.0
2θ (degree)

Figure V - 1

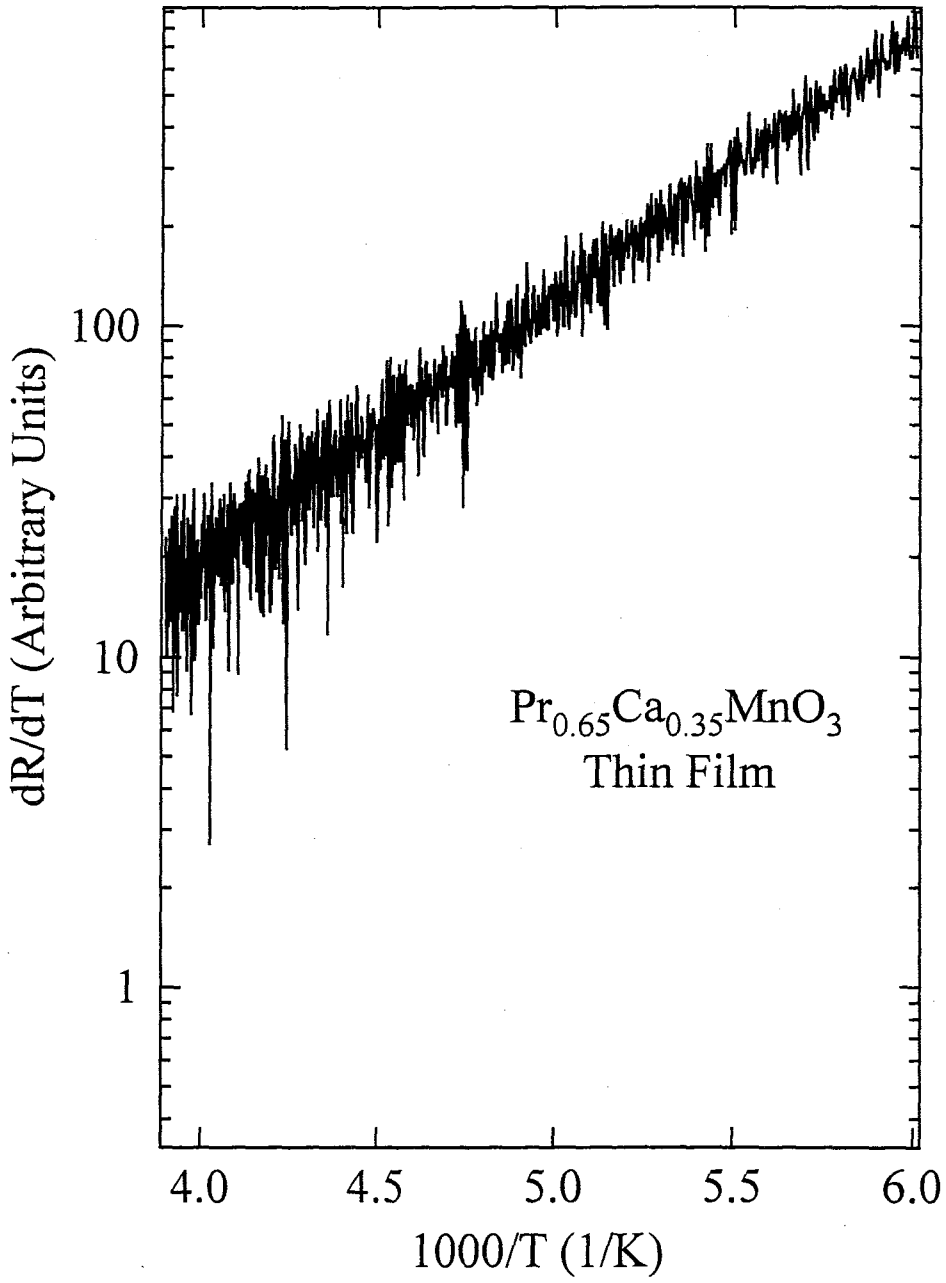
dR/dT (Arbitrary Units)
100
10
1
$Pr_{0.65}Ca_{0.35}MnO_3$
Thin Film
4.0
4.5
5.0
5.5
6.0
1000/T (1/K)

Figure V - 2

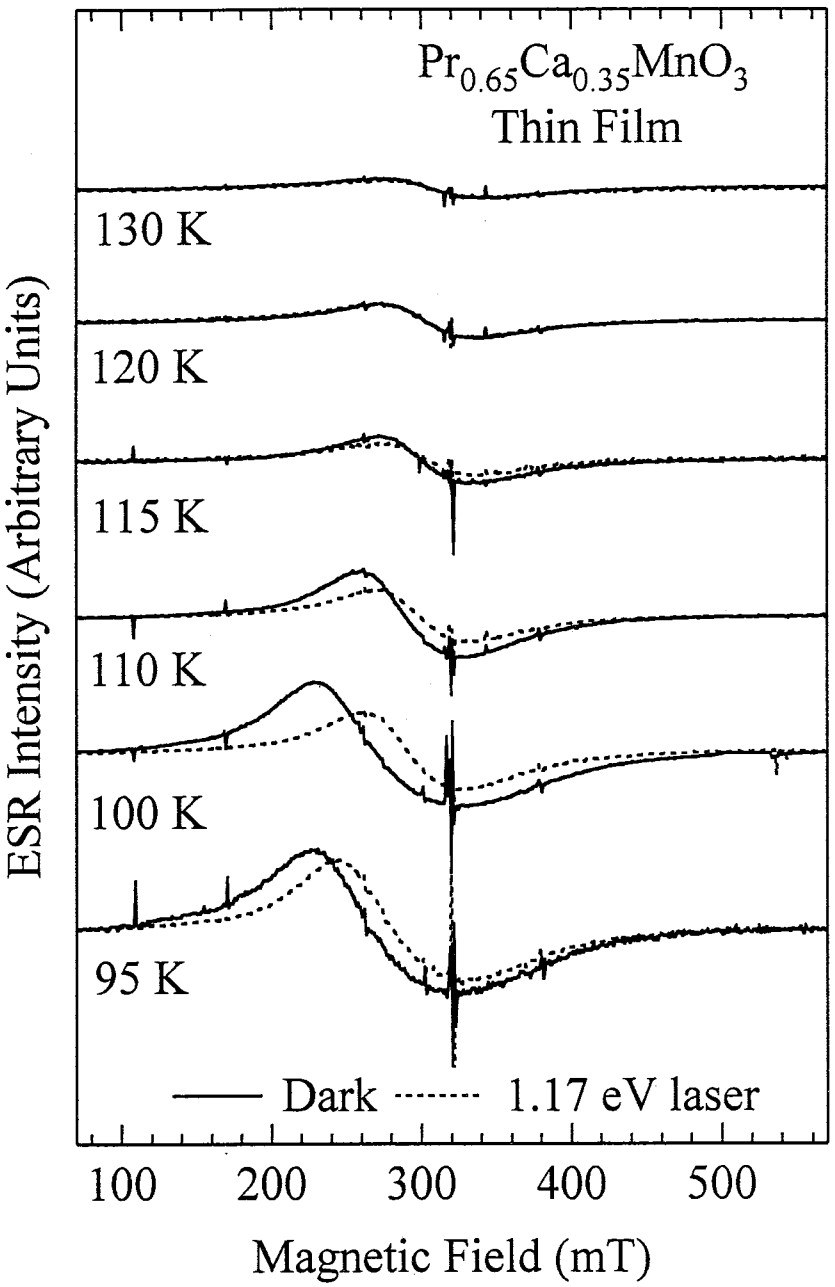
$Pr_{0.65}Ca_{0.35}MnO_3$
Thin Film
130 K
120 K
115 K
110 K
100 K
95 K
Dark
1.17 eV laser
ESR Intensity (Arbitrary Units)
100
200
300
400
500
Magnetic Field (mT)

Figure V - 3

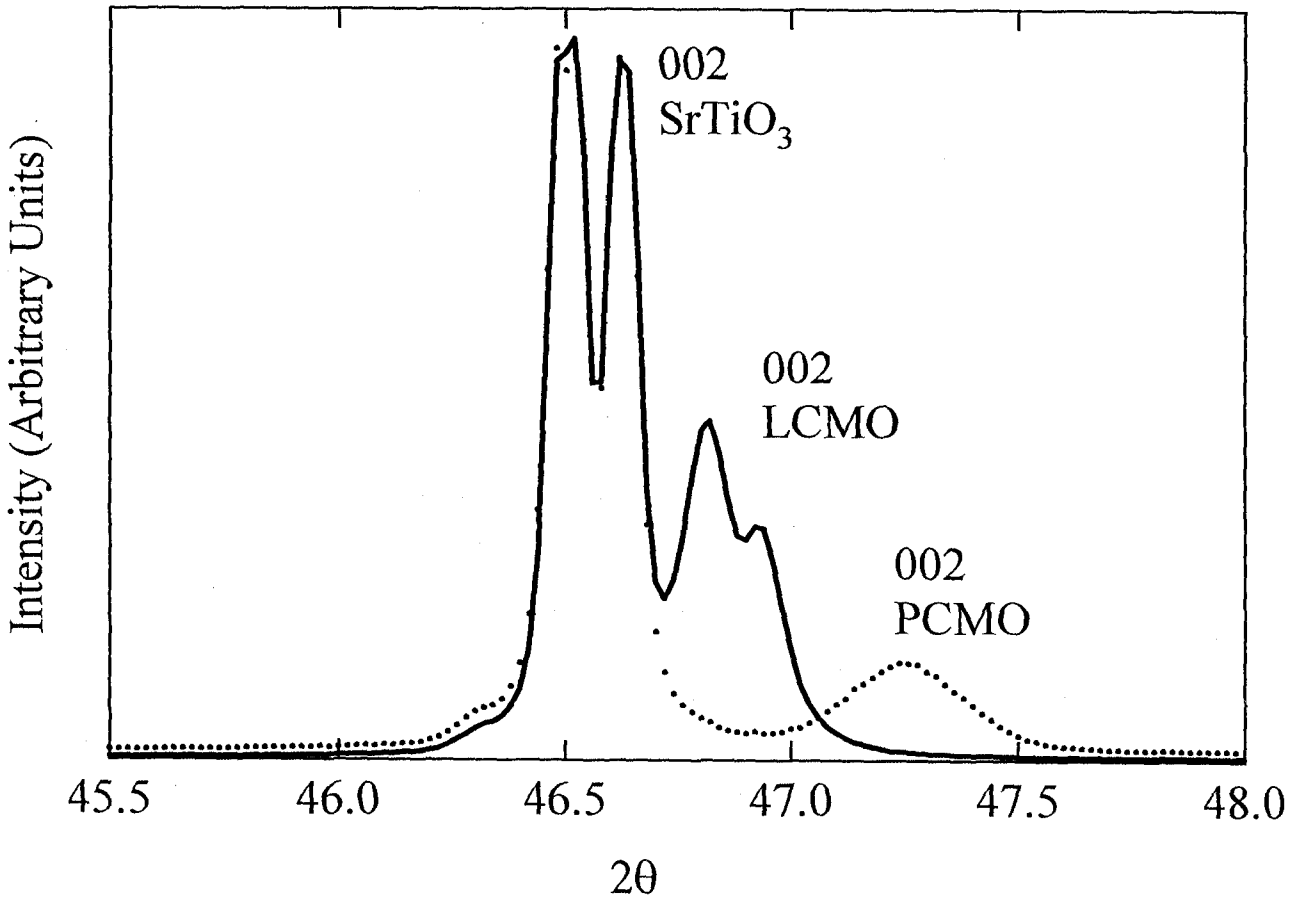
Intensity (Arbitrary Units)
002
SrTiO3
002
LCMO
002
PCMO
45.5
46.0
46.5
47.0
47.5
48.0
2θ

Figure VI - 1

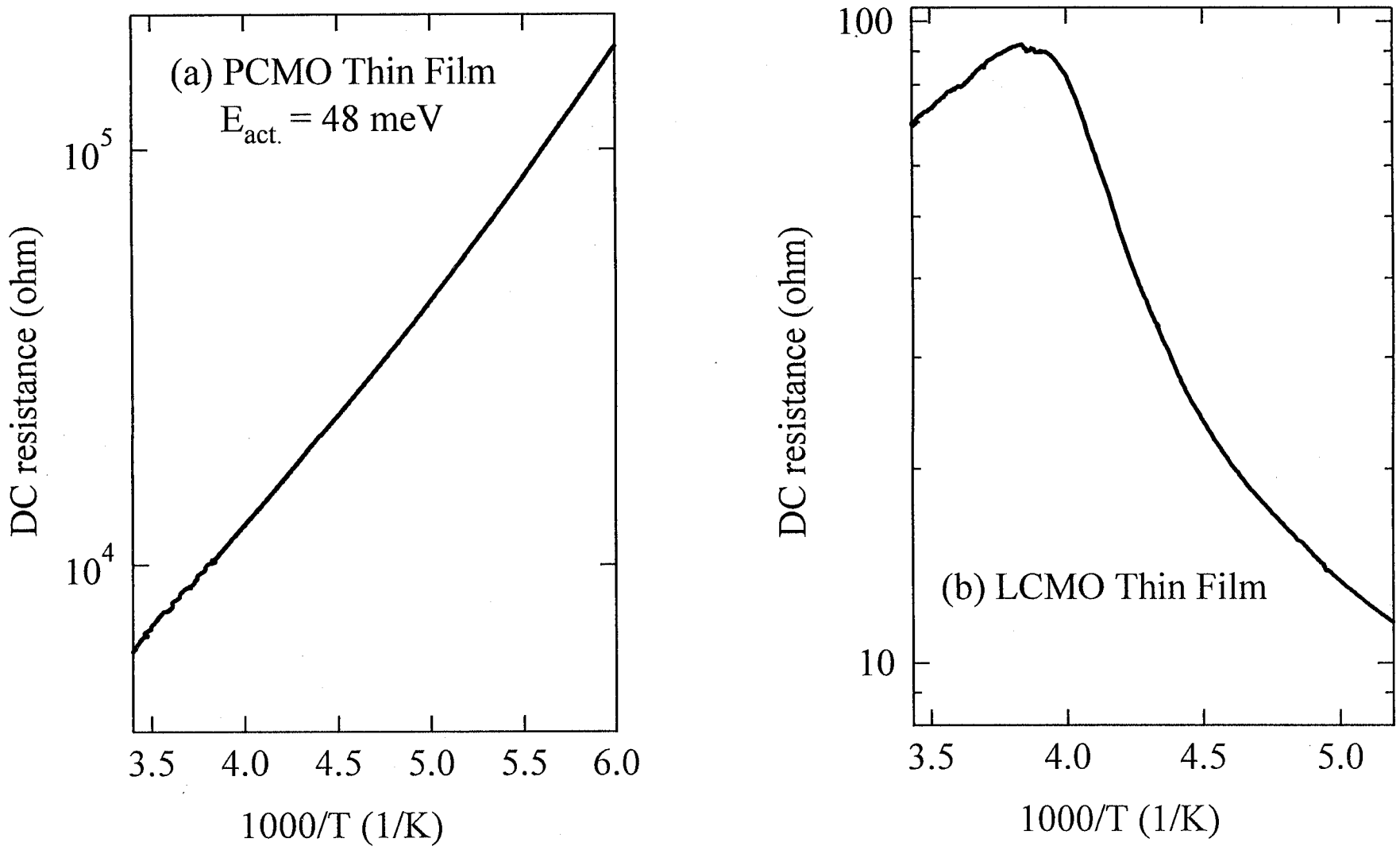
(a) PCMO Thin Film
$E_{act.}$ = 48 meV
10^5
10^4
DC resistance (ohm)
3.5
4.0
4.5
5.0
5.5
6.0
1000/T (1/K)
100
10
DC resistance (ohm)
(b) LCMO Thin Film
3.5
4.0
4.5
5.0
1000/T (1/K)

Figure VI - 2

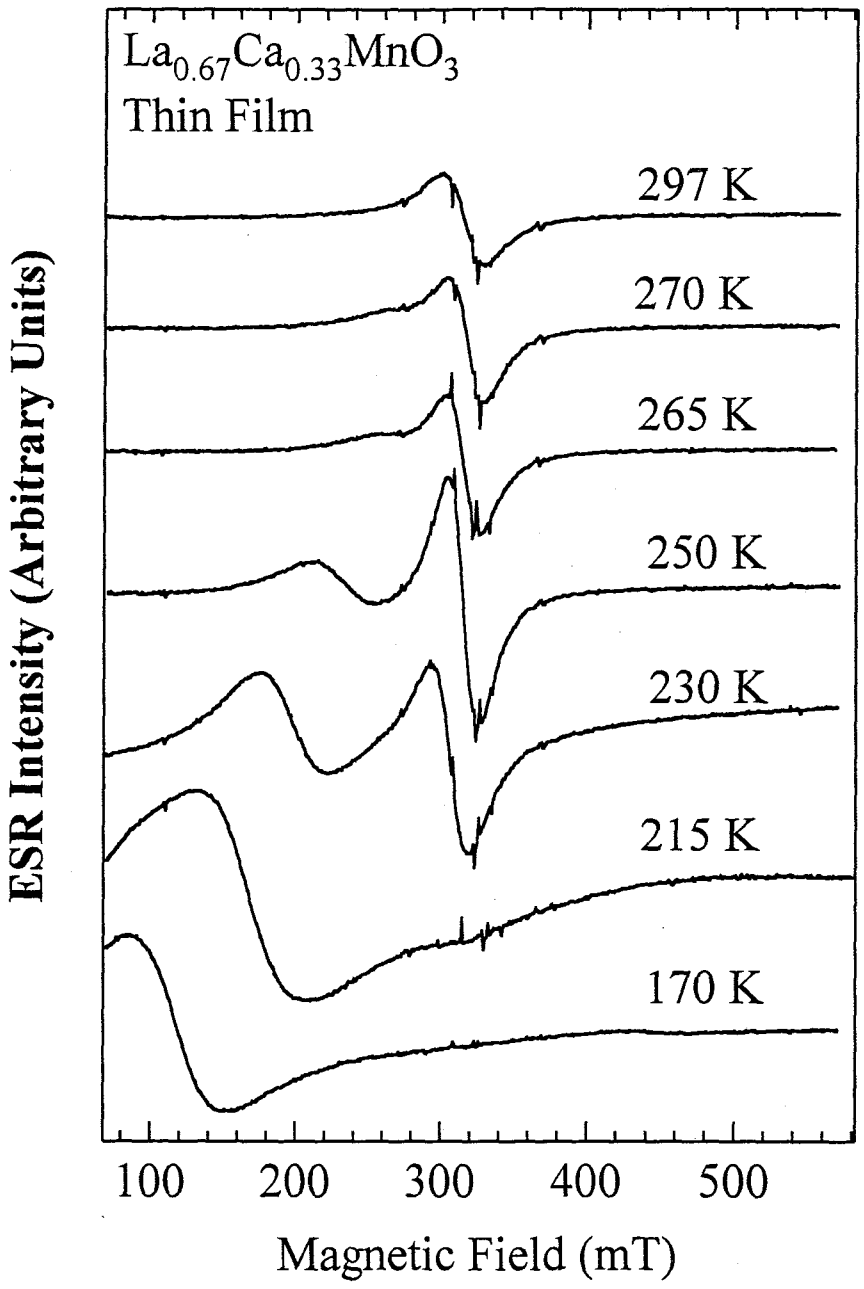
La0.67Ca0.33MnO3
Thin Film
297 K
270 K
265 K
250 K
230 K
215 K
170 K
ESR Intensity (Arbitrary Units)
100
200
300
400
500
Magnetic Field (mT)

Figure VI - 3

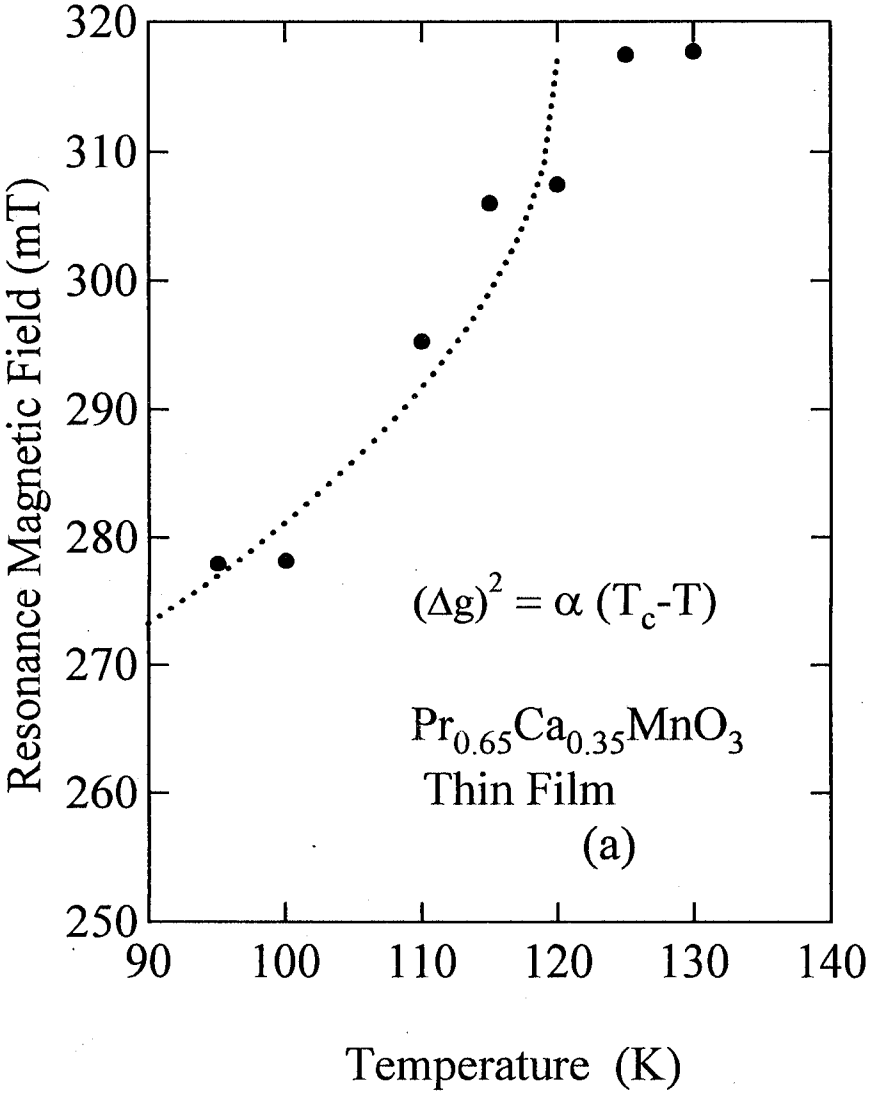
320
310
300
290
280
270
260
250
90
100
110
120
130
140
Resonance Magnetic Field (mT)
Temperature (K)
$(\Delta g)^2 = \alpha (T_c - T)$
$Pr_{0.65}Ca_{0.35}MnO_3$
Thin Film
(a)

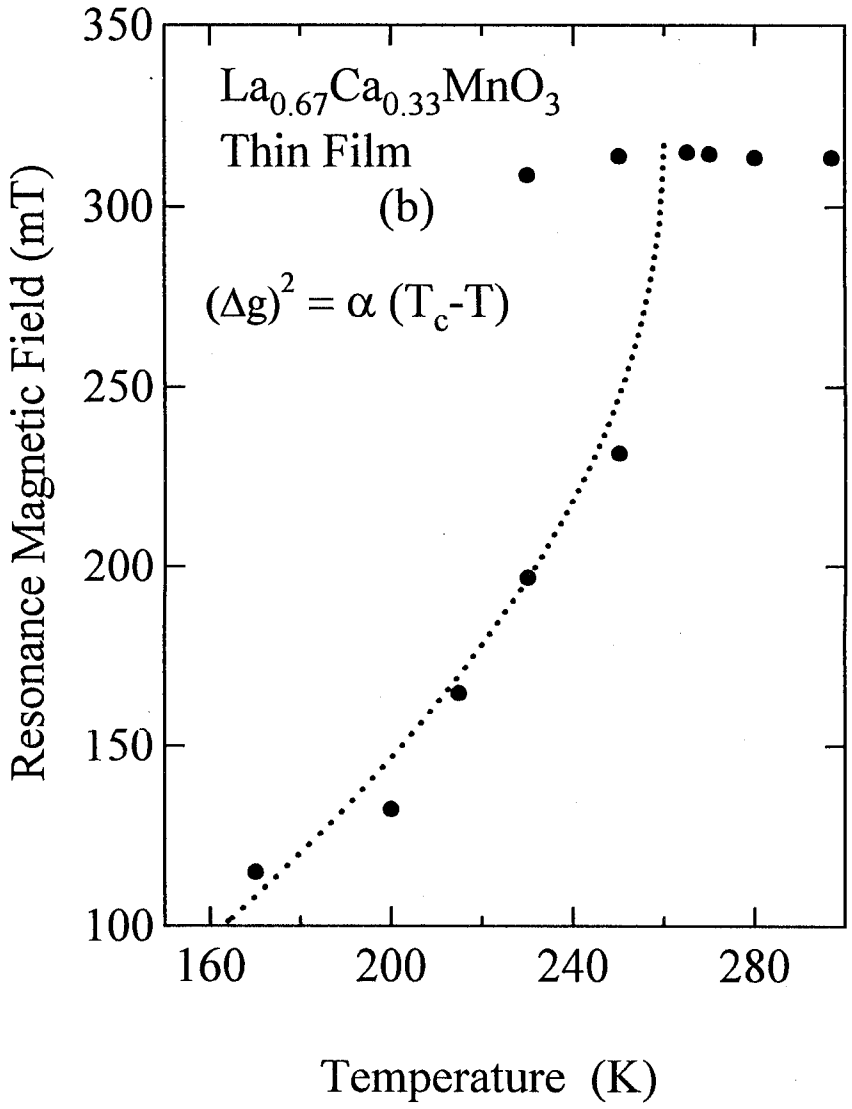
350
300
250
200
150
100
160
200
240
280
Resonance Magnetic Field (mT)
Temperature (K)
$La_{0.67}Ca_{0.33}MnO_3$
Thin Film
(b)
$(\Delta g)^2 = \alpha (T_c - T)$

Figure VI - 4

List of Publication

1 Electron Spin Resonance in $Pr_{0.65}Ca_{0.35}MnO_3$.

Osami YANAGISAWA, Mitsuru IZUMI, Wei-Zhi Hu, Kenji NAKANISHI, and Hideo NOJIMA

J. of Superconductivity, Vol.12, No.1, 1999, pp.307-310

2 The Photo-Induced Effect of the Electron Spin Resonance on the Charge-Ordered State in$Pr_{0.65}Ca_{0.35}MnO_3$

Osami YANAGISAWA, Mitsuru IZUMI, Wei-Zhi Hu, Kenji NAKANISHI, and Hideo NOJIMA

J. of Superconductivity, Vol.12, No.1, 1999, pp.311-315

3 Evidence of Photo-Induced Melting of the Charge-ordered State in $Pr_{0.65}Ca_{0.35}MnO_3$ by X-ray Diffraction.

Osami YANAGISAWA, Mitsuru IZUMI, Wei-Zhi Hu, Kai-hua Huang, Kenji Nakanishi, and Hideo Nojima

Physica B, Vol. 271, 1999, pp. 235-241

4 The Photo-Induced Effect on the Charge-Ordered State with Canted Antiferromagnetic Spin Order in $Pr_{0.65}Ca_{0.35}MnO_3$

Osami YANAGISAWA, Mitsuru IZUMI, Wei-Zhi Hu, Kai-hua Huang, Kenji Nakanishi, and Hideo Nojima

NATO Science Series, 3. High Technology, Vol. 72, pp. 263-268, 1999

5 Comparative Study of Photo-Induced Effect on the Charge-Ordered State of $Pr_{0.65}Ca_{0.35}MnO_3$ in Powder Form and Thin Films

Osami YANAGISAWA, Mitsuru IZUMI, Kai-hua Huang, Wei-Zhi Hu, Yi Shen, Kenji Nakanishi, Yoshihiro Takahashi and Hideo Nojima

Accepted to J. of Magnetism and Magnetic Material at Jun. 1, 1999

6 Magnetic Transition in Thin-Films of $La_{0.6}Ca_{0.35}MnO_3$ and $Pr_{0.65}Ca_{0.35}MnO_3$

Osami YANAGISAWA, Mitsuru IZUMI, Kai-hua Huang, Wei-Zhi Hu, Yi Shen, Kenji Nakanishi, Yoshihiro Takahashi and Hideo Nojima

Accepted to J. of Magnetism and Magnetic Material at Jun. 1, 1999

Journal of Superconductivity, Vol. 12, No. 1, 1999

Electron Spin Resonance in $Pr_{0.65}Ca_{0.35}MnO_3$

Osami Yanagisawa,[1] Mitsuru Izumi,[1] Wei-Zhi Hu,[1] Kenji Nakanishi,[2] and Hideo Nojima[2]

The magnetic behavior of the distorted perovskite manganese, $Pr_{0.65}Ca_{0.35}MnO_3$ was studied by X-band electron spin resonance for powder samples. We observed the onset of the charge-ordered state at $T_{CO} \sim 215$ K, the antiferromagnetic transition with the peak of the ESR linewidth, ΔH_{p-p} at $T_{AF} \sim 180$ K and the canted antiferromagnetic transition at $T_{CAF} \sim 125$ K associated with the abrupt increase of both the effective magnetization and ΔH_{p-p}. Below 90 K, the absorption intensity profile becomes weakened with decreasing temperature suggesting the existence of some kind of magnetic disorder below 90 K, which is responsible for a part of evidence of the existence of the spin-glass state as has been proposed by Yoshizawa *et al., Phys. Rev. B* **52**, 1689 (1996).

KEY WORDS: Magnetic materials; oxides; phase transitions; colossal magnetoresistance; electron paramagnetic resonance; spin glass.

1. INTRODUCTION

The distorted perovskite manganese, $Pr_{1-x}Ca_xMnO_3$ has attracted much interest, since the large negative magnetoresistance so called colossal magnetoresistance (CMR) has been detected, where the electron spins on Mn^{3+} and Mn^{4+} ionic sites play an important role [1–4]. Mn^{3+} ion in the hole nondoped compound $PrMnO_3$ and Mn^{4+} ion in the hole doped compound $CaMnO_3$ have high spin $3d^4$ electron configuration $t_{2g}^3 e_g^1$ and low spin $3d^3$ electron configuration t_{2g}^3, respectively. Hund's rule makes all spins align with each other on the atomic site by a large intra-atomic exchange. The t_{2g} orbitals (localized spin $S = 3/2$) hybridize with O_{2p} orbitals much more weakly than the e_g orbitals. The e_g orbitals have lobes directed to the counter oxygen atoms and hybridize strongly with O_{2g} orbitals, leading to the creation of rather broad bands. The electronic conduction is achieved via hopping of an electron from Mn^{3+} to Mn^{4+} with the electron transfer energy t. This conducts in the ferromagnetic (F) double exchange interaction between the localized spins, the core t_{2g} orbital ($S = 3/2$) mediated by the hopping e_g orbital electron [5,6]. In these manganites, the electronic bandwidth is controlled as a function of transfer energy suffered by the lattice distortion. The smaller ionic radii of the (Pr, Ca) site ions form the smaller transfer integral which leads to the carrier localization in association with the formation of the charge ordered state (CO) rather than delocalization of the charge through the double-exchange mechanism [5,6].

$Pr_{1-x}Ca_xMnO_3$ remains insulating against doping carriers over the whole temperature, which is semiconductor [3,4,7,8]. The charge-ordering appears at higher temperature than the magnetic transition temperature. It is worth noting that the CO state is stabilized over a wide range of concentration, around $0.3 < x < 0.7$ in the $Pr_{1-x}Ca_xMnO_3$ system [3,4,9,10].

The charge-ordering phenomenon has been mostly observed when the concentration of charge carriers takes a rational value of the periodicity of the crystal lattice. The commensurability of the carrier concentration with a periodicity of the crystal lattice is related to the stability of the CO state, because of the correlation strength among the charge carriers. The CO state is optimized at $x = 0.5$ (commensurate), a deviation of x from 0.5 (discommensurate) decreases the stability of the CO state. Around $x = 0.3$, the system is on the phase boundary of the transition from the CO insulator (COI) to the ferromagnetic metal (FM), so that the external stimuli

[1]Laboratory of Applied Physics, Tokyo University of Mercantile Marine, 2-1-6, Etchu-jima, Koto-ku, Tokyo 135-8533, Japan.
[2]Functional Devices Research Laboratory, Sharp Corporation, 273-1 Kashiwa, Kashiwa-shi, Chiba 277-0005, Japan.

0896-1107/99/0200-0307$16.00/0

(magnetic field, photocarrier injection, etc.) may cause the transition from the COI to the FM phase with relative ease [3,4,11–13].

In $Pr_{1-x}Ca_xMnO_3$ ($x = 0.3$), the MR is most pronounced below 80 K. From the neutron diffraction study, the spin glass state is suggested by Yoshizawa *et al.* [3].

In this paper, we study $Pr_{1-x}Ca_xMnO_3$ ($x = 0.35$) in which the averaged ionic valency is 3.35 per Mn ion, leading to the occurrence of discommensuration in CO phase with a specific interest in the competition between CO and FM order under external stimulii. A magnetic behavior in $Pr_{0.65}Ca_{0.35}MnO_3$ was studied with focusing electron spin state of $3d-t_{2g}$ and/or $3d-e_g$ on Mn^{3+} and Mn^{4+} ionic sites with the X-band electron spin resonance (ESR) leading to the complemental evidence of the prescribed spin-glass state as a result of competing interaction between AF and FM states.

2. EXPERIMENT

The powder samples of $Pr_{0.65}Ca_{0.35}MnO_3$ were prepared by conventional ceramic technique [3]. The X-ray analysis indicated that the sample was in single phase with symmetry is orthorhombic, the space group *Pbnm* with lattice constants $a = 5.428$ Å, $b = 5.455$ Å, and $c = 7.663$ Å at 290 K. Below 215 K, the superlattice reflections appeared as an evidence of the formation of the CO state [14,15].

The ESR measurement for the electron spins on Mn^{3+} and Mn^{4+} ionic sites in $Pr_{0.65}Ca_{0.35}MnO_3$ was done using X-band spectrometer (JEOL-RE1X) with 100 kHz field modulation. The amount of the powder sample was 0.5 mg. The sample was mounted in a liquid He continuous-flow type cryostat and was cooled from 300 K down to 10 K. The resonance absorption of the ESR measurement were observed as deviative signal curves, was fitted to a Lorentzian and the resultant curves were made. The ESR linewidth ΔH_{p-p}, which one evaluate the spin–spin interaction through the spin–spin relaxation time, were taken from the half-amplitude linewidth of integrate to these curves. The effective spin susceptibility χ_{eff} was taken from successive integration of the obtained profile with references to both $CuSO_4 \cdot 5H_2O$ whose spin susceptibility is known and Mn^{2+} ions diluted with MgO.

We measured the dc magnetization under the magnetic field 0.01 T by SQUID susceptometer in the warming run after field cooling run (FC(W)), the cooling run after field cooling run (FC(C)) and the zero field cooling run (ZFC). In the zero field cooling run (ZFC), measurements were performed after sample was cooled down to a prescribed temperature under zero field, then a field was raised to 0.01 T.

3. RESULTS AND DISCUSSION

In $Pr_{0.65}Ca_{0.35}MnO_3$, the observed ESR profiles clearly show Lorentzian shape above 80 K. Figure 1 shows the temperature dependence of the ESR linewidth ΔH_{p-p} (●) and the effective spin susceptibility χ_{eff} (▲). The effective spin susceptibility χ_{eff} increases up to $T_{CO} \sim 215$ K with decreasing temperature which shows the paramagnetic behavior, then decreases down to $T_{CAF} \sim 125$ K which can be interpreted that the AF ordering starts to form before the second-order AF transition, and finally shows a spontaneous magnetization below T_{CAF}, which indicates the appearance of the ferromagnetic component [3] associated with the abrupt increase of ΔH_{p-p}. There is a cusp structure near $T_{AF} \sim 180$ K which corresponds to the AF transition. The ESR linewidth ΔH_{p-p} decreases linearly with decreasing temperature leading to the paramagnetic character. Below $T_{CO} \sim 215$ K, the ΔH_{p-p} exhibits a peak around 180 K suggesting the formation of AF order, and finally

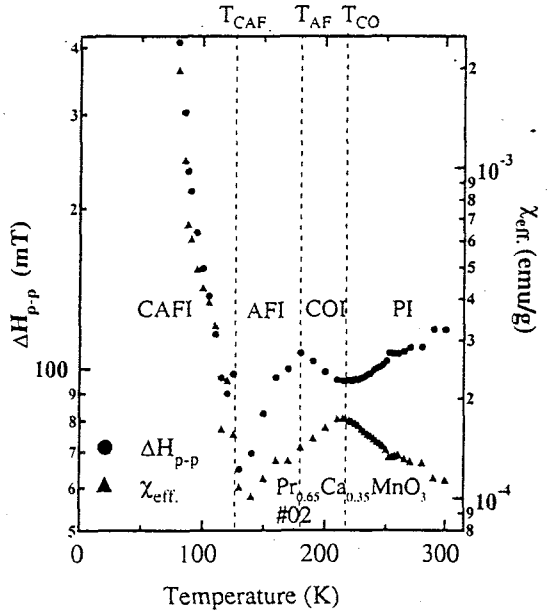

Fig. 1. Temperature dependence of the electron-spin resonance linewidth ΔH_{p-p} (●) and the effective spin susceptibility χ_{eff} (▲) for $Pr_{0.65}Ca_{0.35}MnO_3$ from 300 K down to 10 K. The PI, COI, AFI, and CAFI denote the paramagnetic insulator, charge-ordered insulator, antiferromagnetic insulator, and canted antiferromagnetic insulator, respectively. T_{CO}, T_{AF}, and T_{CAF} denote charge-ordering transition temperature, Néel temperature, canted antiferromagnetic transition temperature, respectively.

increases abruptly below $T_{CAF} \sim 125$ K which shows that the ferromagnetic exchange interaction increases with decreasing temperature. We assign T_{AF} as ~180 K from the existence of the peak in the ESR linewidth ΔH_{p-p} as a function of temperature. T_{AF} has been a difficulty to determine in the magnetization measurement so far. The ferromagnetic moment was determined to be $\mu_F \sim 1.9 \pm 0.2\,\mu_B$/Mn at 5 K from the integrated intensity of the neutron diffraction profiles by Yoshizawa *et al.* [3]. Yoshizawa *et al.* [3] have also determined the AF moment to be $\mu_{AF1} \sim 1.4 \pm 0.2\,\mu_B$/Mn for Mn^{3+} ion site and $\mu_{AF1} < 0.5\,\mu_B$/Mn for Mn^{4+} ion site, respectively. In our present study, the magnetic moment was calculated to be $\mu_F \sim 0.83\,\mu_B$/Mn as a part of the antiferromagnetic moment from the effective spin susceptibility χ_{eff}. The obtained value is about a half of the sum of total AF moment. Besides, Shengelaya *et al.* [16] indicated that the Mn^{3+} ($3d^4$ with S = 2) is unlikely to have an observable ESR due to the existence of a large zero-field splitting and spin-lattice relaxation. The detailed analysis and the precise characterization under the AF resonance scheme is open for the further study.

Figures 2a and 2b exhibit the ESR profiles at the low temperature region between 105 K and 75 K. The solid lines show the observed ESR profiles. Fitting to a Lorentzian curve was made and the resultant curves are drawn with dotted lines. Below 90 K, there are remarkable changes in the observed ESR profiles which are away from the Lorentzian shape together with the decomposition of the unique resonance curves and the resonance field seems to shift to the lower magnetic field. It seems that there are at least two absorption lines these superpose with each other, which shows the existence of a couple of modes as the result of disorder in the antiferromagnetic order below 180 K.

The dc magnetization under the magnetic field 0.01 T in the warming run after field cooling run (FC(W)), the cooling run after field cooling run (FC(C)) and the warming run after zero field cooling (ZFC), respectively. A spontaneous magnetization appears below $T_{CAF} \sim 115$ K. As shown in Fig. 3, the irreversible hysteresis between the FC(W) and ZFC grows remarkably $T_{CAF} \sim 125$ K with a decrease in temperature, especially below 115 K. The present observation is a typical magnetic behavior for a spin-glass state as prescribed above [4]. In $Pr_{0.65}Ca_{0.35}MnO_3$, the concentration, x of Mn^{3+} ions does not retain a commensurate such as $x = 1/4$, $1/3$, and $1/2$. The observed magnetic structure in the orthorhombic ab plane is that of the commensurate value

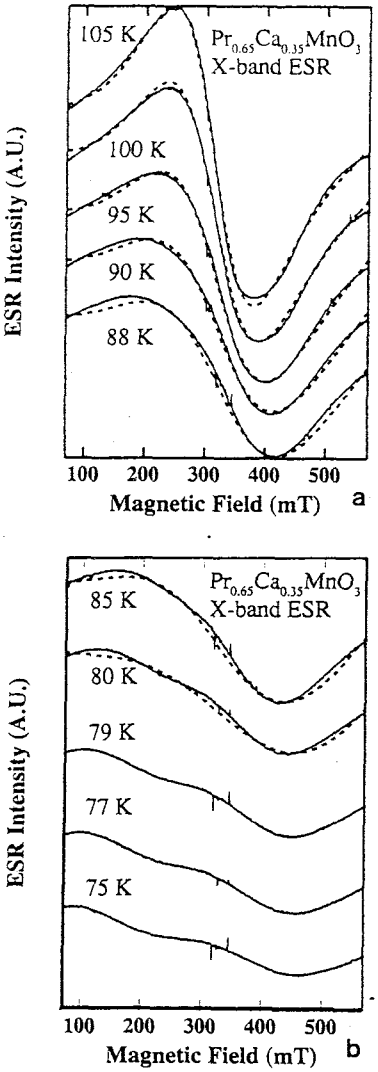

Fig. 2. The electron spin resonance profiles for $Pr_{0.65}Ca_{0.35}MnO_3$ at temperature range between 105 K and 88 K (a) and 85 K and 75 K (b). The ESR profiles clearly show Lorentzian shape above 80 K as exhibited in the Lorentzian curves fitted (dotted curves).

$x = 1/2$ structure as reported in an early study [9,10]. Thus, the formation of charge-ordering (CO) after CE-type configuration makes excess Mn^{3+} ions intersperse randomly over Mn^{4+} ion sites. Then the onset of some kind of frustrated exchange interaction leads to the spin glass like behavior at the low temperature as detected by the present ESR profiles.

4. CONCLUDING REMARKS

Unusual magnetic behavior of the distorted perovskite manganese, $Pr_{0.65}Ca_{0.35}MnO_3$ was studied by X-band ESR for powder samples. We observed the onset of the charge-ordered state at $T_{CO} \sim 215$ K, the

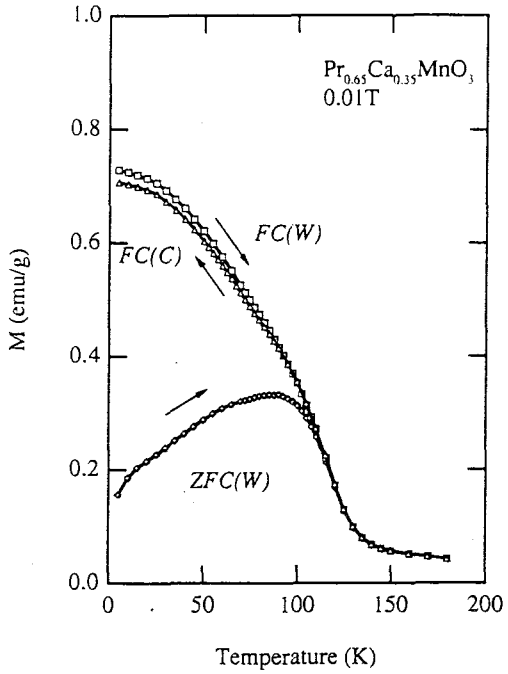

Fig. 3. DC magnetization as a function of temperature in $Pr_{0.65}Ca_{0.35}MnO_3$. FC(C), FC(W) and ZFC denote, which are the magnetization in the cooling run after field cooling run, the warming run after field cooling run, and the warming run after zero field cooling, respectively. Measurements have been done under the magnetic field 0.01 T. In the zero field cooling (ZFC), measurements were performed after sample was cooled to a prescribed temperature under zero field.

antiferromagnetic transition with the peak of the ESR linewidth, ΔH_{p-p} at $T_{AF} \sim 180$ K and the canted antiferromagnetic transition at $T_{CAF} \sim 125$ K associated with the abrupt increase of both the effective magnetization and ΔH_{p-p} as a trace of the ferromagnetic behavior. Below 90 K, the absorption intensity profile becomes anomalously weakened with decreasing temperature suggesting the existence of some kind of magnetic disorder, which is responsible for a part of evidence of the existence of the spin-glass state as has been proposed by Yoshizawa *et al.*, *Phys. Rev. B* **52**, 1689 (1996).

ACKNOWLEDGMENTS

We would like to thank Dr. R. Tamura (SRL-ISTEC) for the dc magnetization measurement and Dr. N. Tsuchimine (Toshima Mfgs Co., Ltd.) for sample preparation.

REFERENCES

1. H. Chiba, M. Kikuch, K. Kusaba, Y. Muraoka, and Y. Syono, *Solid State Commun.* **99**, 499 (1996).
2. S. Jin, T. H. Tiefel, M. McCormack, R. A. Fastnacht, R. Ramesh, and L. H. Chen, *Science* **264**, 413 (1994).
3. H. Yoshizawa, H. Kawano, Y. Tomioka, and Y. Tokura, *Phys. Rev. B* **52**, 1689 (1996).
4. Y. Tomioka, A. Asamitsu, H. Kuwahara, and Y. Moritomo, *Phys. Rev. B* **53**, 1689 (1996).
5. C. Zener, *Phys. Rev.* **82**, 403 (1951).
6. J. B. Goodenough, *Phys. Rev.* **100**, 564 (1955).
7. V. I. Anisimov, I. S. Elfimov, M. A. Korotin, and K. Terakura, *Phys. Rev. B* **55**, 15494 (1997).
8. H. Y. Hwang, P. Dai, S.-W. Cheong, G. Aeppli, D. A. Tennant, and H. A. Mook, *Phys. Rev. Lett.* **53**, 1316 (1998).
9. Z. Jirak, S. Krupicka, Z. Simsa, M. Dlouha, and Z. Vratislav, *J. Mag. Mag. Mat.* **15–18**, 519 (1980).
10. Z. Jirak, S. Krupicka, Z. Simsa, M. Dlouha, and Z. Vratislav, *J. Mag. Mag. Mat.* **53**, 153 (1985).
11. K. Miyano, T. Tanaka, Y. Tomioka, and Y. Tokura, *Phys. Rev. Lett.* **78**, 4257 (1997).
12. A. Asamitsu, Y. Tomioka, H. Kuwahara, and Y. Tokura, *Nature* **388**, 50 (1997).
13. V. Kiryukhin, D. Casa, J. P. Hill, B. Keimer, A. Vigilante, Y. Tomioka, and Y. Tokura, *Nature* **386**, 813 (1997).
14. D. E. Cox, P. G. Radaeli, M. Marezio, and S.-W. Cheong, *Phys. Rev. B* **57**, 3305 (1998).
15. K. Nakanishi, S. Adachi, A. Tsukamoto, W.-Z. Hu, K. Tanabe, and M. Izumi, unpublished.
16. A. Shengelaya, Guo-meng Zhao, H. Keller, K. A. Müller, *Phys. Rev. Lett.* **77**, 5296 (1996).

Journal of Superconductivity, Vol. 12, No. 1, 1999

Photo-Induced Effect of the Electron-Spin Resonance on the Charge-Ordered State in $Pr_{0.65}Ca_{0.35}MnO_3$

Osami Yanagisawa,[1] Mitsuru Izumi,[1] Wei-Zhi Hu,[1] Kenji Nakanishi,[2] and Hideo Nojima[2]

Electron-spin resonance (ESR) for the charge-ordered state in well-characterized $Pr_{0.65}Ca_{0.35}MnO_3$ exhibited significant change of both the absorption profile and the effective spin susceptibility upon injection of laser light with photon energy of 1.17 eV provided by Nd-YAG laser. The increase of the effective spin susceptibility was clearly found out thanks to the injection of photons in the temperature range 90 K–80 K, which is below the transition temperature from the antiferromagnetic charge ordered state to the canted antiferromagnetic spin alternation state, $T_{CAF} \sim 125$ K. The temperature dependence of the change of the ESR profile excludes the possibility of heating by laser light. The present result suggests that a kind of photo-induced insulator–metal transition may occur due to propagation of the delocalized carriers via probable double exchange interaction in the charge-ordering collapsed state created by the injection of photons.

KEY WORDS: Magnetic materials; oxides; phase transitions; colossal magnetoresistance; electron paramagnetic resonance; spin glass.

1. INTRODUCTION

The distorted perovskite manganese $R_{1-x}A_xMnO_3$ (R = trivalent rare earth element and A = divalent alkaline earth element), one can control the electronic property through the electronic bandwidth and the doping level [1]. The electronic bandwidth control is able as a function of the transfer energy from the lattice distortion. The amount of the divalent ions, x, controls the level of doping. Upon partial substitution of R (trivalent ion) with A (divalent ion), a corresponding fraction x of Mn^{3+} is formally replaced with Mn^{4+} [1]. In some of these manganites magnetic field can drive the insulator–metal (I–M) transitions where the resistance and magnetization change dramatically, an effect termed colossal magnetoresistance (CMR) [2–5]. The amount of the divalent ions, x, control the level of doping.

The $R_{1-x}A_xMnO_3$ system is characterized by a strong competition between two different ground states: a charge-ordered (CO) insulating state, where the electric charges are localized and tend to order onto separate crystallographic sublattices, and a charge-delocalized (CD) state, with metallicity in dc conductivity. The magnetic and structural properties of these two states are quite different: the CO state is characterized as an antiferromagnetic (AF) arrangement of spins on Mn-ion sites, and the sublattice retains a cooperative Jahn–Teller (JT) distortion, thereby causing a fruitful combination of charge, orbital, and magnetic ordering. On the other hand, the CD state is in ferromagnetic (FM) spin arrangement, and displays relatively small JT distortions [6,7]. The ferromagnetic (F) properties themselves have been clarified in the context of the double-exchange interaction, originally proposed by Zener [8] and Goodenough [9,10].

The switching of dc resistivity between CO and CD states in the manganites can be achieved not only by a magnetic field, but also by an applied electric field. For the $Pr_{1-x}Ca_xMnO_3$, an electrical current implied by a static electric field triggers the antiferromagnetic insulator (AFI)–ferromagnetic metal (FM) transition at the low temperature [11]. In the

[1]Laboratory of Applied Physics, Tokyo University of Mercantile Marine, 2-1-6, Etchu-jima, Koto-ku, Tokyo 135-8533, Japan.
[2]Functional Devices Research Laboratory, Sharp Corporation, 273-1 Kashiwa, Kashiwa-shi, Chiba 277, Japan.

0896-1107/99/0200-0311$16.00/0

$Pr_{1-x}Ca_xMnO_3$ system, AFI-FM transition can be also driven by illumination with X-rays at the low temperature (<40 K) [12]. This transition is accompanied by significant change in the lattice structure and can be reversed by thermal cycling. No change is observed when the X-ray beam is switched off.

In the present communication, we report photo-induced change of the effective spin susceptibility observed in X-band electron spin resonance (ESR) in $Pr_{0.65}Ca_{0.35}MnO_3$ powder samples characterized well by X-ray diffraction. The photo-induced effect is clearly caused by the injection of photons with laser light with energy of 1.17 eV. The results under optimal photo-excitations at various temperatures exclude the laser heating as the origin of the above effect. The observed photo-induced effects appears remarkably around 80 K–90 K, which is characteristic temperature range below T_{CAF} [13,14]. The origin of the present photo-induced effect is attributed to be the formation of short-range FM states due to the breaking of AF ordering, which is possibly triggered by the collapse of CO states induced by injection of photons.

2. EXPERIMENTS

The powder samples of $Pr_{0.65}Ca_{0.35}MnO_3$ were prepared by calcining the mixture of prescribed amount of manganese and calcium carbonates and praseodymium oxide in the air at 1400°C using the usual ceramic technique. The powder samples were used for all measurement here.

Prior to the ESR study, we carried out the powder X-ray diffraction measurement to verify the existence of single $Pr_{0.65}Ca_{0.35}MnO_3$ phase and to get the lattice constants as a function of temperature from 300 K to 10 K. The powder samples were attached to quartz sample holder. Data were collected using a X-ray powder diffractometer (MXP18, Mac Science Co. Ltd.) with Cu K_α radiation equipped with a rotating anode generator operated at 40 kV and 200 mA 2θ-θ step scan mode was used with step width $\Delta\theta = 0.01°$–$0.02°$, accumulation time 10–100 sec/step, and scan range 15°–100° in 2θ. The calculation of the observed structure factor together with both profile fitting process and the refinement of crystal structure from the powder diffraction data was performed by Rietveld method with a program RIETAN [15]. Figure 1 shows the powder X-ray diffraction profile at 290 K together with and the result of the profile fit by Rietveld analysis with solid lines. The X-ray powder

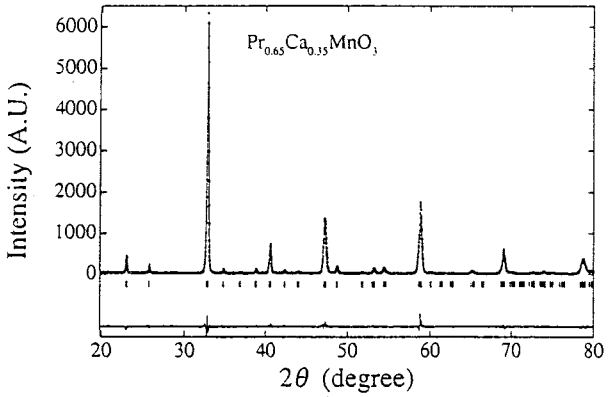

Fig. 1. Powder X-ray diffraction profiles with + mark and the Rietveld fitting result with solid lines for $Pr_{0.65}Ca_{0.35}MnO_3$ at 290 K.

analysis indicated that the present powder sample was in single phase with the distorted perovskite structure and symmetry is orthorhombic with the space group *Pbnm* with lattice constants $a = 5.428$ Å, $b = 5.455$ Å, and $c = 7.663$ Å, respectively, at 290 K [13,16].

The ESR measurement for the electron spin on Mn^{3+} and Mn^{4+} ionic sites in $Pr_{0.65}Ca_{0.35}MnO_3$ was done using a 100 kHz field modulated spectrometer operated at 9.0 GHz. The amount of the sample was 0.5 mg. The sample was mounted in a liq. He continuous-flow type cryostat and was cooled from 300 K to 10 K. The sample temperature was monitored by thermometer located near sample and was controlled by varying the flow rate of liq. He. To obtain dc magnetization giving us a complemental information we measured under the magnetic field 0.01 T by SQUID susceptometer.

3. RESULTS AND DISCUSSION

Figure 2 shows the powder X-ray diffraction profiles of $Pr_{0.65}Ca_{0.35}MnO_3$ at 296 K, 190 K, 100 K, and 50 K. It is clear that some additional diffraction peaks appear at 190 K which is below $T_{CO} \sim 215$ K. The integrated intensities of the peaks assigned as Bragg reflections based on the unit cell parameters at 296 K are almost the same between above and below $T_{CO} \sim 215$ K. According to the indices as shown in Fig. 3, the newly appeared peaks are assigned successfully as a superlattice reflection with the unit cell parameters at 296 K. In Fig. 2, a superlattice structure, $\mathbf{a} \times 2\mathbf{b} \times \mathbf{c}$ relative to the unit cell at 296 K has been confirmed below 200 K, which conducts a further complemental evidence for the CO state associated with the alternation of Mn^{3+} and Mn^{4+}

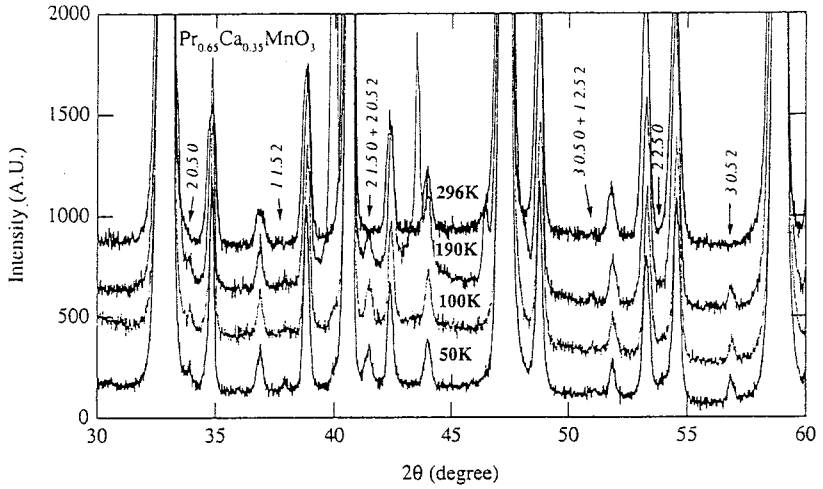

Fig. 2. Superlattice reflections observed in the powder X-ray diffraction profiles for $Pr_{0.65}Ca_{0.35}MnO_3$ at representative temperature.

ions [2,4]. The detailed temperature dependence of these superlattice reflections will be reported elsewhere [16]. The observed superlattice reflection lines remain down to 50 K via T_{AF} and T_{CA}, which confirms that the CO state is retained without external stimulation such as electric, magnetic field etc.

To investigate a photo-induced effect, a He–Ne CW laser and Nd-YAG CW laser were employed for an optical excitation. The phonon energy was 1.17 eV (wavelength $\lambda = 10640$ Å) for the Nd-YAG laser. The laser power was adjusted with an optical slit which were 5 mW, 50 mW, and 175 mW which is equivalent to the injection of 9×10^{17} photons/sec. The laser light was introduced into the sample situated in a cavity resonator through a double shielded quartz tube belonging to the continuous flow He cryostat. The laser spot size was about 1 mm^2. The penetration depth of the laser light is estimated to be about 0.2 mm for the present sample. The ESR measurement was done under the sequence in which we measure the ESR profile without optical excitation, then the profile under excitation with the Nd-YAG laser and finally without optical excitation again in turn to check if any kinds of damage to the sample occur.

Figure 3a shows the ESR profiles under dark, without injection of photons, for the $Pr_{0.65}Ca_{0.35}MnO_3$ as thin solid lines. In $Pr_{1-x}Ca_xMnO_3$, the phase diagram has been determined by the measurements of resistivity, magnetization, and neutron diffraction [1,3]. For the sample with $x = 0.35$, it is the insulator without an external magnetic field at whole temperature range and it shows the paramagnetic behavior at room temperature (PI), then turns into the COI with the lattice distortion at $T_{CO} \sim 215$ K, successively into the pseudo CE-type AFI around 180 K with the antiferromagnetic component where the ferromagnetic double-exchange interaction is quenched by a CO effect, and eventually into the canted antiferromagnetic state (CAFI) $T_{CA} \sim 115$ K. In association with the above successive phase transitions, the ESR profiles retain Lorentzian curvature down to around 100 K which is below T_{CA}. The dc magnetization exhibits paramagnetic behavior down to CO transition and continues to increase via AFI and CAFI phases down to around 100 K. It is noted that an abrupt increase of the magnetization occurs below T_{CA} associated with the spontaneous magnetization due to canted spins at both Mn^{3+} and Mn^{4+} sites. Below 100 K, the ESR profiles become broadened as shown in Fig. 3b with some kind of dissociation of total magnetic moments, which is in accordance with the behavior of dc magnetization in the warming run after zero-field cooling [13]. The exact mechanism of disappearance of the ESR signal is not clear. Further investigation is necessary for clarity on this point. The dc magnetization exhibits a spin-glass behavior which has also been signaled from the magnetic neutron scattering study by Yoshizawa *et al.* [2]. Both in Figs. 1a and b, the thick solid lines show the representative resonance profiles measured under photon injection by Nd-YAG laser (hu = 1.17 eV) at some temperatures. It is clear that the resonance intensity initiate to depend on the injection of photons below $T_{CO} \sim 215$ K with decreasing temperature. Remarkably, the effect of irradiation on the resonance profile becomes predominant below 100 K which is close to the suspected onset temperature of spin-glass state below $T_{CA} \sim 115$ K [2,13].

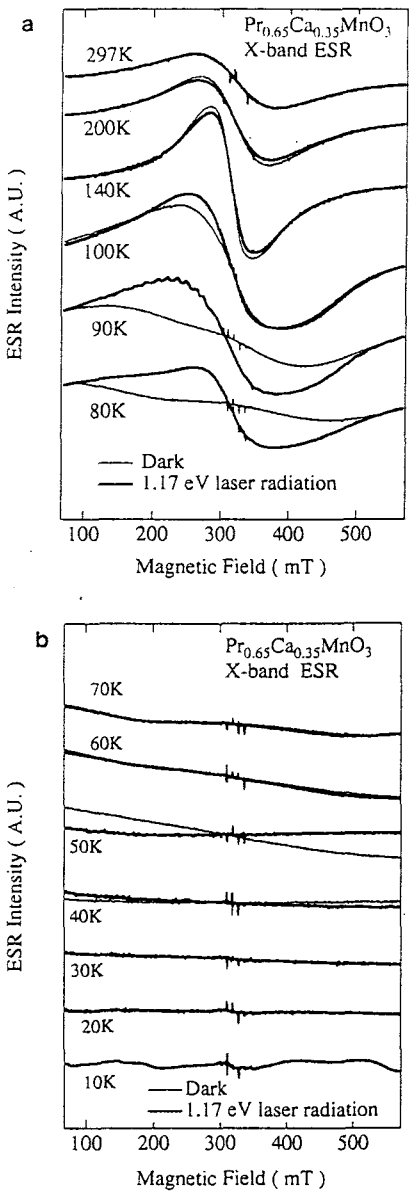

Fig. 3. (a) and (b): ESR profiles for $Pr_{0.65}Ca_{0.35}MnO_3$ without optical excitation (dark: thin solid curves) and with optical excitation by Nd-YAG laser (1.17 eV thick solid curves). In the phase diagram of $Pr_{0.65}Ca_{0.35}MnO_3$ without external stimulation, the paramagnetic state (P) at 297 K, the charge-ordered state (CO) at 215 K, antiferromagnetic state (AF) at 180 K, the canting antiferromagnetic state (CAF) below 125 K. The existence of spin glass state below 100 K has been proposed by Yoshizawa *et al.* [1].

One might suspect that this transition is simply driven by the laser heating. The evidence against the laser heating is provided by the temperature dependence of ESR profiles. The ESR profiles with the optical excitation show different behavior expected from temperature increase as shown in profiles in the temperature range 90 K–80 K and 50 K–40 K. Also there is no difference among those profiles at lowest temperature where it is expected to be sensitive to this kind of heating. This transition was reproducible, not permanent, and also not due to any damage to the sample by laser irradiation. In fact, the ESR profile after the postmeasurement with the optical excitation shows almost identical with that obtained prior to the measurement under optical excitation.

As shown in Figs. 3a and b, in the temperature range of 100 K–80 K, the obtained photo-induced effect indicates that the effective spin susceptibility increases thanks to the injection of photons with 1.17 eV. In contrast, the ESR profiles at 50 K exhibits that the effective spin susceptibility decreases under laser irradiation with good reproducibility. It is remarked that no significant difference was observed at 70 K, 60 K, and below 30 K.

The essential physics of the CMR materials $R_{1-x}A_xMnO_3$ system is the interplay between a strong electron–phonon coupling leading to CO state associating with antiferromagnetic spin arrangement and the "double exchange" effect of ferromagnetic spin alignment on electron kinetic energy, which eventually conducts to metallic state. Therefore, simple interpretation of the above photo-induced effect is due to the increase of the spin susceptibility together with the dissociation of antiferromagnetic AF state based on CO state to ferromagnetic (F) state. The present interpretation indicates that the photo-induced I–M transition, equivalent collapse of CO state, may occur under excitation by laser light with optimal energy.

To realize the above transition, we speculate that the existence of the prescribed spin-glass state [15] make it easy to lead the onset of I–M (AF–F) transition thanks to the short-range ordered canted antiferromagnetic state. Such transition induces the enhancement of metallicity associated with so-called double exchange interaction. It proves the photo-induced increase of the effective spin susceptibility as shown in Fig. 2 (80 K), which confirms the increase of the number of ferromagnetic spin.

The spin-glass state postulated by Yoshizawa *et al.* [2] may play an important role to realize photo-induced transition at 80 K. The composition of $Pr_{0.65}Ca_{0.35}MnO_3$ is not responsible for commensurate CO as in $Pr_{0.5}Ca_{0.5}MnO_3$. In case of $Pr_{0.5}Ca_{0.5}MnO_3$, the commensurate CO order with regular charge alternation in long range as $-Mn^{3+}-Mn^{4+}-Mn^{3+}-$. For $Pr_{0.65}Ca_{0.35}MnO_3$, as far as we consider trivalent (high spin) and tetravalent ionic (low spin)

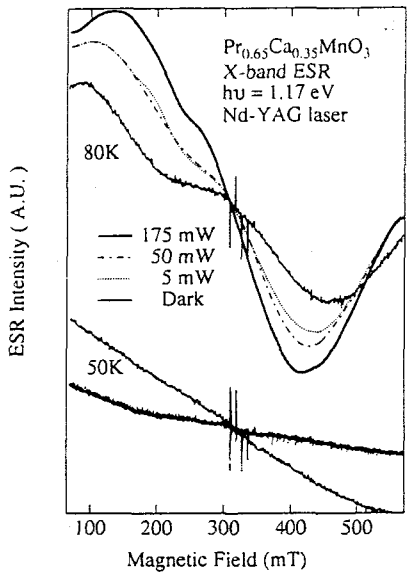

Fig. 4. ESR profiles for $Pr_{0.65}Ca_{0.35}MnO_3$ at 80 K and 50 K under different excitation power with photon energy 1.16 eV. It is worth noting that the laser power has been measured in front of the injection window of the resonance cavity of ESR alignment. Therefore, the injected laser light releases photon density by diffuse scattering due to double shielded quartz tubes of liq. He cryosystem inside the cavity.

states, some kind of discommensuration should appear. In this case, the commensurability conducts to random distribution of AF and F exchange interactions which eventually forms spin-glass state. Such state can be reorganized by laser excitation with optimal photon energy. At 50 K, it is notable that the incident photons eventually decreases the effective spin susceptibility with enough reproducibility. Precise mechanism is an open question for further investigation. The above results are reversible for repetition of the measurement under laser radiation and under dark conditions.

Figure 4 exhibits the incident laser power dependence of the ESR profiles for $Pr_{0.65}Ca_{0.35}MnO_3$ at 80 K and 50 K. Those ESR profiles show different laser power dependence at 80 K and 50 K. At 80 K, there is obvious change in ESR profiles and the effective spin susceptibility increases with increasing laser power. It is noted that the described value of the laser power does not mean the exact value injected to the samples due to the double shielded He flow guide made from quartz glass as mentioned above. At 50 K, there is a few changes as a function of incident laser power in ESR profiles. This result shows that it is rather difficult to achieve the change of spin arrangement by laser radiation.

4. SUMMARY

In summary, ESR was studied on the charge-ordered state in $Pr_{0.65}Ca_{0.35}MnO_3$ for the electron spin states of $3d-t_{2g}$ (S = 2) and $3d-e_g$ (S = 3/2) on Mn^{3+} and Mn^{4+} ions by injection of laser light with photon energy of 1.17 eV provided by Nd-YAG laser. A prominent increase of the effective spin susceptibility was clearly found out associated with the injection of photons with its energy 1.17 eV in the temperature range 90 K–80 K which are below the transition temperature from the antiferromagnetic charge ordered state to the canted antiferromagnetic spin alternation state, $T_{CAF} \sim 125$ K. This result is suspected to be a kind of insulator–metal transition due to propagation of the delocalized carriers thanking to double exchange interaction in the photo-induced charge-ordering collapsed state.

ACKNOWLEDGMENTS

We would express our gratitude to Dr. T. Tamura (SRL-ISTEC) for the dc magnetization measurement and Dr. N. Tsuchimine (Toshima Mfgs Co. Ltd.) for sample preparation.

REFERENCES

1. Z. Jirak, S. Krupicka, Z. Simsa, M. Dlouha, and S. Vratislav, *J. Mag. Mag. Mater.* **53**, 153–166 (1985).
2. H. Yoshizawa, H. Kawano, Y. Tomioka, and Y. Tokura, *Phys. Rev. B* **52**, 1689–1692 (1996).
3. Y. Tomioka, A. Asamitsu, H. Kuwahara, and Y. Moritomo, *Phys. Rev. B* **53**, 1689–1692 (1996).
4. H. Chiba, M. Kikich, K. Kusaba, Y. Muraoka, and Y. Syono, *Sol. Stat. Com.* **99**, 499–502 (1996).
5. S. Jin, T. H. Tiefel, M. McCormack, R. A. Fastnacht, R. Ramesh, and L. H. Chen, *Science* **264**, 413–415 (1994).
6. A. J. Millis, B. I. Shraiman, and R. Mueller, *Phys. Rev. Lett.* **77**, 175–178 (1996).
7. D. Feinberg, P. Germain, M. Grilli, and G. Seibold, *Phys. Rev. B* **57**, 5583–5586 (1998).
8. C. Zener, *Phys. Rev.* **82**, 403 (1951).
9. J. B. Goodenough, *Phys. Rev.* **100**, 564 (1955).
10. P. W. Anderson and H. Hasegawa, *Phys. Rev.* **100**, 675–681 (1955).
11. A. Asamitsu, Y. Tomioka, H. Kuwahara, and U. Tokura, *Nature* **388**, 50 (1997).
12. V. Kiryukhin, D. Casa, J. P. Hill, B. Keimer, A. Vigilante, Y. Tomioka, and Y. Tokura, *Nature* **386**, 813 (1997).
13. O. Yanagisawa, M. Izumi, W.-Z. Hu, K. Nakanishi, and H. Nojima, *Phys. Rev. B* (to be submitted).
14. D. E. Cox, P. G. Radaelli, M. Marezio, and S.-W. Cheong, *Phys. Rev. B* **57**, 3305–3314 (1997).
15. F. Izumi, in R. A. Young, ed., *The Rietveld Method* (Oxford University Press, Oxford, 1993), Chap. 13.
16. K. Nakanishi, H. Nojima, O. Yanagisawa, M. Izumi, and W.-Z. Hu, *Phys. Rev. B* (to be submitted).

PHOTO-INDUCED EFFECT ON THE CHARGE-ORDERED STATE WITH CANTED ANTIFERROMAGNETIC SPIN ORDER IN $Pr_{0.65}Ca_{0.35}MnO_3$

OSAMI YANAGISAWA, MITSURU IZUMI, WEI-ZHI HU, KAI-HUA HUANG
Laboratory of Applied Physics, Tokyo University of Mercantile Marine, 2-1-6, Etchu-jima, Koto-ku, Tokyo 135-8533, JAPAN

KENJI NAKANISHI, HIDEO NOJIMA
Functional Devices Research Laboratory, Sharp Corporation, 273-1, Kashiwa, Kashiwa-shi, Chiba 277 -0005, JAPAN

Abstract

Electron-spin resonance (ESR) and powder X-ray diffraction were studied for the charge-ordered (CO) state in well-characterized $Pr_{0.65}Ca_{0.35}MnO_3$ (Space group: *Pbnm* at 296 K). Upon injection of near infrared cw-YAG laser light with the photon energy of 1.17 eV, the remarkable change of the spin-resonance profile and the prominent decrease of the intensity of superlattice reflections coming from the charge-orderd state were observed below the transition temperature from the antiferromagnetic CO state to the canted antiferromagnetic spin alternation ground state, T_{CAF} ~125 K. The present result is from neither heating by laser irradiation nor phase segregation due to X-ray irradiation, and eventually provides a structural evidence of collapse the CO state by photon injection. We suspect that the photo-induced insulator-metal transition occurs together with collapse of the CO state.

1. Introduction

The distorted perovskite manganese, e.g., $Pr_{1-x}Ca_xMnO_3$ has recently attracted much attention by virtue of a magnetic field driven insulator-metal (I-M) transitions, an effect termed colossal magnetoresistance (CMR) [1-5]. The ground state is characterized by a competing interaction between two different ground states: a charge-delocalized (CD)

I. Nedkov and M. Ausloos (eds.), Nano-Crystalline and Thin Film Magnetic Oxides, 263–268.

metallic state with ferromagnetic (F) spin arrangement under relatively small Jahn-Teller (JT) distortions [6-8] and the other is a charge-ordered (CO) insulating state.

In CD state. the ferromagnetic (F) metal itself has been clarified in the double-exchange interaction scheme originally proposed by Zener [8]. On the other hand, the CO state is characterized as both superlattice structure and an antiferromagnetic (AF) spin arrangement on Mn ions, and the Mn^{3+} sublattice retains a cooperative JT distortion. The CO state is optimized at x = 0.5 (commensurate), a deviation of x from 0.5 (discommensuration) decreases the stability of the CO state. Around x = 0.3, the system is on the phase boundary of the transition from the CO insulator to the FM phase, indicating that the external stimulation cause the transition from the CO to the FM phase with relative ease [1][2][3-5].

In $Pr_{0.7}Ca_{0.3}MnO_3$ system, the collapse of the CO state by magnetic field, which is the transition from AF-CO phase to F-CD phase, was found [1]. An electric current also triggers this type of transition [4]. In $Pr_{0.7}Ca_{0.3}MnO_3$, the AF-CO to F-CD transition as a phase-segregation can be driven by SOR-X-ray exposure below 40 K [5,7]. The transition is together with a break of the superlattie which was formed in the CO state and reversible by thermal cycle, but neither change nor revival of the superlattice reflection intensity is observed when the SOR-X-ray beam is switched off after the suppression of the superlattice [5]. Miyano et al [3] have stated the trace of the collapse of the CO state by observation of photocurrent under the coexistence of the applied electric field and pulse laser irradiation with 1.2 eV in the photon energy range 0.6 to 3.5 eV. Thus, there is no X-ray diffraction study of the collapse of the CO state under laser irradiation, if it exists.

In the present communication, we report photo-induced increase of effective spin susceptibility observed in X-band electron spin resonance (ESR) and study a photo-induced effect on the powder X-ray diffraction (PXD) in $Pr_{0.65}Ca_{0.35}MnO_3$.

2. Results and Discussion

The powder samples of $Pr_{0.65}Ca_{0.35}MnO_3$ were carefully prepared by calcining the mixture of prescribed amount of manganese and calcium carbonates and praseodymium oxide in the air at 1400 °C using the usual ceramic technique [8].

Prior the ESR study, we carried out the powder X-ray diffraction measurement to verify the existence of single $Pr_{0.65}Ca_{0.35}MnO_3$ phase using a X-ray powder diffractometer (MXP18, Mac Science Co. Ltd.) with CuK_a radiation (λ = 1.5418 Å). The refinement of the crystal parameters by profile fitting indicated that the sample is in single phase with space group Pbnm with lattice constants a = 5.428 Å, b = 5.455 Å and c = 7.663 Å at 290 K [6]. The ESR measurement for the electron spin on Mn ionic sites in $Pr_{0.65}Ca_{0.35}MnO_3$ was done using a 100 kHz field modulated spectrometer operated around 9 GHz. The amount of the sample was 0.5 mg.

To investigate a photo-induced effect, a cw-YAG laser was employed for a optical excitation. The photon energy was unique and 1.17 eV (λ = 10640 Å) which is in near-infrared region. The maximum laser power was monitored to be 175 mW ($9x10^{17}$ photons/sec). It is noted that the value of the laser power does not indicate the precise value injected into the samples due to the existence of the window shield. The PXD and ESR were carried out under the sequence in which we measure the profile without the laser irradiation (dark), subsequently the profile with the optical excitation and finally without the laser irradiation again in turn to check if any kinds of irreversible damage to the sample occur.

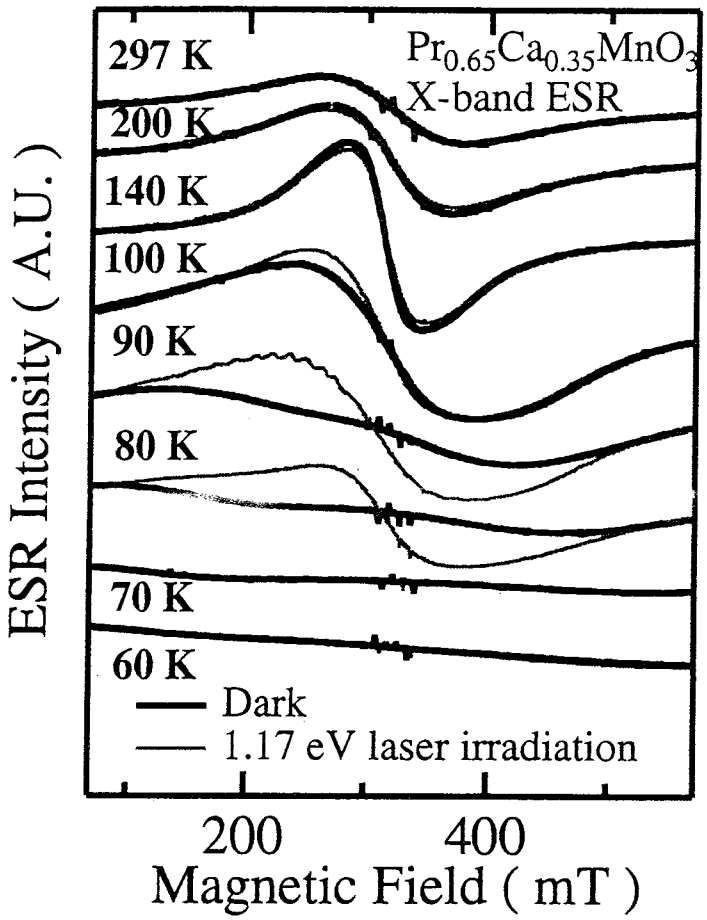

Figure 1. ESR profiles for $Pr_{0.65}Ca_{0.35}MnO_3$ without optical excitation (Dark: thin solid curves) and with optical excitation by cw-YAG laser (thick solid curves). In the phase diagram of $Pr_{0.65}Ca_{0.35}MnO_3$ without external stimulation, the paramagnetic state (P) at 297 K, the charge-ordered state (CO) at 215 K, antiferromagnetic state (AF) at 180K, the canting antiferromagnetic state (CAF) below 125 K. The existence of spin glass state below 100 K has been proposed by Yoshizawa et al [1].

The phase diagram of $Pr_{0.75}Ca_{0.35}MnO_3$ has been determined by the measurements of resistivity, magnetization and neutron diffraction (see Fig. 1) [6]. Figure 1 shows the ESR profiles under dark, without injection of photons, for the $Pr_{0.65}Ca_{0.35}MnO_3$ as thin solid lines. Below 100 K, the ESR profiles become broadened. The exact mechanism of broadening of the ESR signal is not clear but possibly related to a spin-glass behavior which has also been signaled from the magnetic neutron scattering study by Yoshizawa et al [1]. In Fig. 1, the thick solid lines show the representative resonance profiles measured under cw-YAG laser irradiation. Remarkably, the effect of irradiation on the resonance profile becomes predominant below 100 K which is close to the suspected onset temperature of spin-glass state below T_{CAF} ~ 125 K [2]. One might suppose that this is simply driven by the laser heating. The evidence against the laser heating is provided by the temperature dependence of ESR profiles. The ESR profiles with the optical excitation show different behaviour expected from temperature increase as shown in profiles in the temperature range 90 K - 80 K and 70 K - 60 K. This transition was reproducible, not permanent and also not due to any damage to the sample by laser irradiation. In fact, the ESR profile after the post-measurement with the optical excitation shows almost identical with that obtained prior the measurement under optical excitation.

As shown in Fig. 1, in the temperature range of 100 K - 80 K, the obtained photo-induced effect indicates that the narrowing of the resonance profile occurs thanks to the injection of photons with 1.17 eV. It is remarked that no significant difference was observed at both 70 K and 60 K.

The photo-induced effect for the superlattice reflections was studied under the photon injection by cw-YAG laser irradiation. Figures 2(a) and 2(b) show the PXD profiles of superlattice reflections from (2, 1.5, 0) and (2, 0.5, 2) together with fundamental Bragg reflection from (1, 1, 3) at 30 K and at 40 K, respectively. These reflections were selected for clarity to compare the Bragg reflection intensities with superlattice reflection ones. They exhibit the stable diffraction under the X-ray irradiation to measure the diffraction profiles. As shown in Fig. 2, in contrast to the Bragg reflections, a prominent suppression of the superlattice reflection intensities was found out under the YAG laser irradiation. One might suspect that this transition is simply driven by the laser heating. In any case, if the incident light provides the increase of temperature one should observe the change of the lattice spacing. There is no remarkable shift of the Bragg reflection angle for (1, 1, 3) reflection (less than 0.04 % of the length of lattice spacing as estimated from the Bragg reflection angles with and without laser irradiation) for (1, 1, 3) reflection.

The observed suppression of the superlattice reflection evidently indicates that near-infrared laser irradiation with proper photon energy ~1.2 eV induces the collapse of CO state with ease, which would be together with probable the AF-CO to F-CD transition. The present observation is not far from the previously reported I-M transition triggered by photocarrier generation by Miyano et al [3]. Without structural evidence, they have

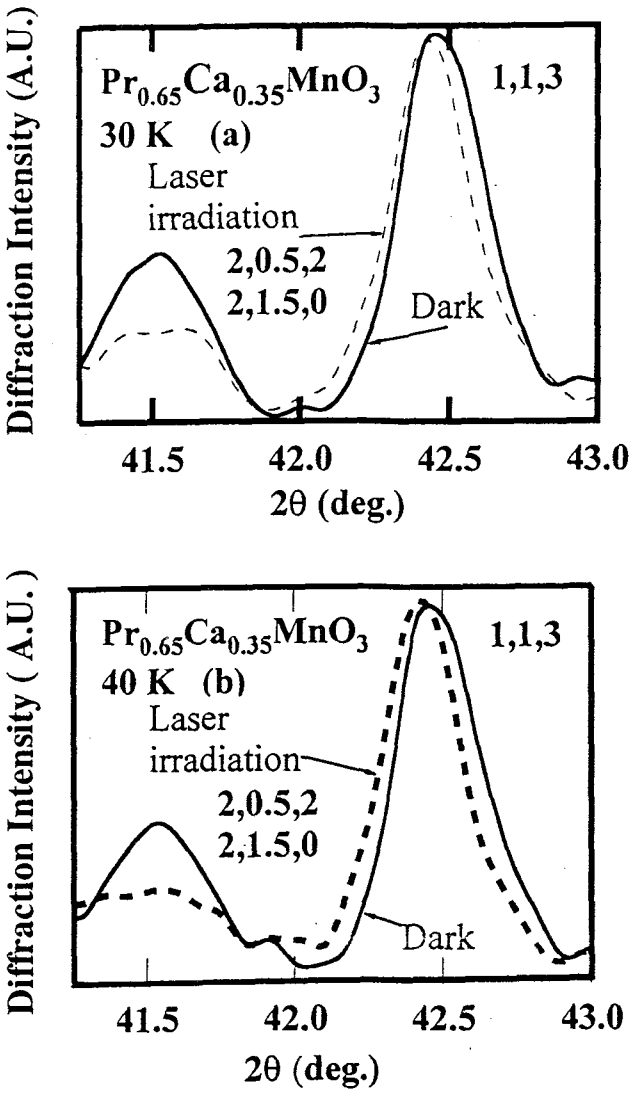

Figure 2. Powder X-ray diffraction profiles at 30 K(a) and 40 K(b) from (2, 1.5, 0), (2 ,0.5, 2) and (1, 1, 3) reflections with (broken curve) and without (solid curve) cw-YAG laser irradiation (hu = 1.17 eV).

stated the trace of the collapse of the CO state by observation of photocurrent under the coexistence of the applied electric field and pulse laser irradiation with 1.2 eV. First we

discuss the reason why we detect the collapse of CO state for photon energy ~1.2 eV. This energy value is characteristic in the optical spectra in these manganites. It has been assigned as a charge-transfer excitation energy of an electron from the lower JT split e_g of Mn^{3+} to the e_g of adjacent Mn^{4+} ion, which exhibits the promotion of the dipole active photoionization of the JT small polaron [20]. Our present result suggests that the simple near-infrared laser irradiation with the characteristic photon energy ~1.2 eV enhances some kind of vibronic state and eventually releases the cooperative JT distortion associated with CO state.

Finally, we stress that the present observation of the collapse of the CO state with relative ease is strongly related to the discommensuration for the charge and spin ordering in CO state for $0.3 \leq x \leq 0.75$. The deviation of x from 0.5 plays an important role for a melting of the CO state with relative ease at the low temperature side. The CAF state is related with the invasion of the metallic phase based on the collapse of the CO state with near-infrared laser irradiation.

3. References

1. Yoshizawa, H., Kawano, H., Tomioka, Y., and Tokura, Y. (1995) Neutron-diffraction study of the magnetic-field-induced metal-insulator transition in $Pr_{0.7}Ca_{0.3}MnO_3$, *Phys. Rev.* B **52**, 13145-13148.
2. Tomioka, Y., Asamitsu, A., Kuwahara, H., and Moritomo, Y. (1996) Magnetic-field-induced metal-insulator phenomena in $Pr_{1-x}Ca_xMnO_3$ with controlled change-ordering instability, *Phys. Rev.*, B **53**, 1689-1692.
3. Miyano, K., Tanaka, T., Tomioka, Y., and Tokura, Y. (1997) Photoinduced Insulator-to-Metal Transition in a Perovskite Manganite, *Phys. Rev. Lett.*, **78**, 4257-4260.
4. Asamitsu, A., Tomioka, Y., Kuwahara, H., and Tokura, Y. (1997) Current switching of resistive states in magnetoresistive manganites, *Nature* **388**, 50-52.
5. Kiryukhin, V., Casa, D., Hill, J.P., Keimer, B., Vigilante, A., Tomioka, Y., and Tokura, Y. (1997) An X-ray-induced insulator-metal transition in a magnetoresistive manganite, *Nature*, **386**, 813-815.
6. Jirak, Z., Krupicka, S., Simsa, Z., Dlouha, M., and Vratislav, S. (1985) Neutron Diffraction Study of $Pr_{1-x}Ca_xMnO_3$ Perovskites, *J. Mag. Mag. Mat*. **53**, 153-166.
7. Cox, D.E., Radaelli, P.G., Marezio, M., and Cheong, S-W. (1998) Structural changes,clustering,and photoinduced phase segregation in $Pr_{0.7}Ca_{0.3}MnO_3$, *Phys. Rev.* B, **57**, 3305-3314.
8. Zener, C. (1951) Interaction between the d-Shells in the Transition Metals.II. Ferromagnetic Compounds of Manganese with Perovskite Structure, *Phys. Rev.*, **82** , 403-405.
9. Zhao, Y.G., Li, J.J., Shreekala, R., Drew, H.D., Chen, C.L., Cao, W.L., Lee, C.H. (1998) Ultrafast Laser Induced Conductive and Resistive Transients in $La_{0.7}Ca_{0.3}MnO_3$: Change Transfer and Relaxation Dynamics, *Phys. Rev. Lett.*, **81**, 1310-1313.

ELSEVIER

Physica B 271 (1999) 235–241

PHYSICA B

www.elsevier.com/locate/physb

Evidence of photo-induced melting of the charge-ordered state in $Pr_{0.65}Ca_{0.35}MnO_3$ by X-ray diffraction

Osami Yanagisawa[a], Mitsuru Izumi[a,*], Wei-Zhi Hu[a], Kai-Hua Huang[a], Kenji Nakanishi[b], Hideo Nojima[b]

[a]*Laboratory of Applied Physics, Tokyo University of Mercantile Marine, 2-1-6 Etchu-jima, Koto-ku, Tokyo 135-8533, Japan*
[b]*Functional Devices Research Laboratory, Sharp Corporation, 273-1 Kashiwa, Kashiwa-shi, Chiba 277-0005, Japan*

Received 11 September 1998; accepted 4 February 1999

Abstract

Powder X-ray diffraction was studied in respect of the photo-induced effect on the charge-ordered (CO) structure of $Pr_{0.65}Ca_{0.35}MnO_3$ (Space group: Pbnm at 296 K). Below 215 K, the superlattice reflection peaks appear associating with the formation of the CO state with the $a \times 2b \times c$ cell and the present CO structure is maintained down to at least 10 K. A cw-YAG laser light ($h\upsilon = 1.17$ eV) irradiation conducts to the prominent decrease of the intensity of superlattice reflections. The present result is from neither the heating by laser irradiation nor phase segregation due to X-ray irradiation and eventually provides a structural evidence of collapse of the CO state by photon injection and allows to suspect that the photo-induced insulator–metal transition occurs together with the collapse of the CO state.

PACS: 75.25. + z; 75.50. − y; 75.30.Et; 75.30.Kz

Keywords: Magnetic materials; Oxides; Phase transitions; Colossal magnetoresistance; Powder X-ray diffraction; Photo-induced effect

1. Introduction

The distorted perovskite manganese, $R_{1-x}A_xMnO_3$: R is trivalent rare earth element and A is divalent alkaline earth element have recently attracted much attention by virtue of their unusual magnetic and electric properties [1–7]. For example, some of these manganese exhibit a magnetic field driven insulator–metal (I–M) transitions where the conductivity and magnetization change dramatically, an effect termed colossal magnetoresistance (CMR) [1–4]. The I–M transitions in the manganese can be achieved not only by a magnetic field, but also by other external field and/or stimulation.

The ground state of the $R_{1-x}A_xMnO_3$ system is characterized by a competing interaction between the two different ground states: a charge-delocalized (CD) state is in ferromagnetic (F) spin arrangement with metalicity, and exhibits relatively small Jahn–Teller (JT) distortions [8,9] and the other is a charge-ordered (CO) insulating state. In CD state, the ferromagnetic (F) metal itself has been

* Corresponding atuhor. Tel.: + 81-3-5245-7462; fax: + 81-3-5245-7462.
E-mail address: izumi@ipc.tosho-u.ac.jp (M. Izumi)

0921-4526/99/$ - see front matter
PII: S0921-4526(99)00215-X

clarified in the double-exchange interaction scheme originally proposed by Zener [10] and further developments are under way [11,12], in which the doped holes at e_g orbital in Mn^{4+} site exhibit a kind of hopping conduction associated with the aligned spins for both Mn^{4+} and Mn^{3+} sites. On the other hand, the CO state is characterized as an antiferromagnetic (AF) spin arrangement on Mn ions, and the Mn^{3+} sublattice retains a cooperative JT distortion, thereby giving rise to a combination of charge, orbital, and magnetic ordering. Upon heating, both the CO and the CD states transform into a charge-localized paramagnetic insulator (PI) phase, characterized by semiconducting properties. The switching in DC resistivity between CO and CD states, I–M transition, can be achieved not only by a magnetic field, but also by other external field and/or stimulation.

The CO state occurs as observed in $La_{1-x}Ca_xMnO_3$ ($x = \frac{1}{2}$) [13], $Pr_{1-x}Sr_xMnO_3$ ($x = \frac{1}{2}$) [2], $Nd_{1-x}Sr_xMnO_3$ ($x = \frac{1}{2}$) [14], and also in $Pr_{1-x}Ca_xMnO_3$ ($x = \frac{1}{2}$) [1,2,8–16]. The charge carriers localize on the Mn ion site and form real-space alternation of 1 : 1 Mn^{3+}/Mn^{4+} species, the so-called "charge crystal" associated with the doubling of the unit cell in unique crystallographic direction. The charge-ordering appears at higher temperature than the magnetic transition temperature. The CO state is stabilized over a wide range of concentration, around $0.3 < x < 0.7$ in the $Pr_{1-x}Ca_xMnO_3$ system [1,2,8].

The CO state has been mostly observed when the concentration of charge carriers takes a rational value of the periodicity of the crystal lattice. The commensurability of the carrier concentration with a periodicity of the crystal lattice is related to the stability of the CO state. The CO state is optimized at $x = 0.5$ (commensurate), a deviation of x from 0.5 (discommensuration) decreases the stability of the CO state. Around $x = 0.3$, the system is on the phase boundary of the transition from the CO insulator to the FM phase, so that the external stimulation cause the transition from the CO to the FM phase with relative ease [1,2,5–7].

For the $Pr_{1-x}Ca_xMnO_3$ system, the collapse of the CO state by magnetic field, which is the transition from antiferromagnetic charge-ordered (AF-CO) state to ferromagnetic charge-delocalized (F-CD), was found together with the structural evidence at the low temperature [1]. An electric current (and by implication of a static electric field) also triggers this type of transition at the low temperature [6]. In the $Pr_{0.7}Ca_{0.3}MnO_3$ system, the AF-CO to F-CD transition as a phase-segregation can be driven by SOR-X-ray exposure below 40 K [7,9]. This transition is accompanied by a significant change in the lattice structure and can be reversed by the thermal cycle, but neither change nor revival of the superlattice reflection intensity is observed when the X-ray beam is switched off after the suppression of the superlattice with SOR-X-ray exposure. The SOR-X-ray-induced conductivity is annealed out on heating above 60 K [7]. Miyano et al. [5] have stated the trace of the collapse of the CO state by the observation of a photocurrent under the coexistence of the applied electric field and pulse laser irradiation with 1.2 eV in the photon energy range 0.6–3.5 eV. Thus, there is no X-ray diffraction study of the collapse of the CO state under laser irradiation to our knowledge.

In the present communication, we study a photo-induced effect on the powder X-ray diffraction (PXD) of $Pr_{1-x}Ca_xMnO_3$ ($x = 0.35$) in which the CO state is supposed to be easily suppressed by the external stimulation at the low temperatures [1]. We report that the superlattice reflections, which are from the CO structure associated with the alternation of Mn^{3+} and Mn^{4+} ions and not suppressed by only X-ray irradiated for the diffraction study, are suppressed under cw-YAG laser irradiation with a photon energy 1.17 eV, leading to the structural evidence of the collapse of the CO state by near-infrared laser irradiation which are lower-energy photons rather than SOR-X-rays.

2. Experiment

The powder samples of $Pr_{0.65}Ca_{0.35}MnO_3$ were carefully prepared by calcining the mixture of a prescribed amount of manganese and calcium carbonates and praseodymium oxide in the air at 1400°C using the usual ceramic technique.

In the PXD measurement, powder samples were attached to a copper sample holder which was mounted on a liq. He closed-cycle-type cryostat.

The sample temperature was monitored by a thermometer located next to the sample and was controlled within ± 0.1 K. Data were collected using MXP18 powder diffractometer with Cu K_α radiation (λ = 1.5418 Å) equipped with a rotating anode generator operated at 40 kV and 200 mA. The 2θ–θ step scan was used with step width $\Delta\theta$ = 0.01–0.02°, accumulation time 10–100 s/step. The calculation of the observed structure factor together with both profile fitting process and the refinement of crystal structure based on the PXD data was performed by Rietveld method with a program RIETAN [17].

To investigate a photo-induced effect, a cw-YAG laser was employed for an optical excitation. The photon energy was unique and 1.17 eV (λ = 10640 Å) which is near infrared region. Due to the difficulty to equalize the incident photon number for each, we did not apply other photon energy for comparison such as photon energy dependence of X-ray diffraction profile. The maximum laser power was monitored to be 175 mW (9×10^{17} photons/s). The laser light was introduced into the sample situated in the He cryostat through the window shielded with the Kapton film. It is noted that the described value of the monitored laser power does not indicate the precise value injected into the samples due to the existence of the window shielded with the Kapton film as mentioned above. The PXD was carried out under the sequence in which we measure the PXD profile without the laser irradiation (dark), subsequently the profile with the optical excitation and finally without the laser irradiation again in turn to check if any kinds of damage to the sample occur.

3. Results and discussion

The X-ray powder analysis indicated that the sample was in single phase with the distorted perovskite structure and the symmetry is orthorhombic with the space group Pbnm with lattice constants a = 5.428 Å, b = 5.455 Å and c = 7.663 Å, respectively, at 290 K. The lattice constants were measured down to 10 K. A detailed discussion based on the refined structural and atomic parameters will be reported elsewhere [18].

The phase diagram of $Pr_{1-x}Ca_xMnO_3$ has been determined by the measurements of resistivity, magnetization and neutron diffraction [3,4,8]. In the present sample with x = 0.35, it is the insulator without an external magnetic field at whole temperature range and it is PI at room temperature, then turns into the COI with the lattice distortion at $T_{CO} \sim 215$ K, successively into the pseudo-CE-type AFI with the antiferromagnetic component where the ferromagnetic double-exchange interaction is quenched by a CO effect at Néel temperature $T_N \sim$ 180 K, and finally into the canted antiferromagnetic state (CAFI) $T_{CA} \sim 125$ K.

Fig. 1 shows the PXD profiles at 296 and 50 K. The superlattice reflection peaks appear below $T_{CO} \sim 215$ K. According to the indices as shown in Fig. 1, the newly appeared peaks are assigned successfully as superlattice reflections with the unit cell parameters at 296 K as space group Pbnm. Hence, a superlattice structure, $a \times 2b \times c$ relative to the unit cell at 296 K has been confirmed below 200 K, which provides a complemental evidence for the existence of the CO state associated with the charge alternation of Mn^{3+} and Mn^{4+} ions [1,8].

Fig. 2 shows the temperature dependence of the integrated intensity of the superlattice reflection at (3, 0.5, 2) which is one of the prominently intensified ones $T_{CO} \sim 215$ K. These superlattice reflection peaks appear from $T_{CO} \sim 215$ K associated with the onset of the CO state and increases rapidly [9]. It is noted that the reflection intensity tends to be independent of temperature below $T_{CAF} \sim 215$ K. The present result confirms that the CO state is firmly retained in the ground state which provides the canted antiferromagnetic insulator. The observed superlattice reflection intensity does not change under the X-ray diffraction measurement without laser irradiation as far as we are concerned: i.e., no trace of photo-induced effect was observed for the CO state by using the present laboratory X-ray source in contrast to the previous SOR-X-ray study [7,9].

The photo-induced effect for these superlattice reflections was studied under the photon injection by cw-YAG laser irradiation ($h\upsilon$ = 1.17 eV). Figs. 3(a) and (b) show the PXD profiles of superlattice reflections from (2 1.5 0) and (2 0.5 2) together with Bragg reflection from (1 1 3). These reflections were

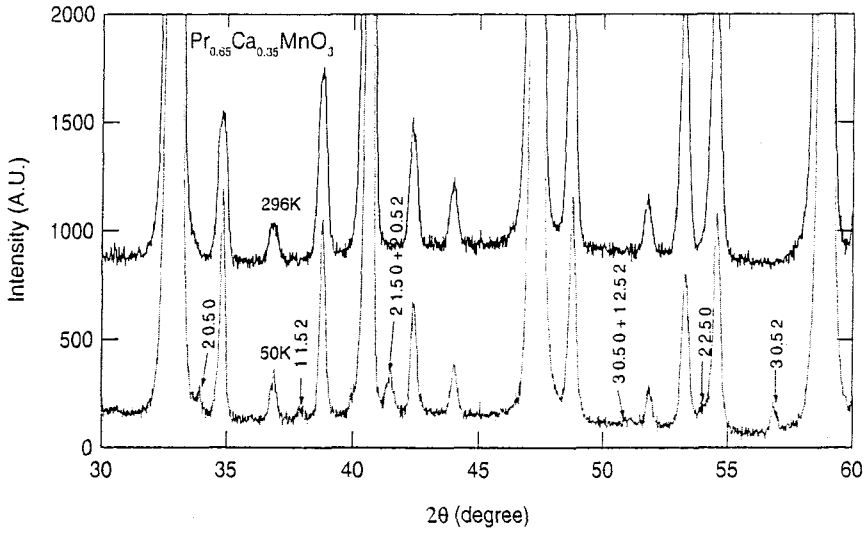

Fig. 1. Powder X-ray diffraction profiles in paramagnetic insulator at 296 K and charge-ordered (CO) phases at 50 K which is below $T_{CO} \sim 215$ K. The integrated intensities of the peaks assigned as the Bragg reflections are almost the same between those above and below T_{CO}. The newly appeared peaks are indexed successfully as superlattice reflections with the unit cell parameters at 296 K.

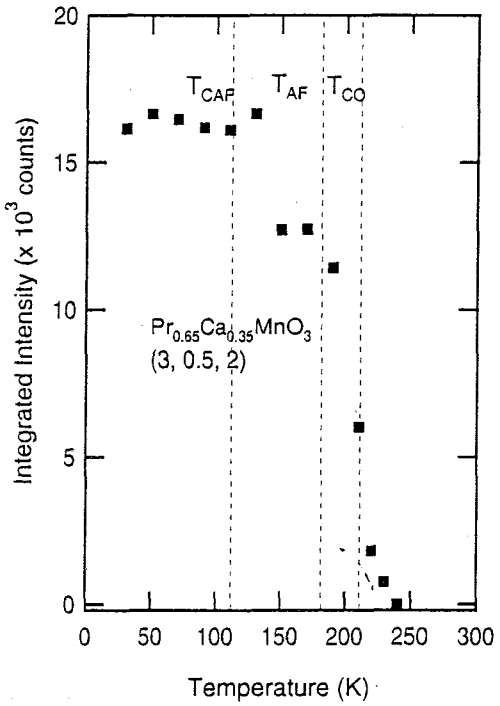

Fig. 2. Temperature dependence of the integrated intensity of superlattice reflection at (3, 0.5, 2) which is one of the prominent superlattice reflections below $T_{CO} \sim 215$ K in the $Pr_{0.65}Ca_{0.35}MnO_3$ at temperature range from 240 K down to 30 K.

selected for clarity to compare the Bragg reflection intensities with superlattice reflection ones. They exhibit the stable diffraction under the X-ray irradiation to measure the diffraction profiles. As shown in Fig. 3, in contrast to the Bragg reflections, a prominent suppression of the superlattice reflection intensities was found out under the YAG laser photon injection. One might suspect that this transition is simply driven by the laser heating. The evidence against it is given as follows. In any case, if the incident light provides an increase of temperature one should observe the change of the lattice spacing. There is no remarkable difference in both intensity and shift of the Bragg reflection angle (shift less than 0.04% of the length of lattice spacing as estimated from the Bragg reflection angles with and without laser irradiation) for (1 1 3) reflection. The length of the lattice spacing should be quite sensitive for this kind of heating. The observed intensity change of superlattice reflections was reproducible for alternation of switch-on and-off of laser, not permanent and no remarkable trace of the damage to the sample was found to diffraction profiles. It is stressed that the almost identical Bragg profile without the optical excitation was obtained to the PXD measurement under laser irradiation. The remaining intensity of the

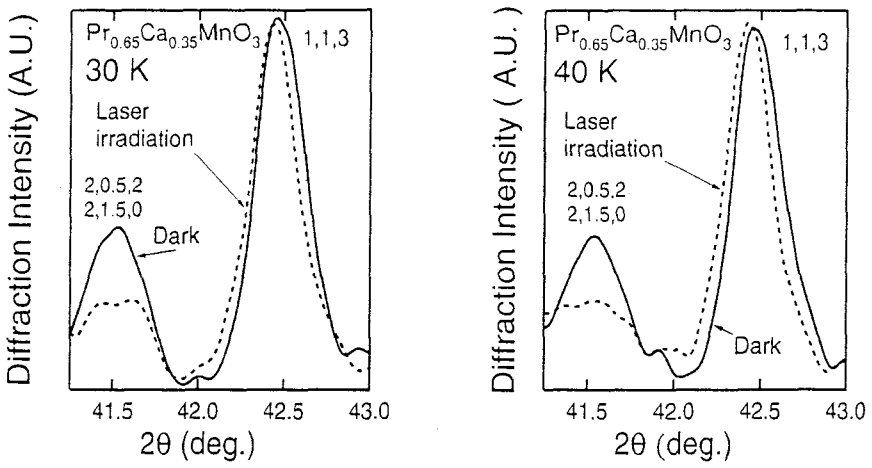

Fig. 3. Powder X-ray diffraction profiles at 30 K (a) and 40 K (b) from (2, 1.5, 0), (2, 0.5, 2) and (1, 1, 3) reflections with (dotted curve) and without (solid curve) cw-YAG laser irradiation ($h\upsilon = 1.17$ eV).

superlattice reflections under laser irradiation is possibly from the non-irradiated fraction of the powder particles with a mesh 20 μm and gradually melting CO domains [9], while the penetration depth of the laser light has been estimated to be about 0.2 μm [5] for the present sample.

The observed suppression of the superlattice reflection evidently indicates that the near-infrared laser irradiation with proper photon energy ~ 1.2 eV induces the collapse of CO state with ease, which would be together with the probable AF-CO to F-CD transition. In fact, Yoshizawa et al. [1] showed the suppression of the superlattice intensity at (2, 1.5, 0) under magnetic field as a evidence of the collapse of the CO state. However, it is the first to our knowledge that laser light irradiation suppresses the superlattice intensity at (2, 1.5, 0) structuraly. The present observation is not far from the previously observed I–M transition triggered by photocarrier generation by Miyano et al. [5]. Without structural evidence, they have stated the trace of the collapse of the CO state by observation of photocurrent under the coexistence of the applied electric field and pulse laser irradiation with 1.2 eV in the photon energy range 0.6 to 3.5 eV. First, we discuss the reason why we detect the collapse of CO state for photon energy ~ 1.2 eV. This energy value is characteristic in the optical spectra in these manganites. For example, there is a broad peak in the photoconductivity function centered around 1.2 eV in similar compound $La_{0.7}Ca_{0.3}MnO_3$ [19,20]. It is assigned as a charge-transfer excitation of an electron from the lower JT split e_g of Mn^{3+} to the e_g of adjacent Mn^{4+} ion, which exhibits the promotion of the dipole active photoionization of the JT small polaron [20]. Our present result suggests that the simple near-infrared laser irradiation with the characteristic photon energy ~ 1.2 eV enhances some kind of vibronic state and eventually releases the cooperative JT distortion associated with the CO state. The electronic conduction arises from the hopping of an electron from Mn^{3+} to Mn^{4+} with the electron transfer energy t. The large J_H means that the hopping of an outer-shell electron between two Mn sites is affected by the relative alignment of the core spins, being maximal when the core spins are parallel and minimal when they are antiparallel. This results in the ferromagnetic (F) double exchange interaction between the localized spins, the core t_{2g} orbital ($S = \frac{3}{2}$) mediated by the hopping e_g orbital electron. The insulating state is AF and the metallic state is ferromagnetic (F). We stress that the laser-induced conductance change in $La_{0.7}Ca_{0.3}MnO_3$ [20] has been observed near the PI to FM transition temperature. Highly polarized state of Mn^{3+} and Mn^{4+} spins as a ferromagnetic order is necessary to achieve the DC conductivity based on the collapsed CO state. The present result of X-ray diffraction, which excludes the heating by

laser irradiation, provides not only a structural evidence of collapse of the CO state by photon injection but also the photo-induced insulator–metal transition occurs with ease, together with the increase of the spin canting toward the spin polarization of Mn sites. The present results also reconfirm the inadequacy of a simple double exchange model and the importance of the influence of the lattice distortion as well as the AF ordering.

Second, we state that the present observation of the collapse of the CO state with relative ease is strongly related to the discommensuration for the charge and spin ordering in CO state for $0.3 \leqslant x \leqslant 0.75$, which is basically represented by their AF CE-type [8]. In the composition with $x = 0.5$, where Mn^{3+} and Mn^{4+} ions are arranged alternatively within the (0 0 1) plane and magnetic lattice is expanded to $4\boldsymbol{a} \times 4\boldsymbol{b} \times 2\boldsymbol{c}$ in the pseudocubic setting. This fact indicates that they need some additional mechanism which stabilizes the CE-type spin structure even at $x = 0.35$ despite a considerable spin disorder in the AF insulator. When x reduces from 0.5 to 0.3, the spin arrangement within the *ab* plane preserves CE-type feature but that along the *c* direction changes from antiparallel to parallel. Such an x-dependent antiferromagnetic AF structure has been discussed in terms of the double exchange interaction along the *c*-axis direction mediated by the extra electrons [1], the concentration of which is $(1/2 - x)$/Mn site and measures the degree of the discommensuration. The deviation of x from 0.5 plays an important role in the melting of the CO state with relative ease at the low-temperature side. The CO state suppresses the ferromagnetic metal and favors an AF ordering [1,2], eventually leading to the CAF state below $T_{CAF} = 125$ K lower than the AF state. The AF components are parallel to the [0 0 1] axis and the ferromagnetic components lies in the (0 0 1) plane. In the present results, the CAF state seems to be related with the invasion of the metallic phase based on the collapse of the CO state with near-infrared laser irradiation.

4. Summary

We studied the $Pr_{1-x}Ca_xMnO_3$ ($x = 0.35$) in which the CO state were suppressed with relative ease by the external field and/or stimulation below $T_{CAF} \sim 125$ K. The structural behavior of the $Pr_{0.65}Ca_{0.35}MnO_3$ was studied with the PXD. The superlattice reflections observed below $T_{CO} \sim 215$ K persist down to at least 10 K throughout the AF transition at $T_{AF} \sim 180$ K and the CAF transition at $T_{CAF} \sim 125$ K. The present result confirms that the CO state is retained without the external stimulation and survives with X-ray irradiation to measure the diffraction. A prominent reduction of superlattice reflection intensities was clearly found out under the photon injection by the cw-YAG laser irradiation ($h\upsilon = 1.17$ eV) at below T_{CAF}, which leads to the evidence of the collapse of the CO state. The observed photo-induced collapse of the CO state is suspected to be associating with the I–M transition due to the propagation of the delocalized carriers owing to the double exchange interaction revived in the spin polarization with Mn sites.

References

[1] H. Yoshizawa, H. Kawano, Y. Tomioka, Y. Tokura, Phys. Rev. B 52 (1995) 13145.
[2] Y. Tomioka, A. Asamitsu, H. Kuwahara, Y. Moritomo, Phys. Rev. B 53 (1996) 1689.
[3] H. Chiba, M. Kikich, K. Kusaba, Y. Muraoka, Y. Syono, Solid State Commun. 99 (1996) 499.
[4] S. Jin, T.H. Tiefel, M. McCormack, R.A. Fastnacht, R. Ramesh, L.H. Chen, Science 264 (1994) 413.
[5] K. Miyano, T. Tanaka, Y. Tomioka, Y. Tokura, Phys. Rev. Lett. 78 (1997) 4257.
[6] A. Asamitsu, Y. Tomioka, H. Kuwahara, Y. Tokura, Nature 388 (1997) 50.
[7] V. Kiryukhin, D. Casa, J.P. Hill, B. Keimer, A. Vigilante, Y. Tomioka, Y. Tokura, Nature 386 (1997) 813.
[8] Z. Jirak, S. Krupicka, Z. Simsa, M. Dlouha, S. Vratislav, J. Magn. Magn. Mater. 53 (1985) 166.
[9] D.E. Cox, P.G. Radaelli, M. Marezio, S.-W. Cheong, Phys. Rev. B 57 (1998) 3305.
[10] C. Zener, Phys. Rev. 82 (1951) 403.
[11] P.W. Anderson, H. Hasegawa, Phys. Rev. 100 (1955) 675.
[12] J.B. Goodenough, Phys. Rev. 100 (1955) 564.
[13] A.J. Millis, Boris I. Shraiman, R. Mueller, Phys. Rev. Lett. 77 (1996) 175.
[14] D. Feinberg, P. Germain, M. Grilli, G. Seibold, Phys. Rev. B. 57 (1998) 5583.
[15] E.O. Wollan, W.C. Koeiiler, Phys. Rev. 100 (1955) 545.

[16] H. Kuwahara, Y. Tomioka, A. Asamitsu, Y. Moritomo, Y. Tokura, Science 270 (1995) 961.
[17] F. Izumi, in: R.A. Young (Ed.), The Rietveld Method, Oxford University Press, Oxford (Chapter 13) 1993.
[18] Kenji Nakanishi, Hideo Nojima, Osami Yanagisawa, Mitsuru Izumi, Wei-Zhi Hu, unpublished.
[19] S. Kaplan, M. Quijada, H.D. Drew, D.B. Tanner, G.C. Xiong, R. Ramesh, C. Kwon, T. Venkatesan, Phys. Rev. Lett. 77 (1996) 2081.
[20] Y.G. Zhao, J.J. Li, R. Shreekala, H.D. Drew, C.L. Chen, W.L. Cao, C.H. Lee, Phys. Rev. Lett. 81 (1998) 1310.

ELSEVIER

Journal of Magnetism and Magnetic Materials 000 (1999) 000–000

Journal of magnetism and magnetic materials

www.elsevier.com/locate/jmmm

Magnetic transitions in thin films of $La_{0.67}Ca_{0.33}MnO_3$ and $Pr_{0.65}Ca_{0.35}MnO_3$

Osami Yanagisawa[a,*], Mitsuru Izumi[a], Kai-Hua Huang[a], Wei-Zhi Hu[a], Yi Shen[a], Kenji Nakanishi[b], Yoshihiro Takahashi[b], Hideo Nojima[b]

[a]*Laboratory of Applied Physics, Tokyo University of Mercantile Marine, Etchu-jima 2-1-6, Koto-ku, Tokyo 135-8533, Japan*
[b]*Ecological Tech. Development Center, Sharp Corporation, Kashiwa 273-1, Kashiwa-shi, Chiba 277-0005, Japan*

Abstract

Electron paramagnetic resonance (EPR) measurements were carried out to study the appearance of magnetic order in the ground states of both $La_{0.67}Ca_{0.33}MnO_3$ (LCMO) and $Pr_{0.65}Ca_{0.35}MnO_3$ (PCMO) thin films. LCMO undergoes the transition of the paramagnetic insulating phase into the metallic ferromagnetic phase below the Curie temperature (T_c = 260 K). The PCMO films also undergoes the transition into the ferromagnetic phase when the temperature is lowered through the critical value (T_c = 120 K). Below T_c the EPR spectrum of both films splits into lines that shift to the low magnetic resonance field with decrease in temperature. The temperature dependence of the resonance magnetic field in both EPR spectra obeys the critical behavior of a second-order phase transition, corresponding to the appearance of the spontaneous magnetic moment. In contrast to the bulk PCMO sample, PCMO thin films prepared by the sol–gel method shows only one magnetic transition.

Keywords: Magnetic materials; Oxides; Phase transitions; Colossal magnetoresistance; Electron spin resonance

1. Introduction

The perovskite manganese oxide (LaMnO3), an antiferromagnetic insulator in room temperature, has been intensively studied during the last decade. In particular, the object of special interest was the magnetic field induced insulator–metal transition of the mixed compounds along the series: $R_{1-x}A_xMnO_3$, where R is a rare-earth trivalent ion and A is an alkali divalent ion [1]. The basic physics of the ground state concerns a competing interaction between antiferromagnetic and ferromagnetic spin order of Mn^{3+} and Mn^{4+} ions. This interaction is primarily correlated with the choice of a pair of R and A ions [2]. The main factors influencing the realization of the different magnetic states in these compounds are: (I) the ionic radii of R and A ions leading in some cases to the distorted manganese perovskite structure associated with modification of the distance between Mn ion sites via inter-site oxygen, (II) the chemical composition and the accompanied incommensurable effects creating the differences in the population of Mn^{3+}/Mn^{4+} ion sites [3]. For x close to 0.5, it results in the charge-order (CO) state with the ground state of AF spin order. The proper choice of

* Corresponding author. Tel.: +81-3-5245-7466; fax: +81-3-5245-7339.
E-mail address: osami@zairyo.phys.tosho-u.ac.jp (O. Yanagisawa)

0304-8853/99/$-see front matter
PII: S0304-8853(99)00743-X

La/Ca atomic radius ratio of $La_{0.67}Ca_{0.33}MnO_3$ (LCMO) results in the ferromagnetic ground state with a metallic conduction below the insulator–metal transition temperature (T_c) that exhibits a colossal magnetoresistance (CMR) around T_c [4]. In a powder $Pr_{0.65}Ca_{0.35}MnO_3$ (PCMO) composition, a proper choice of Pr/Ca ratio gives a material-showing-successive phase transitions from paramagnetic to CO state, subsequently antiferromagnetic and finally canted antiferromagnetic state [3,5]. The PCMO sample also shows the CMR with a low applied magnetic threshold field below the onset temperature of the spin canting antiferromagnetic order. Both materials can be prepared in thin films that are crucial in their future potential applications, particularly in the field of magnetic recording [6]. The laser-light induced phenomena in the PCMO system is currently focussed. The CO state, which has been retained down to its ground state, can be "melted" not only by the magnetic field of a usual CMR but also by the various external stimuli such as near-infrared laser irradiation [7,8], electric field [9] or synchrotron X-ray illumination [10]. In the present communication, the recent results of the studies of preparation of both compounds by the sol–gel method, the structural characterization of LCMO- and PCMO-based thin films and the electron paramagnetic resonance (EPR) have been reported.

2. Experimental results and discussion

Both LCMO and PCMO thin film samples were prepared by sol–gel method in the $SrTiO_3$ (1 0 0) substrate. First, a repetition of spin coatings was done starting from the xylene solution followed by the drying and pyrolysis processes at 430°C for 10 min. Second, the crystallization was driven by the rapid thermal annealing (RTA) method under N_2O gas flow. The optimal crystallization was obtained at 1000°C for LCMO and at 900°C for PCMO samples.

With the X-ray diffraction technique, we can confirm that these samples have a high degree of crystallinity and proper orientation on the *c*-axis. Fig. 1 shows the X-ray diffraction profiles of LCMO and PCMO thin film samples. For the substrate, the 002 diffraction peak profile is shown with the 002 peak. In the case of LCMO thin films, the repetition of the post-crystallization annealing at 800°C is remarkable with an increase in T_c. This is directly connected to the insulator–metal transition temperature obtained from the DC resistance measurements. The increase in T_c (the highest $T_c = 310$ K) is most probably caused by the increase in oxygen content. Our samples LCMO and PCMO films were typically 5000 Å thick.

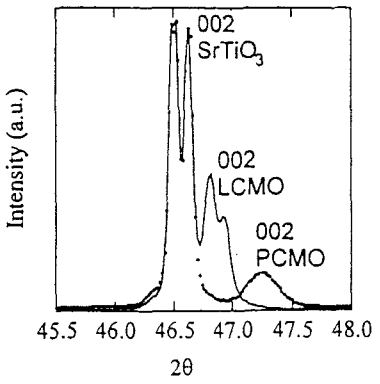

Fig. 1. X-ray, Cu-K_α diffraction profiles around [0 0 2] of $La_{0.67}Ca_{0.33}MnO_3$ (LCMO) and $Pr_{0.65}Ca_{0.35}MnO_3$ (PCMO) thin films in addition to the [0 0 2] line from the $SrTiO_3$ [0 0 1] substrate. The lengths of the *c*-axis were 3.884 and 3.843 Å in LCMO and PCMO, respectively.

Fig. 2 presents the DC resistivity as a function of temperature in $Pr_{0.65}Ca_{0.35}MnO_3$ (PCMO) and $La_{0.67}Ca_{0.33}MnO_3$ (LCMO) thin film samples. The composition of PCMO thin films shows the semiconducting behavior with the activation energy of 48 meV without any sign of the formation of the CO state (see the temperature derivative resistance (dR/dT) curve). This is in contrast with the observation of the CO-phase transition in the bulky PCMO sample at 215 K [3,5,11]. Due to, either a mismatch of the optimal lattice constant of PCMO with that of the applied substrate or some kind of lattice defects, the optimal population of Mn^{3+} and Mn^{4+} ions looks difficult to be achieved in the studied films. In the subsequent discussion, we will focus on the survey of the onset of some kind of magnetic transition in the PCMO thin film. For LCMO composition, the thin film shows the

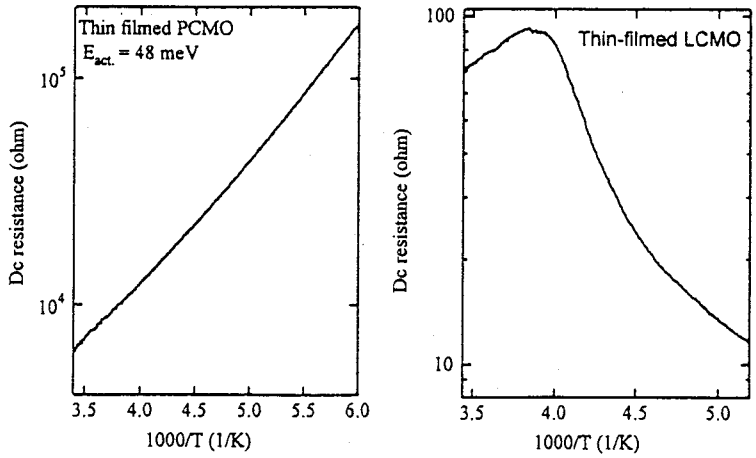

Fig. 2. The temperature dependence of DC resistivity of the $Pr_{0.65}Ca_{0.35}MnO_3$ (PCMO) and $La_{0.67}Ca_{0.33}MnO_3$ (LCMO) thin film samples. PCMO films exhibit the semiconductive behavior with the activation energy of 48 meV. The LCMO film shows the insulator–metal transition at 260 K (T_c) together with a large CMR.

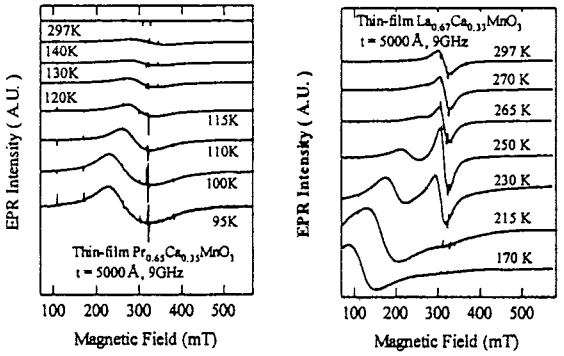

Fig. 3. EPR spectra measured at 9 GHz for $Pr_{0.65}Ca_{0.35}MnO_3$ (PCMO) and $La_{0.67}Ca_{0.33}MnO_3$ (LCMO) thin films under $H_0 \perp c$-axis geometry. The sharp resonance peaks around 320 mT come from the reference material Mn^{2+}/MgO as a marker.

insulator–metal transition at 260 K (T_c) together with a large CMR.

The temperature dependence of EPR spectrum was studied with 100 kHz modulation at 9 GHz to achieve the microscopic information.

Fig. 3 shows the EPR profiles for PCMO and LCMO thin films. The static magnetic field H_0 was applied parallelly to the surface of the films ($H_0 \perp c$-axis). In PCMO sample, the EPR signal intensity of $g \sim 2.0$ gradually increases with decreasing temperature, suggesting the existence of the paramagnetic susceptibility. Below 125 K (T_c), the spectrum splits into a minimum of two lines and the center magnetic field of the resonance profile shifts to a low magnetic field with decreasing temperature. The observed resonance-shift signals the appearance of the spontaneous magnetization. The results obtained are in contrast with the observed EPR signals for the same nominal composition however in "powder" form of PCMO sample [11].

The thin film of LCMO shows the paramagnetic behavior down to 270 K and around 260 K (T_c) the spectrum splits into two lines. One of them shifts to a low resonance field with the broad line. The other resonance line remains with $g \sim 2$ band and successively vanishes below 215 K.

In Fig. 4, the resonance magnetic field in both PCMO and LCMO thin films have been plotted. These values were taken from the simple unconvolution of the obtained spectrum. The observed shift of the resonance magnetic field is noted as Δg (shift of the resonance g value).

The temperature dependence of Δg below T_c indicates the critical behavior in the case of the existence of magnetic transition. According to the simple phenomenological Landau theory of the second-order phase transition [12], we have performed the fit of the obtained center magnetic field

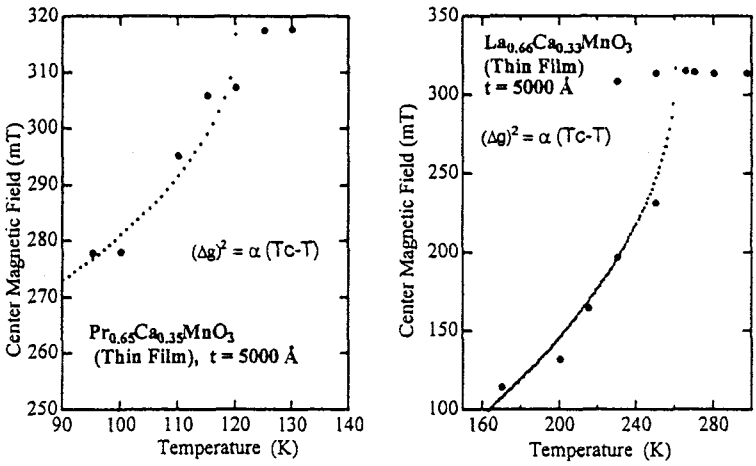

Fig. 4. The temperature dependence of the resonance magnetic field of the EPR spectrum (closed circles) in $Pr_{0.65}Ca_{0.35}MnO_3$ (PCMO) and $La_{0.67}Ca_{0.33}MnO_3$ (LCMO) thin films. The broken curves show the calculated values for $(\Delta g)^2$ which is defined as an order parameter under the Landau theory of the second-order phase transition [12].

Δg to the $\alpha(T_c - T)^{1/2}$ where α is the positive constant. As shown in Fig. 4, a good agreement between the obtained resonance shift and the calculated $(\Delta g)^2$ was achieved for both compounds below T_c. It has been reported that LCMO undergoes into the ferromagnetic metal state below $T_c = 260$ K [4]. The present PCMO thin films similarly indicate the existence of the magnetic transition with ferromagnetic order at $T_c = 120$ K.

In conclusion, in the PCMO thin films, there is no onset of the CO phase around 215 K in the DC resistivity behavior as seen in the bulky PCMO [11]. The mismatch between the optimal lattice constants of bulky PCMO and those of substrate or some kind of lattice defects and strains, the insufficient population of Mn^{3+} and Mn^{4+} ions might prevent the realization of the identical properties as seen in the bulky PCMO samples [13]. In contrast to the bulk PCMO, we have found the existence of the onset of the magnetic transition at 120 K in the thin films of PCMO. The temperature dependence of the resonance field-shift below 120 K is consistent with the phenomenological order parameter induced from the second-order transitional scheme. The more precise studies in order to identify the origin of the observed resonance are presently in progress. They concern both the paramagnetic resonance of ferromagnetic clusters and the propagation of magnetic polarons [14,15]. Finally, our suggestion points to the existence of probable spin-fold over the effect of the spin wave below 90 K for PCMO and 150 K for LCMO thin films, which is a characteristic behavior of ferromagnetic thin films.

References

[1] A.J. Millis, Nature 392 (1998) 147.
[2] J.Z. Sun, L. Krusin-Elbaum, A. Gupta, Gang Xiao, P.R. Duncombe, S.S.P. Parkin, IBM J. Res. Dev. 42 (1998) 89.
[3] H. Yoshizawa, H. Kawano, Y. Tomioka, Y. Tokura, J. Phys. Soc. Jpn. 65 (1996) 1043.
[4] Q. Huang, A. Santoro, J.W. Lynn, R.W. Erwin, J.A. Borchers, J.L. Peng, K. Ghosh, R.L. Greene, Phys. Rev. B 58 (1998) 2684.
[5] R. Cox, P.G. Radaclli, M. Marezio, S.-W. Cheong, Phys. Rev. B 57 (1998) 3305.
[6] A. Goyal, M. Rajeswari, R. Shreekala, S.E. Lofland, S.M. Bhagat, T. Boettcher, C. Kwon, R. Ramesh, T. Venkatesan, Appl. Phys. Lett. 71 (1997) 2535.
[7] K. Miyano, T. Tanaka, Y. Tomioka, Y. Tokura, Phys. Rev. Lett. 78 (1997) 4257.
[8] O. Yanagisawa, M. Izumi, W.-Z. Hu, K. Nakanishi, H. Nojima, J. Superconductivity 12 (1999) 311.
[9] A. Asamitsu, Y. Tomioka, H. Kuwahara, Y. Tokura, Nature 388 (1997) 50.
[10] V. Kiryukhin, D. Casa, J.P. Hill, B. Keimer, A. Vigliante, Y. Tomioka, Y. Tokura, Nature 386 (1997) 813.

[11] O. Yanagisawa, M. Izumi, W.-Z. Hu, K. Nakanishi, H. Nojima, J. Superconductivity 12 (1999) 307.
[12] R.A. Cowley, Adv. Phys. 29 (1980) 1.
[13] K.A. Thomas, P.S.I.P.N. de Silva, L.F. Cohen, A. Hossain, M. Rajeswari, T. Venkatesan, R. Hiskes, J.L. MacManus-Driscoll, J. Appl. Phys. 84 (1998) 3939.
[14] D.C. Worledge, L. Mieville, T.H. Geballe, J. Appl. Phys. 83 (1998) 5913.
[15] O. Chauvet, G. Goglio, P. Molinie, B. Corraze, L. Brohan, Phys. Rev. Lett. 81 (1998) 1102.

ELSEVIER

Journal of Magnetism and Magnetic Materials 000 (1999) 000–000

journal of magnetism and magnetic materials

www.elsevier.com/locate/jmmm

Comparative study of photo-induced effect on the charge-ordered state of $Pr_{0.65}Ca_{0.35}MnO_3$ in powder and thin films

Osami Yanagisawa[a,*], Mitsuru Izumi[a], Kai-Hua Huang[a], Wei-Zhi Hu[a], Yi Shen[a], Kenji Nakanishi[b], Yoshihiro Takahashi[b], Hideo Nojima[b]

[a]*Laboratory of Applied Physics, Tokyo University of Mercantile Marine, Etchu-jima 2-1-6, Koto-ku, Tokyo 135-8533, Japan*
[b]*Ecological Tech. Development Center, Sharp Corporation, Kashiwa 273-1, Kashiwa-shi, Chiba 277-0005, Japan*

Abstract

Recent progress on the survey of photo-induced effect in $Pr_{0.65}Ca_{0.35}MnO_3$ is reported with respect to the electron paramagnetic resonance (EPR) and X-ray diffraction (XRD). In the powder samples, a photo-induced effect is reported in the charge-ordered (CO) phase associated with the canted antiferromagnetic (AF) spin order. First, the paramagnetic resonance, which is diminished at the onset of the AF spin order, revives with the near-infrared laser irradiation of $h\upsilon = 1.17$ eV. Second, XRD indicates that the photo-induced paramagnetic resonance is associated with the melting of the CO formed by the alternation of the ionic valence of Mn. The thin films of $Pr_{0.65}Ca_{0.35}MnO_3$ prepared by the sol–gel method exhibit magnetic transition at low temperature. However, the ground state of the discussed thin film is not accompanied by the CO-state.

PACS: ■; ■; ■

Keywords: Magnetic materials; Oxides; Colossal magnetoresistance; Electron paramagnetic resonance

Jolly VS Mallikarjun

1. Introduction

From the viewpoint of potential applications of the distorted manganese perovskites, as the first step, it is crucial to optimize the colossal magnetoresistance (CMR) effect by using external stimuli such as electric field, X-ray, and laser light. The distorted manganese perovskites, $R_{1-x}A_xMnO_3$, where R is trivalent rare-earth atom and A is divalent alkaline earth element, provide us amazing physical properties depending on the population of Mn^{3+} and Mn^{4+} ions. Such amazing physical properties are explained by a competing interaction between two different ground states, i.e., the charge-ordered (CO) insulating state associated with the antiferromagnetic (AF) spin order on Mn ionic sites and the ferromagnetic (F) charge-delocalized (CD) state. The growth of the CO state formed by the ionic valence alternation of Mn is regardless of the cooperative

* Corresponding author. Tel.: +81-3-5245-7466; fax: +81-3-5245-7339.
E-mail address: osami@zairyo.phys.tosho-u.ac.jp (O. Yanagisawa)

0304-8853/99/$ - see front matter
PII: S0304-8853(99)00724-6

Jahn–Teller (JT) distortion, which clearly suppresses the ferromagnetic double-exchange interaction leading to the CD state [1–7]. On heating, both CO and CD states transform into a charge-localized paramagnetic phase characterized by semi-conducting properties. The switching of DC resistivity between CO and CD states in manganites can be achieved not only by applying a magnetic field but also by an electric field. In $Pr_{1-x}Ca_xMnO_3$, an electrical current implied by static electric field triggers the antiferromagnetic insulator (AFI)–ferromagnetic metal (FM) transition at low temperature [8]. This AFI–FM transition can also be driven by the synchrotron X-ray illumination at a low temperature (< 40 K) which is accompanied by a significant change in the lattice structure and which can be reversed by thermal cycling [9]. Miyano et al. [10] have studied the trace of the collapse of the CO state by the observation of a photo-current under the action of both an applied electric field and a pulse of laser irradiation of photon energy $h\upsilon = 1.2$ eV. We have reported the different aspects of the photo-induced effect on the electron paramagnetic resonance (EPR) and the X-ray diffraction (XRD) in the powder sample of $Pr_{0.65}Ca_{0.35}MnO_3$ under near-infrared laser irradiation of photon energy $h\upsilon = 1.17$ eV [11,12]. The results give an evidence for the photo-induced collapse of the CO in $Pr_{0.65}Ca_{0.35}MnO_3$.

As the second step, the fabrication of the thin-film samples provides the advantages to the industrial application. However, the phenomenon of oxygen stoichiometry in the thin-film samples varies in the preparatory condition and influences the charge carrier concentration as well as electrical properties like most of the metal oxides. A strain effect due to the lattice mismatch between the film and the substrate plays an important role resulting in a distortion of perovskite structure of manganite and eventually the population of Mn^{3+} and Mn^{4+} ions.

In the present communication, our results of the photo-induced effect on the powder sample will be compared to those of the thin-film samples prepared by the sol–gel method. It is shown that there is a large difference between the powder and the thin films with respect to the existence of the CO-state.

2. Experiment

The powder samples of $Pr_{0.65}Ca_{0.35}MnO_3$ were carefully prepared by calcimining the mixture of a prescribed amount of manganese, calcium carbonates and praseodymium oxide in air at 1400°C using the usual ceramic technique [4]. The thin-film samples of $Pr_{0.65}Ca_{0.35}MnO_3$ with 5000 Å thickness were prepared by the sol–gel method on $SrTiO_3$ (1 0 0) single-crystal substrates. First, a repetition of the spin-coating was done starting with a xylene-MOD solution and following by a dry and pyrolysis process at 430°C, for 10 min. Second, the crystallization was done by rapid thermal annealing (RTA) under N_2O gas flow. The optimal crystallization was obtained at 900°C. The XRD was carried out at room temperature to study the crystallographic characters.

The temperature dependence of DC on the resistance was measured by a conventional four-probe method from 290 to 5 K under an applied magnetic field up to 6 T using a super-conducting magnet (Oxford Maglab 2000).

The EPR study for the spin states of 3d-t_{2g} ($S = 2$) and/or 3d-e_g ($S = \frac{3}{2}$) on Mn^{3+} and Mn^{4+} ionic sites was done using a spectrometer operated at 9.0 GHz (X-band) from 300 K down to 10 K. The sample was mounted in a liquid-He continuous-flow type cryostat. For the thin-film sample, the static magnetic field H_0 was applied perpendicular to the c-axis of the film. To investigate the photo-induced effect, a He–Ne CW laser of photon energy, $h\upsilon = 1.96$ eV and a Nd–YAG CW laser of $h\upsilon = 1.17$ eV were employed for the photon injection. The laser power was adjusted with an optical slit resulting in 5, 50 and 175 mW (9×10^{17} photons/s.) for the Nd–YAG laser, and 5 mW for the He–Ne laser. It is noted that the described value of the laser power does not indicate the exact value injected into the samples due to the double-shielded He-flow-guide made from quartz glass. The penetration depth of the laser light has been estimated to be about 0.2 μm for the present sample [6]. The EPR measurement was done under the sequence in which the ESR profiles were measured without the photon injection, with the photon injection and once more without the photon injection (dark) successively to check if there is any damage to the sample.

The XRD with the photon injection ($h\upsilon = 1.17$ eV) for $Pr_{0.65}Ca_{0.35}MnO_3$ powder sample in the temperature range 300–5 K were taken to investigate the mechanism of the photo-induced effect. The maximum laser power was monitored to be 175 mW. It is noted that the described value of the monitored laser power does not indicate the precise value injected into the samples due to the existence of the window shielded with the Kapton foil for the He cryostat. The XRD was carried out with the same procedure as the ESR measurement under the photon injection.

3. Results and discussion

Fig. 1(a) shows the XRD profile of $Pr_{0.65}Ca_{0.35}MnO_3$ powder sample at 290 K (closed circles) together with the result of the profile fit by Rietveld analysis (solid line). The present XRD analysis indicates that the present sample is in single phase of $Pr_{0.65}Ca_{0.35}MnO_3$ with the distorted perovskite structure belonging to the orthorhombic space group Pbnm. The grain size is about 20 μm. Fig. 1(b) shows the XRD profile of $Pr_{0.65}Ca_{0.35}MnO_3$ film at 290 K. The peak profile of the 002 peak is shown with the 002-diffraction peak of the $SrTiO_3$ substrate. XRD indicates the formation of high degree of crystalline order and orientation of the c-axis due to the annealing procedure under N_2O gas flow. The typical sample thickness is around 5000 Å.

The electric transport property of the powder and the thin-film samples are significantly different. Fig. 2(a) shows the temperature dependence of the differential resistance (dR/dT) of $Pr_{0.65}Ca_{0.35}MnO_3$ powder. It is semiconductor-like without external magnetic field in the whole temperature range. The dR/dT shows a prominent peak which is evident due to the second-order phase transition associated with formation of the CO state where the charge is localized on Mn ionic site at $T_{CO} \sim 215$ K together with the Mn^{3+} and Mn^{4+} alternation leading to the superlattice X-ray reflection [12]. The powder sample shows a CMR effect $(R_M - R_0)/R_0 \sim 400\%$ with a threshold magnetic field of about 2 T at the CO state below T_{CO} 215 K. Fig. 2(b) shows the temperature dependence of the dR/dT of a $Pr_{0.65}Ca_{0.35}MnO_3$ thin-film sample. The dR/dT does not show any clear sign of the onset of the second-order transition that gives an evidence for the existence of the CO-state. The present thin film samples do not show any significant CMR effect at high magnetic fields up to 6 T in the whole temperature range. It showed rather a positive magnetoresistance.

In Fig. 3(a), the dotted curves show the EPR profiles for the $Pr_{0.65}Ca_{0.35}MnO_3$ powder sample without photon injection (dark). The EPR spectrum exhibits a paramagnetic feature at room tem-

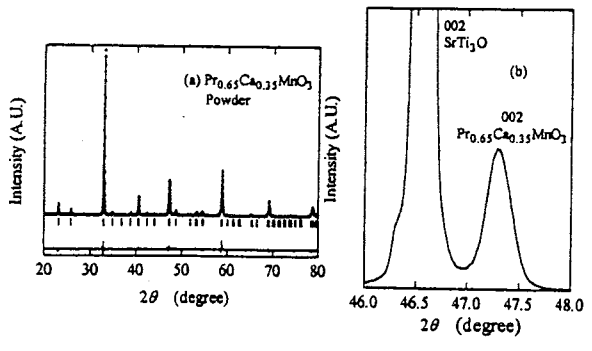

Fig. 1. (a) X-ray diffraction pattern of $Pr_{0.65}Ca_{0.35}MnO_3$ powder sample at 290 K together with the result of the profile fit by Rietveld analysis [14] with solid lines. (b) The X-ray diffraction pattern of a $Pr_{0.65}Ca_{0.35}MnO_3$ thin film sample at 290 K.

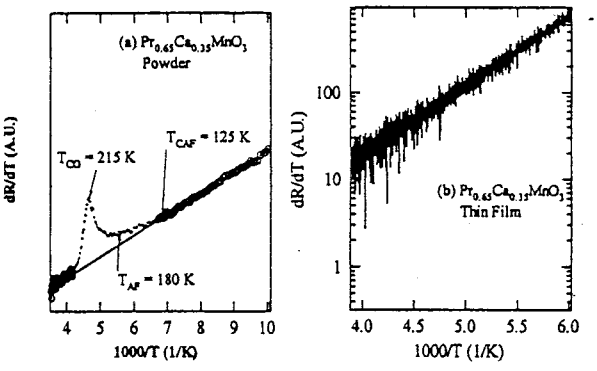

Fig. 2. (a) Shows temperature dependence of the differential resistance (dR/dT) of a $Pr_{0.65}Ca_{0.35}MnO_3$ powder sample. (b) Shows temperature dependence of the dR/dT of a $Pr_{0.65}Ca_{0.35}MnO_3$ thin film sample.

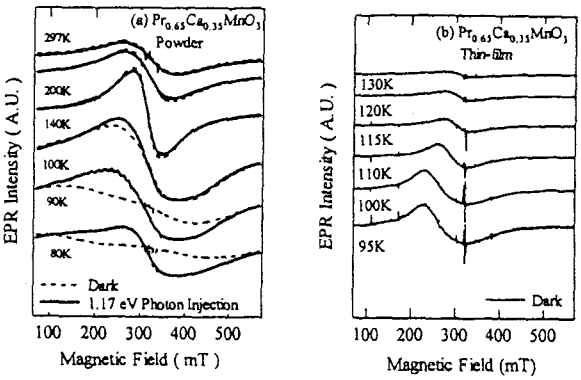

Fig. 3. (a) Temperature dependence of the X-band EPR profiles for a $Pr_{0.65}Ca_{0.35}MnO_3$ powder sample without optical excitation (dark) and with Nd–YAG laser irradiation ($h\upsilon = 1.17$ eV). (b) Temperature dependence of the EPR profiles for a $Pr_{0.65}Ca_{0.35}MnO_3$ thin-filmed sample without the photon injection (dark).

perature. This paramagnetic feature is retained down to the CO phase below $T_{CO} \sim 215$ K. Below the onset of the AF phase at $T_{AF} \sim 180$ K, the EPR signal becomes weak with decreasing temperature. Eventually, the characteristic feature of the ensemble of spin clusters appears around the onset of the canted antiferromagnetic state of $T_{CAF} \sim 115$ K. This is in good agreement with the phase diagram of $Pr_{1-x}Ca_xMnO_3$ determined by resistivity, magnetization and neutron diffraction [3,5,13]. It is stressed that below T_{CAF}, the EPR profiles become broadened with some kind of dissociation of the total magnetic moments, which is in accordance with the behavior of DC magnetization in the warming run after zero-field cooling [14]. The resonance is more characteristic of ferromagnetic resonance from a collection of independent and randomly oriented anisotropic crystalline samples. Anti-ferromagnetic resonance is not probable since the individual exchange field of the separate magnetic sublattices would be too large to provide a resonance at 9.0 G Hz.

In Fig. 3(a), the thick solid curves show the EPR profiles under the photon injection by a Nd–YAG laser ($h\upsilon = 1.17$ eV). It is clear that the EPR intensity starts to depend on the photon injection below $T_{CO} \sim 215$ K with decreasing temperature and strikingly recovers its paramagnetic resonance intensity even below T_{CAF} (115 K). The present photo-induced effect becomes predominant below 100 K [6,14]. It is worth noting that evidence against the laser heating is provided by the temperature dependence of EPR profiles [11]. This photo-induced transformation of the EPR profile was reproducible, not permanent and also not due to any damage to the sample by laser irradiation. In fact, the EPR profile after the post-measurement with the photon injection appears almost identical with that obtained prior to the measurement under the photon injection. In the temperature range of 100–80 K, the obtained photo-induced effect indicates that the paramagnetic χ_{eff} revives owing to the photon injection ($h\upsilon = 1.17$ eV). These results indicate that the CO state with canted antiferromagnetic spin order can be transformed into paramagnetic and/or ferromagnetic order. In the following, the XRD profile measured under the near-infrared laser irradiation clearly suppresses the super-lattice reflection, which provides us with evidence for the melting of the CO. It is clear that the energy value of 1.17 eV of laser light is assigned as a charge-transfer excitation of an electron from the lower Jahn–Teller (JT) split e_g of Mn^{3+} to the e_g of adjacent Mn^{4+} ion. The present e_g-level interpretation indicates that the photo-induced I–M transition or equivalently the collapse of the CO state, occurs under the excitation by laser light with optimal energy. In fact, in contrast to the photon injection ($h\upsilon = 1.17$ eV), the EPR resonance intensity is not affected under He–Ne laser irradiation ($h\upsilon = 1.96$ e V). The photon energy, $h\upsilon = 1.17$ e V, is characteristic in the optical spectra in $R_{1-x}A_xMnO_3$. It has been assigned as a charge-transfer excitation energy of an electron from the lower JT split e_g of Mn^{3+} to the e_g of adjacent Mn^{4+} ion, which exhibits the promotion of the dipole active photoionization of the JT small polaron [5]. Our present result suggests that the simple near-infrared laser irradiation with the characteristic photon energy, $h\upsilon \sim 1.2$ eV enhances some kind of vibronic state and eventually releases the cooperative JT distortion associated with CO state.

The XRD profile for the $Pr_{0.65}Ca_{0.35}MnO_3$ powder sample shows that the super-lattice reflection peaks appear below $T_{CO} \sim 215$ K. These peaks are associated with the formation of the CO

state with $a \times 2b \times c$ cell. The present CO structure is maintained down to at least 10 K [12]. The photon injection ($h\upsilon = 1.17$ eV) conducts to the prominent decrease of the intensity of the superlattice reflections. The present result eventually provides a structural evidence for the collapse of the CO state by photon injection. We suspect that the photo-induced insulator–metal transition occurs together with the collapse of the CO-state.

In Fig. 3(b), the thin solid curves show the EPR profiles for the $Pr_{0.65}Ca_{0.35}MnO_3$ thin film without laser irradiation (dark) at temperature range 130–95 K. The EPR signal was very weak and paramagnetic above 130 K. In the thin film samples, the EPR intensity with $g \sim 2.0$ gradually increases with decreasing temperature, suggesting the existence paramagnetic susceptibility. Below 120 K, the spectrum splits into at least two lines and the central magnetic field of the resonance profile shifts to a low magnetic field with decreasing temperature. The observed resonance-shift indicates the appearance of the spontaneous magnetization. The temperature dependence of the resonance field-shift below 120 K is in good agreement with the phenomenological order parameter, which is induced from the second-order transition scheme [15]. The precise study to identify the origin of the observed resonance is under progress with respect to both paramagnetic resonance of ferromagnetic clusters and the propagation of magnetic polarons [16,17]. The EPR profiles in the present thin film exhibit a significant modification under the laser irradiation ($h\upsilon = 1.17$ eV) in temperature range 110–95 K. We think that the present result has to be a kind of photo-induced effect. However, the mechanism of this effect does not come from the photo-induced melting of the CO as in the powder sample. This is because there is no evidence for the existence of the CO state in this present thin film.

The electrical and magnetic properties of thin film and powder samples of $Pr_{0.65}Ca_{0.35}MnO_3$ are quite different as mentioned above. The difference may be due to the oxygen stoichiometry, the degree of order of the population of Mn ions, the charge carrier concentration and eventually electron hopping like in most metal oxide materials. A strain effect due to the lattice mismatch between the film and the substrate is plausible and it may control the distortion of perovskite structure.

With laser irradiation, we find the shift of the resonance line to high magnetic field. We think that the present photo-induced effect is not due to the same mechanism as in the powder sample since the thin-film form does not possess the CO. It is worth noting that some ferromagnetic materials, for example mixed crystal $CdCr_{2-x}InxSe_4$ [18], show a photo-induced effect. Probably, the present transition in the thin films is a ferromagnetic transition with some kind of photo-induced effect, which is in contrast to the photo-induced effect in bulk compounds.

4. Summary

Thin film samples of $Pr_{0.65}Ca_{0.35}MnO_3$ prepared by the sol–gel method were studied compared to the powder sample focusing on the optimization of the photo-induced effect, which was observed in the powder sample especially by using EPR. The present thin-film sample shows a week photo-induced effect in the EPR profile under the photon injection by near-infrared laser ($h\upsilon = 1.17$ eV) in the temperature range 110–95 K. The temperature dependence of the dR/dT indicates a magnetic transition at $T_C \sim 120$ K but does not indicate the CO state in the present $Pr_{0.65}Ca_{0.35}MnO_3$ thin-filmed sample. We suspect that the observed effect is a kind of photo-induced effect but the mechanism of this effect is different from the photo-induced effect seen in the powder sample.

Acknowledgements

The authors would like to express their gratitude to Dr. N. Tsuchimine (Toshima Mfgs Co. Ltd.) for sample preparation and Dr. D. B. Romero and A. Weber (NIST) for useful discussion.

References

[1] C. Zener, Phys. Rev. 82 (1951) 403.
[2] P.W. Anderson, H. Hasegawa, Phys. Rev. 100 (1955) 675.
[3] J.B. Goodenough, Phys. Rev. 100 (1955) 564.

[4] Z. Jirak, S. Krupicka, Z. Simsa, M. Dlouha, S. Vratislav, J. Magn. Magn. Mater. 53 (1985) 153.
[5] A.J. Millis, B.I. Shraiman, R. Mueller, Phys. Rev. Lett. 77 (1996) 175.
[6] D. Feinberg, P. Germain, M. Grilli, G. Seibold, Phys. Rev. B 57 (1998) 5583.
[7] D.E. Cox, P.G. Radaelli, M. Marezio, S.-W. Cheong, Phys. Rev. B 57 (1998) 3305.
[8] A. Asamitsu, Y. Tomioka, H. Kuwahara, Y. Tokura, Nature 388 (1997) 50.
[9] V. Kiryukhin, D. Casa, J.P. Hill, B. Keimer, A. Vigliante, Y. Tomioka, Y. Tokura, Nature 386 (1997) 813.
[10] K. Miyano, T. Tanaka, Y. Tomioka, Y. Tokura, Phys. Rev. Lett. 78 (1997) 4257.
[11] O. Yanagisawa, M. Izumi, W.-Z. Hu, K. Nakanishi, H. Nojima, J. Supercond. 12 (1999) 311.
[12] O. Yanagiswa, M. Izumi, W.-Z. Hu, K.-H. Huang, K. Nakanishi, H. Nojima, Physica B, in press.
[13] H. Chiba, M. Kikuchi, K. Kusaba, Syono, Sol. Stat. Commun. 99 (1996) 499.
[14] O. Yanagisawa, M. Izumi, W.-Z. Hu, K. Nakanishi, H. Nojima, J. Supercond. 12 (1999) 307.
[15] R.A. Cowley, Adv. in Phys. 29 (1980) 1.
[16] D.C. Worledge, L. Mieville, T.H. Geball, J. Appl. Phys. 83 (1998) 5913.
[17] O. Chauvet, G. Goglio, P. Molinie, B. Corraze, L. Brohan, Phys. Rev. Lett. 81 (1998) 1102.
[18] Y.H. Kim, S.M. Bhagat, M.A. Manheimer, S. Tyagi, L. Maksymowicz, M. Lubecka, IEEE Trans. Magn. 28 (1992) 3195.